

1995

## Constrained least-squares digital image restoration

Rajeeb Hazra

*College of William & Mary - Arts & Sciences*

Follow this and additional works at: <https://scholarworks.wm.edu/etd>



Part of the [Computer Sciences Commons](#), and the [Electrical and Computer Engineering Commons](#)

---

### Recommended Citation

Hazra, Rajeeb, "Constrained least-squares digital image restoration" (1995). *Dissertations, Theses, and Masters Projects*. Paper 1539623865.

<https://dx.doi.org/doi:10.21220/s2-vrc2-fx80>

This Dissertation is brought to you for free and open access by the Theses, Dissertations, & Master Projects at W&M ScholarWorks. It has been accepted for inclusion in Dissertations, Theses, and Masters Projects by an authorized administrator of W&M ScholarWorks. For more information, please contact [scholarworks@wm.edu](mailto:scholarworks@wm.edu).

## **INFORMATION TO USERS**

**This manuscript has been reproduced from the microfilm master. UMI films the text directly from the original or copy submitted. Thus, some thesis and dissertation copies are in typewriter face, while others may be from any type of computer printer.**

**The quality of this reproduction is dependent upon the quality of the copy submitted. Broken or indistinct print, colored or poor quality illustrations and photographs, print bleedthrough, substandard margins, and improper alignment can adversely affect reproduction.**

**In the unlikely event that the author did not send UMI a complete manuscript and there are missing pages, these will be noted. Also, if unauthorized copyright material had to be removed, a note will indicate the deletion.**

**Oversize materials (e.g., maps, drawings, charts) are reproduced by sectioning the original, beginning at the upper left-hand corner and continuing from left to right in equal sections with small overlaps. Each original is also photographed in one exposure and is included in reduced form at the back of the book.**

**Photographs included in the original manuscript have been reproduced xerographically in this copy. Higher quality 6" x 9" black and white photographic prints are available for any photographs or illustrations appearing in this copy for an additional charge. Contact UMI directly to order.**

# **UMI**

A Bell & Howell Information Company  
300 North Zeeb Road, Ann Arbor, MI 48106-1346 USA  
313/761-4700 800/521-0600



# CONSTRAINED LEAST-SQUARES DIGITAL IMAGE RESTORATION

---

A Dissertation

Presented to

The Faculty of the Department of Computer Science

The College of William and Mary in Virginia

In Partial Fulfillment

Of the Requirements for the Degree of

Doctor of Philosophy

---

by

RAJEEB HAZRA

1995

UMI Number: 9537549

Copyright 1995 by  
Hazra, Rajeeb  
All rights reserved.

---

UMI Microform 9537549

Copyright 1995, by UMI Company. All rights reserved.

This microform edition is protected against unauthorized  
copying under Title 17, United States Code.

---

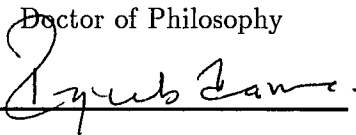
UMI

300 North Zeeb Road  
Ann Arbor, MI 48103

## APPROVAL SHEET

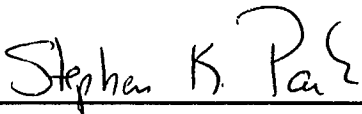
This dissertation is submitted in partial fulfillment of  
the requirements for the degree of

Doctor of Philosophy

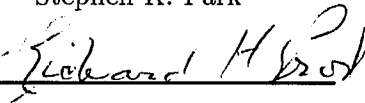


Author


Approved, March 1995



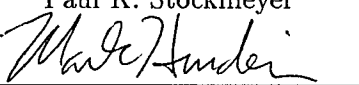
Stephen K. Park



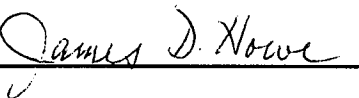
Richard H. Prosl



Paul K. Stockmeyer



Mark K. Hinders



James D. Howe



G. Louis Smith

© Copyright by Rajeeb Hazra 1995

All rights reserved

To my wife Mousumi,  
my daughter Dia,  
and my parents.



# Table of Contents

<b>Acknowledgements</b>	<b>ix</b>
<b>List of Figures</b>	<b>x</b>
<b>Abstract</b>	<b>xiii</b>
<b>INTRODUCTION</b>	<b>2</b>
1.1 Digital Image Restoration – Historical Review . . . . .	2
1.1.1 Imaging System Model . . . . .	4
1.1.2 Restoration Metric . . . . .	6
1.1.3 Filter Synthesis . . . . .	7
1.1.4 Filter Implementation . . . . .	8
1.2 Problem Definition and Research Contribution . . . . .	10
1.3 Dissertation Outline . . . . .	12
<b>CHAPTER II. TRADITIONAL FREQUENCY-DOMAIN IMAGE</b>	
<b>RESTORATION</b>	<b>15</b>
2.1 A D/D Imaging System Model . . . . .	15
2.2 D/D Model-Based Simulation . . . . .	19
2.3 D/D Model-Based Restoration . . . . .	23
2.3.1 Inverse Restoration Filter . . . . .	25
2.3.2 Wiener Restoration Filter . . . . .	28

2.3.3	CLS Restoration Filter . . . . .	31
2.4	D/D Model Limitations . . . . .	37

## CHAPTER III. SAMPLED IMAGING SYSTEMS AND DIGITAL

### IMAGE RESTORATION 45

3.1	A C/D/C Imaging System Model . . . . .	45
3.1.1	Coordinate System . . . . .	46
3.1.2	Image Formation . . . . .	47
3.1.3	Image Sampling and Additive Random Noise . . . . .	50
3.1.4	Digital Processing . . . . .	52
3.1.5	Image Reconstruction . . . . .	52
3.2	C/D/C Model-Based Simulation . . . . .	54
3.2.1	Scene Representation . . . . .	55
3.2.2	Image Acquisition . . . . .	56
3.2.3	Image Sampling . . . . .	57
3.2.4	Digital Processing . . . . .	59
3.2.5	Image Reconstruction . . . . .	59
3.2.6	C/D/C Model Simulation Examples . . . . .	61
3.3	C/D/C Model-Based Digital Image Restoration . . . . .	62

## CHAPTER IV. C/D/C MODEL-BASED WIENER IMAGE RESTORATION 72

4.1	Wiener Filter Derivation . . . . .	72
-----	------------------------------------	----

4.2	Wiener Restoration Problems . . . . .	80
4.2.1	Conceptual Problems . . . . .	80
4.2.2	Computational Problems . . . . .	82
4.3	Simulated Wiener Restorations . . . . .	83
 <b>CHAPTER V. C/D/C MODEL-BASED CLS IMAGE RESTORA-</b>		
<b>TION</b>		<b>88</b>
5.1	CLS Filter Derivation . . . . .	89
5.2	CLS Filter Computation . . . . .	94
5.3	Simulated CLS Restorations . . . . .	98
 <b>CHAPTER VI. SPATIAL DOMAIN IMPLEMENTATION OF THE</b>		
<b>C/D/C MODEL-BASED CLS RESTORATION FILTER</b>		<b>112</b>
6.1	Spatial Domain Restoration . . . . .	112
6.2	Small CLS Restoration Kernels . . . . .	115
6.3	Simulated Small-Kernel CLS Restorations . . . . .	119
 <b>CHAPTER VII. CLS RESTORATION OF FORWARD-LOOKING</b>		
<b>INFRARED IMAGERY</b>		<b>125</b>
7.1	CLS Restoration of FLIR Imagery . . . . .	126
 <b>CHAPTER VIII. CLS RESTORATION OF SATELLITE-BORNE</b>		
<b>SCANNING RADIOMETER DATA</b>		<b>133</b>
8.1	ERBE System Model . . . . .	134

8.1.1	ERBE Coordinate System . . . . .	134
8.1.2	ERBE Image Acquisition . . . . .	135
8.1.3	Shift-variant Image Restoration . . . . .	137
8.2	Simulation Results . . . . .	138
<b>CHAPTER IX. CONCLUSIONS</b>		<b>148</b>
9.1	Conclusions . . . . .	148
9.2	Future Research . . . . .	150
9.2.1	Optimal regularization . . . . .	150
9.2.2	Adaptive CLS Restoration . . . . .	150
9.2.3	Color (Multi-spectral) CLS Restoration . . . . .	151
<b>Appendix A</b>		<b>152</b>
<b>BIBLIOGRAPHY</b>		<b>156</b>

## Acknowledgements

I am deeply grateful for the education, encouragement and help that I have received from my advisor, Dr. Stephen K. Park, throughout my career as a graduate student. This dissertation would not have been possible without his guidance and nurturing. Dr. Park's contribution to my life goes far beyond this dissertation and I am honored to have had the opportunity of working with him. I would also like to thank Dr. Paul Stockmeyer, Dr. Richard Prosl, Dr. James Howe, Dr. Mark Hinders and Dr. G. L. Smith for serving on my dissertation committee.

I am indebted to Dr. Stephen Reichenbach for being so very generous with his image processing software and advice. His help shortened considerably the coding process for this dissertation. A special "thank you" is reserved for Dr. (Lou) Smith whose unwavering faith in my abilities was a source of comfort on days when I seemed to lose that faith.

My wife Mousumi and my daughter Dia deserve a special "thank you" for their support and understanding throughout the dissertation process, especially the "down" periods when I must not have been a very easy person to live with. I am also grateful to my good friends Christine and David for providing me with the comforts of home and family when I was alone in Virginia. Finally, I would like to thank my parents for their love and support. Without their sacrifices, I would not be where I am today.

## List of Figures

2.1	A discrete/discrete (d/d) imaging system model . . . . .	16
2.2	Four simulated 1-D OTFs. . . . .	21
2.3	Aerial scene and three simulated d/d model images. . . . .	24
2.4	Inverse filter restorations with no additive random noise. . . . .	27
2.5	Inverse filter restorations with quantization noise. . . . .	29
2.6	Wiener filter restorations with quantization noise. . . . .	32
2.7	CLS filter restorations with quantization noise. . . . .	35
2.8	1-D CLS filter frequency response. . . . .	36
2.9	Blurred, sampled and pixel-replicated images. . . . .	39
2.10	Inverse filter restoration of pixel-replicated images. . . . .	41
2.11	Blurred, sampled and sinc-interpolated images. . . . .	42
2.12	Inverse filter restoration of sinc-interpolated images. . . . .	43
3.1	A continuous/discrete/continuous (c/d/c) imaging system model . .	46
3.2	A c/d/c model coordinate system . . . . .	48
3.3	Image acquisition OTFs. . . . .	58
3.4	Image reconstruction RTFs: [a] Sum of two Gaussians, [b] PCC. . .	60
3.5	PCC reconstruction of the blurred and sampled aerial scene (no restoration). . . . .	63

3.6	Display reconstruction of the blurred and sampled aerial scene (no restoration). . . . .	64
3.7	Reconstructed aerial and component images (no restoration). . . . .	69
3.8	High-pass filtered aerial and component images. . . . .	70
4.1	Simulated c/d/c model-based Wiener restorations. . . . .	86
4.2	$\ p - p'\ ^2$ versus $\mu$ . . . . .	87
5.1	C/d/c model-based CLS restorations with SNR = 50. . . . .	100
5.2	C/d/c model-based CLS restorations with SNR = 10. . . . .	102
5.3	C/d/c model-based CLS filter responses for different SNRs. . . . .	103
5.4	PCC reconstruction of aerial scene with different sampling grids. . .	105
5.5	C/d/c model-based CLS restorations with different sampling grids. .	107
5.6	C/d/c model-based CLS filter responses with different sampling grids.	108
5.7	C/d/c model-based CLS restorations corresponding to different user-supplied high-pass filters. . . . .	109
5.8	C/d/c model-based CLS filter responses with different user-supplied high-pass filters. . . . .	110
6.1	Spatially unconstrained and three small-kernel CLS restorations. . .	122
6.2	Difference images for spatially unconstrained and small-kernel CLS restorations. . . . .	123

7.1	Unprocessed actual images at distances of 100 <i>m</i> to 800 <i>m</i> at 100 <i>m</i> intervals. . . . .	129
7.2	100 <i>m</i> reference image and PCC reconstructions of 200 <i>m</i> to 800 <i>m</i> images. . . . .	130
7.3	100 <i>m</i> reference image and CLS restorations of 200 <i>m</i> to 800 <i>m</i> images.	131
8.1	Imaging geometry and coordinate systems. . . . .	136
8.2	Simulated cosine radiance field. . . . .	139
8.3	ERBE scanning radiometer PSF. . . . .	141
8.4	Footprint growth in the along-track direction with scan angle. . . .	144
8.5	Restored versus unrestored digital image. . . . .	145
8.6	Restored versus unrestored TOA reconstructions. . . . .	146



## Abstract

The design of a digital image restoration filter must address four concerns: the completeness of the underlying imaging system model, the validity of the restoration metric used to derive the filter, the computational efficiency of the algorithm for computing the filter values and the ability to apply the filter in the spatial domain. Consistent with these four concerns, this dissertation presents a constrained least-squares (CLS) restoration filter for digital image restoration. The CLS restoration filter is based on a comprehensive, continuous-input/discrete-processing/continuous-output (c/d/c) imaging system model that accounts for acquisition blur, spatial sampling, additive noise and imperfect image reconstruction. The c/d/c model-based CLS restoration filter can be applied rigorously and is easier to compute than the corresponding c/d/c model-based Wiener restoration filter. The CLS restoration filter can be efficiently implemented in the spatial domain as a small convolution kernel. Simulated restorations are used to illustrate the CLS filter's performance for a range of imaging conditions. Restoration studies based, in part, on an actual Forward Looking Infrared (FLIR) imaging system, show that the CLS restoration filter can be used for effective range reduction. The CLS restoration filter is also successfully tested on blurred and noisy radiometric images of the earth's outgoing radiation field from a satellite-borne scanning radiometer used by the National Aeronautics and Space Administration (NASA) for atmospheric research.

**CONSTRAINED LEAST-SQUARES DIGITAL IMAGE  
RESTORATION**

# INTRODUCTION

## 1.1 Digital Image Restoration – Historical Review

Digital image *processing* is the art and science of manipulating digital images. The wide range of digital image processing applications include scientific, military and commercial imaging, forensic medicine, and remote sensing. Digital image *restoration*, the focus of this dissertation, addresses one of the central problems in digital image processing — the design and implementation of algorithms for removing image degradations.

Digital image formation introduces inevitable degradations that adversely affect the quality of a digital image.<sup>1</sup> Degradations are introduced by the imaging system (optical blur, electronic noise, spatial sampling) and, perhaps, by external sources (camera motion, object motion). In an authoritative but now dated textbook on the subject, Andrews and Hunt [1] provide a succinct formulation of the general image restoration problem — given a degraded digitized representation (image) of a scene, compute an estimate of the original scene based on *a priori* knowledge about the processes that caused the degradations. Despite significant advances in digital imaging technology, for some important applications digital image restoration remains a problem of significant interest [2]–[5].

Although digital image restoration and computers are now intimately connected,

---

<sup>1</sup>In this dissertation image *quality* is used in a subjective sense to denote the degree to which a reconstructed image is an accurate representation of an original scene.

the history of image restoration pre-dates the digital computer era. Before the widespread availability of digital computers and digital imaging systems, *analog* image restoration received serious attention with the pioneering work of Mertz et al. [6] and later work by Elias et al. [7] and Linfoot [8]. This research quantified the major sources of image degradation in then contemporary analog imaging systems such as television and film cameras. The practitioners of analog image processing noted, however, that the inherent mathematical complexity of the image restoration problem far exceeded their ability to use optical (analog) methods to compensate for imperfect imaging instruments. Thus, analog image restoration sensitized the scientific community to the possibility of image restoration, but failed to provide a satisfactory solution to the image restoration problem.

The advent of digital imaging systems and digital computers provided a great opportunity for *digital* image restoration practitioners. Most digital imaging systems provide a natural numeric representation for images as two-dimensional arrays. This array representation is amenable to the sophisticated numerical computations required to solve the image restoration problem; digital computers provide the ability to perform these computations in a reasonable amount of time. Early research conducted at NASA's Jet Propulsion Laboratories illustrated the success of digital restoration techniques by showing that significant improvements in image quality could be achieved with computing resources that were modest by today's standards [9]. Since then, the field has grown tremendously; its maturity can be judged

by the number of journals and image processing texts that devote substantial attention to digital image restoration.

Image restoration practitioners model the imaging process, then attempt to recover the scene by constructing a restoration filter to “undo” (invert) the processes that degraded the image.<sup>2</sup> Given this model-based goal of attempting to recover the original scene, a digital image restoration study has to address four related issues:

- the input-output model of the imaging system;
- the performance measure (metric) to be optimized by the restoration filter;
- the algorithm used to compute the restoration filter;
- the computational complexity of the restoration filter implementation.

### 1.1.1 Imaging System Model

Three types of *linear* imaging system models are common in the image restoration literature. Historically, the first of these is a *continuous-input/continuous-output* (c/c) system model commonly used by the analog image processing community to analyze the performance of conventional film camera systems [8]. This type of model allows for system noise and multiple cascaded filtering steps; the filters account for all the system components that contribute to the low-pass filtering

---

<sup>2</sup>Image *restoration* differs from image *enhancement* in that the latter uses ad-hoc techniques, not based on an imaging system model. Examples of image enhancement include contrast stretching and histogram-based image modification.

effects of image formation. In a *c/c* model the mathematical representation of the image at any filtering step is a function defined for a two-dimensional continuum of spatial locations. For this reason, a *c/c* model is not applicable to the analysis of *sampled* imaging systems and the design of *digital* image restoration filters.

The second type of linear model is a *discrete-input/discrete-output* (*d/d*) system model. This system model is a discrete approximation to a *c/c* system model; the image at any filtering step is a two-dimensional array. A *d/d* model is the most commonly used imaging system model in the image restoration literature today [5]; it is not directly applicable to the analysis of sampled imaging systems, however. That is, as demonstrated in chapter 2, a *d/d* model ignores two potentially important sources of image degradation in sampled imaging systems — spatial sampling and image reconstruction.

A comprehensive end-to-end performance analysis of a *sampled* imaging system must be based on a model that accounts for the continuous-to-discrete sampling process and the discrete-to-continuous reconstruction process. These processes produce pixel-scale sampling artifacts in digital images and subtle differences in the visual quality of these images when reconstructed by different display devices (such as a CRT or film) [10][11]. Models that are either entirely discrete (*d/d* models) or entirely continuous (*c/c* models) cannot properly account for sampling and reconstruction. Instead, a model that uses *both* continuous and discrete representations as appropriate is required. A linear *continuous-input/discrete-processing/continuous-*

*output* (c/d/c) model satisfies this requirement [12]. A c/d/c model is more complex than either a c/c or a d/d model. As demonstrated in several recent papers, however, this complexity is not so great as to prohibit the design of digital restoration filters [13][14]. The constrained least-squares restoration technique described in this dissertation is based on a c/d/c imaging system model.

### 1.1.2 Restoration Metric

The second image restoration issue is the choice of a quantitative performance measure (restoration metric) that the restoration filter attempts to optimize. Restoration metrics have been investigated since the early days of film cameras and television by, for example, Linfoot [15], Mertz et al. [16] and Budrikis [17]. If an imaging system produces visual output (this is the usual case), the restoration metric should correlate well with the human visual system. In this application, however, the extremely subjective nature of human image interpretation coupled with a still incomplete model of the human visual system makes the design of accurate restoration metrics a challenging problem that remains an active research area [18]–[24].

With a few exceptions, most restoration metrics fall into one of the following categories: *subjective* or *ad-hoc* metrics [25]; *maximum entropy* metrics [26]–[29]; *Bayesian* metrics [30]–[32] and *mean-square difference* metrics [33]–[43].<sup>3</sup> Most of the common restoration techniques use the mean-square difference (MSD) metric

---

<sup>3</sup>This list of references is not exhaustive; these references should be considered seminal work in each of the categories indicated.

to measure the degree to which one image matches another [44]. For example, the Wiener restoration filter attempts to minimize the end-to-end MSD between the ideal input scene and the restored output image.

The MSD metric originated in the scientific data processing literature, then received recognition as an image fidelity metric in the work of Linfoot [15]. Some critics of this metric have correctly pointed out that it does not always correlate well with human (subjective) judgement. Since it lends itself to linear system analysis using Fourier methods, however, it has been widely used. Moreover, as suggested in a recent article [45] and clearly demonstrated in this dissertation, much of this criticism of the MSD is misplaced in the sense that unsatisfactory restoration may be the result of using a d/d system model when a c/d/c system model should have been used instead.

### 1.1.3 Filter Synthesis

The third image restoration issue is the algorithm for synthesizing (computing) the restoration filter. Generally, the greater the mathematical sophistication of the restoration filter, the greater the computational demands of the associated algorithm for computing the filter values. For that class of applications where the imaging system is fixed and the restoration filter can be designed independent of the scene (e.g., the inverse filter), the restoration filter values need to be computed once only; if so, algorithm efficiency is not an important issue.

Most practical digital restoration applications are not so simple, however. The



properties of the imaging system change over time, either by necessity (e.g., because different camera settings are used) or inadvertently (e.g., because of operating condition changes in electronic components). Moreover, the use of sophisticated restoration filters that are optimized to a particular scene necessitates the (re)computation of the restoration filter values if the scene changes. Computationally efficient filter synthesis is thus an important issue, especially if timing constraints are placed on the entire filter synthesize-and-implement cycle, as is usually the case in real-time restoration applications (e.g., digital video and television).

One practical advantage of the constrained least-squares (CLS) restoration filter presented in this dissertation is the relative simplicity of the filter synthesis algorithm. Unlike the algorithm for computing the  $c/d/c$  model-based Wiener filter values, it is not necessary to estimate the (unknown) energy spectrum of the scene and the noise. Instead, the  $c/d/c$  model-based CLS restoration filter values can be computed directly from a knowledge of the imaging system.

#### 1.1.4 Filter Implementation

The last image restoration issue is efficient filter implementation. Although processor and memory access speeds continue to improve, the restoration of a typical  $512 \times 512$  (or larger) digital image in near real-time remains a challenge. For image restoration to be practical in real-time applications, efficient implementation considerations must be an integral part of the restoration filter design process.

Traditional linear restoration filters such as the Wiener filter and the CLS filter

are *designed* in the frequency domain, thereby suggesting the frequency domain as the natural domain for *implementing* the restoration filter as well. A frequency domain implementation is problematic, however, because a substantial amount of computer memory is required to compute and store the restoration filter coefficients and the discrete Fourier transform (DFT) of the digital and restored images. Moreover, even if fast Fourier transform (FFT) algorithms are used to compute forward and inverse DFTs, a frequency domain implementation requires significant processing power. In contrast, digital restoration implemented as a convolution in the spatial domain using *small* restoration filter kernels requires less memory and modest processing power [47]. Additionally, the spatial domain approach is amenable to direct hardware implementation.

The efficient spatial domain implementation of digital restoration filters has been addressed in the context of a d/d system model [48]–[53]. Recently, Reichenbach et al. demonstrated a similar technique for designing a c/d/c model-based Wiener restoration filter kernel, subject to explicit spatial constraints [47]. Using this technique, implementation efficiency is achieved by restricting the size of the restoration filter to a small convolution kernel. This dissertation applies Reichenbach et al.’s small-kernel technique to the c/d/c model-based CLS restoration filter. Doing so makes it possible to use the CLS restoration filter in future high-performance digital imaging systems that may use “in-line” digital processing.

## 1.2 Problem Definition and Research Contribution

As discussed in section 1.1.1, most contemporary digital image restoration filters are conditioned on a d/d system model. Since a d/d model does not account for sampling and reconstruction, the applicability of these restoration filters to digital image data is questionable. In recent years, a c/d/c model-based Wiener restoration filter has been derived that is directly applicable to sampled image data [13][14]. Although this filter is based on a proper underlying system model, it cannot be applied rigorously. That is, although a c/d/c model-based Wiener filter is *optimal* in an end-to-end expected MSD sense, this optimality is conditioned on a knowledge of the energy spectra of the unknown stochastic scene and additive random noise as well as on statistical assumptions that the noise is signal-independent and the scene's sidebands are uncorrelated [12]. In practice, the energy spectra of the scene and noise are never known and the validity of the statistical assumptions are impossible to verify. Consequently, every practical Wiener filter application is necessarily *sub-optimal* (and maybe inaccurate); a c/d/c model-based Wiener restoration filter is an important *theoretical* tool, but one whose direct practical usefulness is limited.

This dissertation provides a viable alternative to the c/d/c model-based Wiener restoration filter. The specific dissertation contributions are summarized by the following four points.

- Simulation is used to illustrate that if imaging systems employ sampling and reconstruction, then image restoration should be conditioned on a c/d/c imag-

ing system model.

- A  $c/d/c$  model-based CLS restoration filter derivation is presented that does not rely on the statistical assumptions required by the  $c/d/c$  model-based Wiener filter. The computation of the restoration filter values is correspondingly easier in the sense that no *a priori* knowledge about the energy spectra of the stochastic scene and the additive random noise is required.
- To facilitate hardware implementation in real-time applications, a method for constraining the  $c/d/c$  model-based CLS restoration filter to a small convolution kernel is provided. Use of this method allows the restoration filter to be efficiently implemented in the spatial domain as a small-kernel convolution.
- Two different image restoration applications are presented to demonstrate that the  $c/d/c$  model-based CLS restoration filter is practical and effective. In one application, a thermal imaging system is simulated to demonstrate that the  $c/d/c$  model-based CLS restoration filter can significantly improve the quality of thermal images. In the other application, the  $c/d/c$  model-based CLS restoration filter is used to restore radiometric data from a simulated satellite-borne scanning radiometer.

### 1.3 Dissertation Outline

As outlined in this introductory chapter, a practical digital image restoration filter is developed in this dissertation that is based on a comprehensive  $c/d/c$  imaging system model and a MSD restoration metric. The algorithm for computing the restoration filter values is efficient and the restoration filter can be implemented in the spatial-domain as a small-kernel convolution.

Chapter 2 describes a  $d/d$  system model and three different  $d/d$  model-based restoration filters — the inverse filter, the Wiener filter and the CLS filter. The applicability of a  $d/d$  system model to sampled imaging systems is examined via simulation. In this way, it is demonstrated that  $d/d$  model-based restoration filters can enhance the unwanted effects of sampling and image reconstruction. The discussion in this chapter is used to motivate the need to use a more comprehensive  $c/d/c$  system model and associated restoration filter.

Chapter 3 describes a  $c/d/c$  system model. Factors that limit the ability of  $c/d/c$  model-based restoration filters to sharpen digital images are discussed. In particular, the limiting effect of sampling and reconstruction is examined via simulation. It is shown that degradations caused by sampling and reconstruction limit image restoration, much in the same manner as additive noise.

Chapter 4, describes a  $c/d/c$  model-based Wiener restoration filter. A derivation of the filter is presented with special emphasis on the statistical assumptions required. Using simulation, it is shown that reasonable implementations of this  $c/d/c$

model-based Wiener filter are sub-optimal and that restoration accuracy varies with the type of parametric model used to characterize the scene's energy spectrum.

Chapter 5 presents a  $c/d/c$  model-based CLS restoration filter as an alternative to the corresponding Wiener filter. The derivation of the filter is presented in detail along with a discussion of frequency domain implementation issues. Simulated restorations are provided to demonstrate the effectiveness of the  $c/d/c$  model-based CLS restoration filter.

Chapter 6 presents a technique for generating a small  $c/d/c$  model-based CLS restoration filter kernel. This technique allows the CLS restoration filter to be applied in the spatial domain as a small-kernel convolution. Simulated restorations using small CLS restoration kernels are presented to demonstrate the effectiveness of this technique.

Chapter 7 presents a simulation-based study of the  $c/d/c$  model-based CLS filter based, in part, on infrared images acquired by a Forward Looking Infrared (FLIR) image acquisition system. Practical advantages of the CLS filter over the Wiener filter are emphasized.

Chapter 8 presents an application of the  $c/d/c$  model-based CLS restoration filter in the context of a satellite-borne scanning radiometer. This application demonstrates that the  $c/d/c$  model-based CLS filter can be adapted to certain types of shift-variant imaging systems and applied in non-traditional image restoration applications where there is little or no *a priori* knowledge about the spectral

characteristics of the input scene.

Chapter 9 concludes with a summary of results and ideas for future research. In particular, possible ways of using a c/d/c model-based CLS restoration filter as an adaptive restoration filter to account for stochastic imaging systems and non-homogeneous scenes are outlined.

## CHAPTER II

### TRADITIONAL FREQUENCY-DOMAIN IMAGE RESTORATION

An incomplete *discrete-input/discrete-output* (d/d) imaging system model is commonly used for image restoration studies. Simulated restorations are presented in this chapter for three different d/d model-based restoration filters — the inverse filter, the Wiener filter and the constrained least-squares (CLS) filter. It is demonstrated that when image acquisition blur is the *only* significant source of image degradation, all three d/d model-based restoration filters can successfully sharpen blurred digital images, even when the blurring is excessive. If a small amount of additive random noise is also a source of image degradation, however, then only the more sophisticated Wiener and CLS filters can produce satisfactory restorations. Moreover, if sampling and reconstruction are part of the imaging process, but are not included in the system model, all d/d model-based inverse restoration filters fail to restore satisfactorily, even when additive random noise is absent. In this way, it is demonstrated that a d/d model is *not* a correct sampled imaging system model.

#### 2.1 A D/D Imaging System Model

A d/d imaging system model is illustrated in figure (2.1). As evident from its name, a d/d model takes a discrete view of the world — all model components



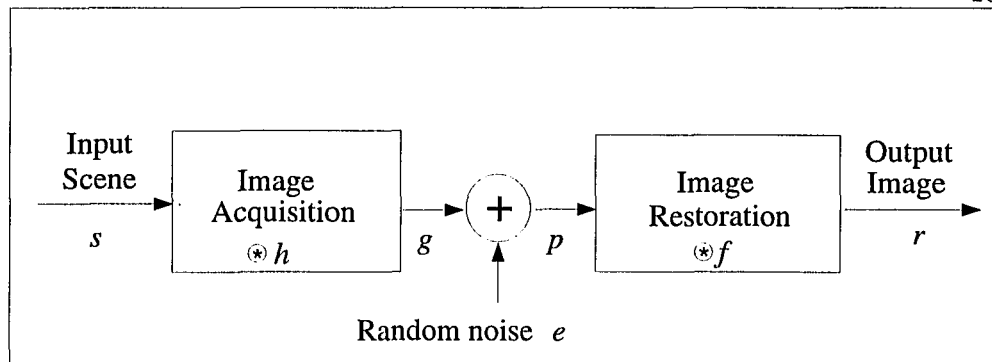


Figure 2.1: A discrete/discrete (d/d) imaging system model

are represented as (discrete) two-dimensional arrays. This array representation facilitates the implementation of image restoration algorithms and helps explain the unrestricted use (and mis-use) of a d/d model in image restoration studies.

The input scene in figure (2.1) is an array  $s$  corresponding to a degradation-free scene. The scene is assumed to be periodic with period  $N_1 \times N_2$ . Although the periodicity assumption is artificial with the potential for introducing artifacts, the artifacts are generally negligible except at the natural boundaries of the scene. Moreover, the periodicity assumption facilitates the use of Fourier analysis and is no more artificial than other common techniques (e.g., windowing or padding) for dealing with finite  $N_1 \times N_2$  images.

Image acquisition is modeled as a convolution of the input scene with an aperiodic array  $h$  that represents the point spread function (PSF) of the image acquisition system. That is,  $g = s \otimes h$  where

$$g[n_1, n_2] = \sum_{n'_1=-\infty}^{\infty} \sum_{n'_2=-\infty}^{\infty} h[n'_1, n'_2] s[n_1 - n'_1, n_2 - n'_2]. \quad (2.1)$$

The array  $g$  is a blurred image of the scene. Consistent with the assumed periodicity

of the input scene,  $g$  is also periodic with period  $N_1 \times N_2$ .

Equation (2.1) can be written equivalently in the frequency domain, using the (discrete) convolution theorem, as

$$\hat{g}[\nu_1, \nu_2] = \hat{h}[\nu_1, \nu_2] \hat{s}[\nu_1, \nu_2] \quad (2.2)$$

where  $\nu_1, \nu_2$  are integer-valued frequency indices and the arrays  $\hat{g}, \hat{s}$  are the discrete Fourier transform (DFT) arrays corresponding to  $g, s$  respectively. That is,

$$\hat{s}[\nu_1, \nu_2] = \frac{1}{N_1 N_2} \sum_{n_1=0}^{N_1-1} \sum_{n_2=0}^{N_2-1} s[n_1, n_2] \exp(-i2\pi n_1 \nu_1 / N_1) \exp(-i2\pi n_2 \nu_2 / N_2) \quad (2.3)$$

and  $\hat{g}[\nu_1, \nu_2]$  is defined analogously. The optical transfer function (OTF) of the image acquisition system is the array  $\hat{h}$  defined by the  $z$ -transform of the PSF array evaluated at the normalized spatial frequencies  $[\nu_1/N_1, \nu_2/N_2]$ . That is, the OTF array is

$$\hat{h}[\nu_1, \nu_2] = \sum_{n_1=-\infty}^{\infty} \sum_{n_2=-\infty}^{\infty} h[n_1, n_2] \exp(-i2\pi n_1 \nu_1 / N_1) \exp(-i2\pi n_2 \nu_2 / N_2). \quad (2.4)$$

The digital image  $p$  is a noisy version of the blurred scene, expressed in the spatial domain as

$$p[n_1, n_2] = g[n_1, n_2] + e[n_1, n_2] \quad (2.5)$$

where  $e[n_1, n_2]$  is an additive random noise array. Additive random noise represents measurement uncertainty due to stochastic variations in the electronic components of the image acquisition system and analog-to-digital conversion. To make the array  $p$  periodic, the additive random noise array is assumed to be periodic with period

$N_1 \times N_2$ . The periodicity of  $p$  allows its DFT array to be expressed as

$$\hat{p}[\nu_1, \nu_2] = \hat{g}[\nu_1, \nu_2] + \hat{e}[\nu_1, \nu_2] = \hat{s}[\nu_1, \nu_2] \hat{h}[\nu_1, \nu_2] + \hat{e}[\nu_1, \nu_2] \quad (2.6)$$

where  $\hat{e}$  is the DFT array corresponding to  $e$ .

Linear, shift-invariant image restoration is modeled as a convolution of  $p$  with a restoration filter array  $f$  to produce the output image  $r = p \otimes f$ . The restoration filter array is assumed to be periodic with period  $N_1 \times N_2$ . The assumed periodicity of  $f$  allows its frequency response to be represented by its DFT array, facilitating the use of frequency domain techniques to design the filter. The output image array is periodic with period  $N_1 \times N_2$ ; the corresponding DFT array is

$$\hat{r}[\nu_1, \nu_2] = \hat{p}[\nu_1, \nu_2] \hat{f}[\nu_1, \nu_2] = \left( \hat{s}[\nu_1, \nu_2] \hat{h}[\nu_1, \nu_2] + \hat{e}[\nu_1, \nu_2] \right) \hat{f}[\nu_1, \nu_2] \quad (2.7)$$

where  $\hat{f}$  is the restoration filter DFT array.

Equation (2.7) provides a complete end-to-end characterization of the d/d model in the frequency domain. That is, given the transform arrays  $\hat{h}$ ,  $\hat{e}$  and  $\hat{f}$ , equation (2.7) uniquely defines the output image DFT array in terms of the input scene DFT array. All of the arrays  $\hat{s}$ ,  $\hat{h}$ ,  $\hat{e}$ ,  $\hat{f}$  and  $\hat{r}$  are complex-valued and periodic with period  $N_1 \times N_2$ . The inverse DFT array

$$r[n_1, n_2] = \sum_{\nu_1=0}^{N_1-1} \sum_{\nu_2=0}^{N_2-1} \hat{r}[\nu_1, \nu_2] \exp(i2\pi n_1 \nu_1 / N_1) \exp(i2\pi n_2 \nu_2 / N_2). \quad (2.8)$$

defines the output image in the spatial domain.

## 2.2 D/D Model-Based Simulation

Model-based simulation is commonly used to analyze different restoration techniques for a variety of system operating conditions (blur and random noise). A d/d model-based simulation can be implemented in the spatial domain or in the frequency domain. The two approaches are *mathematically* equivalent and, except for the effects of finite-precision arithmetic, yield identical results. A frequency domain implementation is generally preferred, however, due to the insight it provides into the restoration process and the computational efficiency gained by replacing convolutions in the spatial domain (e.g., equation (2.1)), with (complex-valued) multiplications in the frequency domain (e.g., equation (2.2)).

An example of an input scene  $s$  is shown in figure (2.3[a]). This  $512 \times 512$  aerial image is a good choice for a test scene because it has high contrast and contains both high-frequency pixel-scale features and low-frequency region-scale features; with such an input scene it is possible to test the ability of a restoration filter to sharpen blurred scene features without producing excessive noise enhancement.

To simulate image acquisition using equation (2.2), it is necessary to select a model for the OTF. A variety of OTF models have been used in d/d model-based restoration studies to simulate different types of image acquisition characteristics; these range from simplistic low-pass filter models with little theoretical justification to more realistic models that attempt to capture the effects of optical blurring, detector blurring, jitter and relative motion between the scene and the image ac-

quisition system. *Parametric* models are commonly used to account for varying degrees of image acquisition blur. One such parametric model is the (separable) discrete, Gaussian OTF

$$\hat{h}[\nu_1, \nu_2] = \exp\left(-\frac{(\nu'_1/N_1)^2}{\sigma_1^2}\right) \exp\left(-\frac{(\nu'_2/N_2)^2}{\sigma_2^2}\right) \quad (2.9)$$

where  $\nu'_1 = |\nu_1| \bmod N_1$  and  $\nu'_2 = |\nu_2| \bmod N_2$ . Consistent with equation (2.4), the ‘mod’ makes the  $\hat{h}$  array periodic with period  $N_1 \times N_2$ . The OTF parameters  $\sigma_1, \sigma_2$  control the two-dimensional frequency response of the image acquisition system; small values produce excessive blurring and vice versa. The units of  $\sigma_1, \sigma_2$  are cycles per “scene pixel” (*scenel*). Typical values of  $\sigma_1, \sigma_2$  range from 0.04 (severe blur) to 0.25 (moderate blur). Figure (2.2) illustrates four 1-D Gaussian OTFs for OTF parameter values of 0.25, 0.10 and 0.04; the  $\sigma = \infty$  case represents a perfect image acquisition system.<sup>1</sup>

Additive random noise  $e$  is usually assumed to be scene-independent and zero-mean. This assumption simplifies the design of d/d model-based restoration filters and is justified, in part, by some d/d model-based studies indicating that there is very little modeling accuracy to be gained by using a scene-dependent additive random noise model [54]. The effect of zero-mean additive random noise is quantified by a *Signal-to-Noise Ratio* (SNR) parameter that characterizes the level of noise

---

<sup>1</sup>Although the Gaussian OTF in equation (2.9) is discrete, in figure (2.2) it is plotted as a continuous function of the normalized frequency  $\nu/N$ .

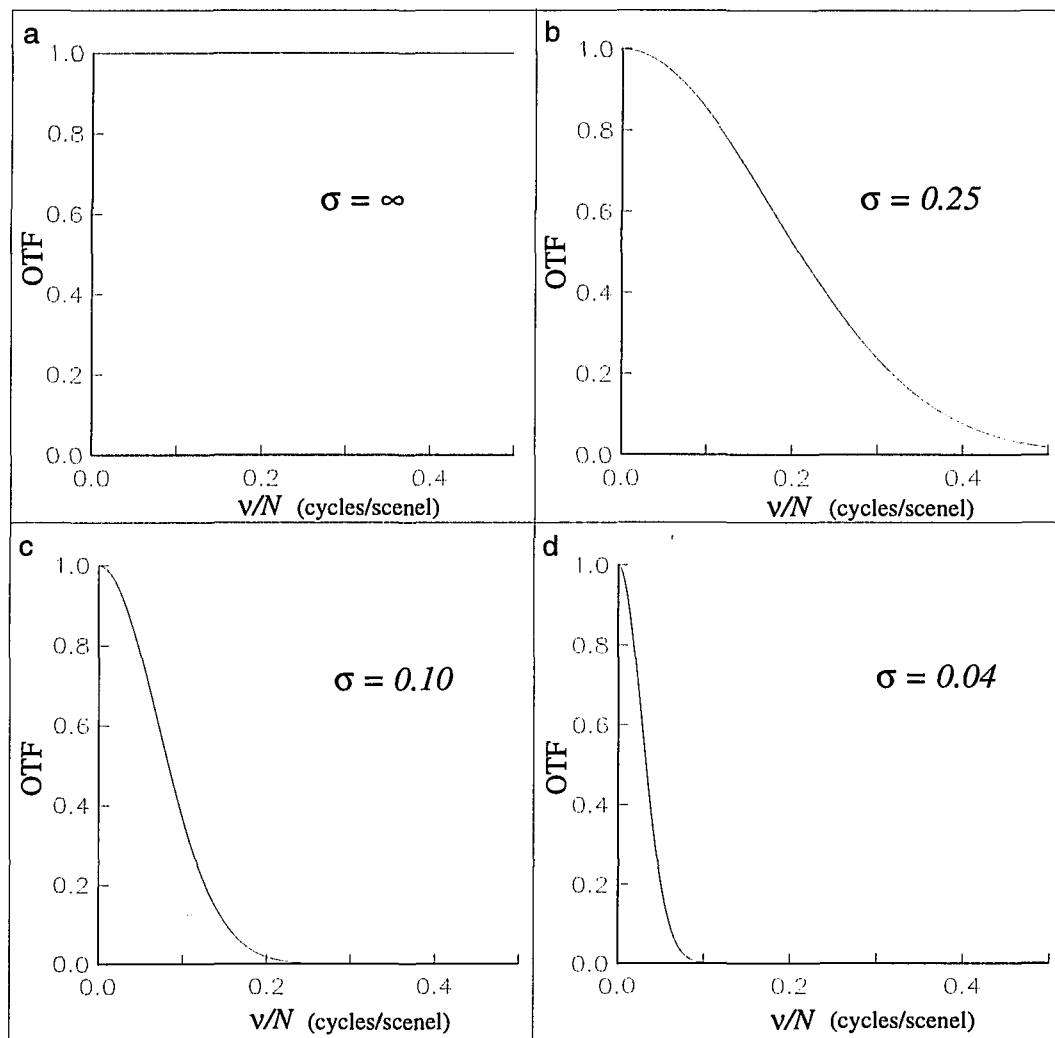


Figure 2.2: Four simulated 1-D OTFs.

relative to the input scene. The definition of SNR used in this dissertation is

$$\text{SNR} = \frac{\sigma_s}{\sigma_e} \quad (2.10)$$

where  $\sigma_s$  and  $\sigma_e$  are the standard deviations (contrasts) of the scene and noise respectively [55]. By definition, SNR is a dimensionless quantity. Large values of SNR (greater than 1000) denote a relatively noise-free image; small values (less than 10) denote an extremely noisy image.

For a digital imaging system, one unavoidable source of additive random noise is *quantization*. Relative to figure (2.1), quantization is additive noise produced by analog-to-digital conversion (by rounding); that is,  $g$  has a floating-point representation and  $p$  has a limited-precision (unsigned) integer representation. Quantization results in some clipping for values of  $g$  (if any) beyond the range of representable integer values as well as round-off error for the values within this range. As demonstrated in the following section, quantization noise can pose serious problems for a d/d model-based restoration filter.<sup>2</sup>

For the d/d model, restoration is implemented in the frequency domain using equation (2.7) with the restoration filter of choice. The restored image is then obtained using equation (2.8). Examples of d/d model-based restoration are presented

---

<sup>2</sup>If appropriate, random noise from other sources can be simulated by adding random integer values (positive or negative) drawn from a discrete distribution, for example, the Poisson. If random noise had been added in this manner,  $\sigma_e^2$  would be the sum of the variances of the quantization noise and the random noise.

in section 2.3.<sup>3</sup>

Figure (2.3) is a four-panel composite of individual images. Figure (2.3[a]) is the  $512 \times 512$  aerial scene  $s$ . The other three images in figure (2.3) correspond to the image  $p = s \oplus h + e$  produced by a simulated d/d model with the OTF  $\hat{h}$  illustrated in the corresponding panel in figure (2.2). For example, the image in figure (2.3[b]) corresponds to the OTF illustrated in figure (2.2[b]). The additive term  $e$  is quantization noise. This four-panel format is used for all the remaining figures in this chapter. Consistent with the OTF frequency characteristics in figure (2.2), the images in figure (2.3) become increasingly more blurred as the OTF parameter is decreased.<sup>4</sup>

## 2.3 D/D Model-Based Restoration

The goal of image restoration is to make the restored image match the input scene. This section describes three d/d model-based image restoration filters that are designed in the frequency domain to achieve this purpose; they are the *inverse* filter, the *Wiener* filter and the *CLS* filter [1]. While these restoration filters are not the

---

<sup>3</sup>If it is necessary to normalize the restored image to the range of values that can be displayed by an analog output device such as a video monitor, this normalization must be done carefully. Ad-hoc normalization methods can create artifacts that may be erroneously attributed to the restoration process.

<sup>4</sup>Figure (2.3[a]) can be interpreted as the output image corresponding to a perfect image acquisition system with  $\sigma = \infty$ .



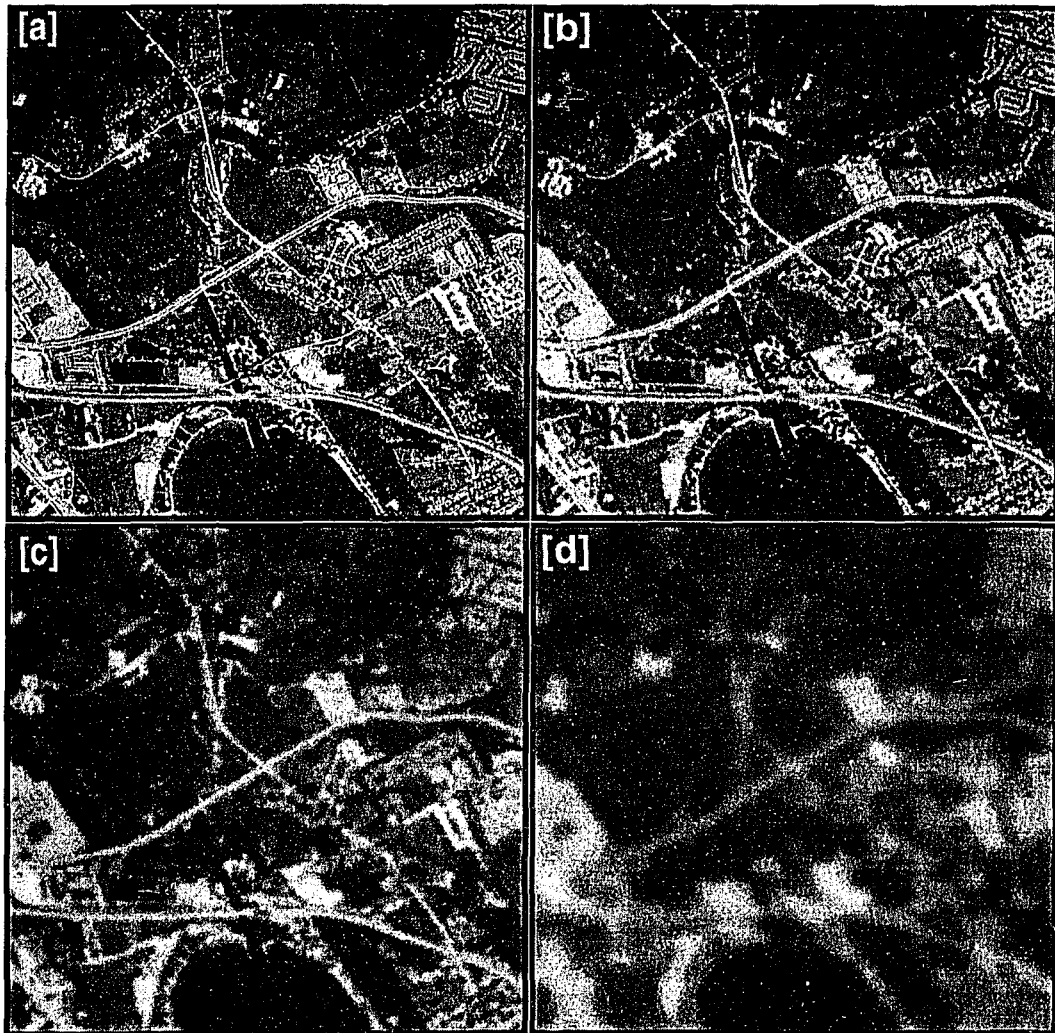


Figure 2.3: Aerial scene and three simulated d/d model images.

only d/d model-based restoration filters available, they have been widely used in the past and continue to be popular in image restoration applications today. As discussed in chapters 3, 4 and 5 (in the context of a c/d/c model), the derivation of all three restoration filters uses the MSD as the restoration metric. The inverse filter derivation minimizes the MSD between the scene and the restored image with the additive random noise ignored. The Wiener filter derivation minimizes the expected MSD between the scene and the restored image in the presence of additive random noise. The minimum MSD is used in the derivation of the CLS filter to select the “best” restored image from an infinity of possibilities.

### 2.3.1 Inverse Restoration Filter

The inverse restoration filter is defined as

$$\hat{f}[\nu_1, \nu_2] = \begin{cases} \frac{1}{\hat{h}[\nu_1, \nu_2]} & \hat{h}[\nu_1, \nu_2] \neq 0 \\ 0 & \text{otherwise.} \end{cases} \quad (2.11)$$

The design of this filter is based upon the observation that *in the absence of additive random noise*, the original scene can be recovered by “inverting” the effects of image acquisition. That is, if the inverse filter is used then, from equation (2.7), at those frequencies where  $\hat{h}[\nu_1, \nu_2] \neq 0$  the restored image DFT array is

$$\hat{r}[\nu_1, \nu_2] = \frac{\hat{p}[\nu_1, \nu_2]}{\hat{h}[\nu_1, \nu_2]} = \hat{s}[\nu_1, \nu_2] + \frac{\hat{e}[\nu_1, \nu_2]}{\hat{h}[\nu_1, \nu_2]} \quad (2.12)$$

From equation (2.12) it is clear that if  $\hat{h}[\nu_1, \nu_2] \neq 0$  and if  $\hat{e}[\nu_1, \nu_2] = 0$  for *all*  $[\nu_1, \nu_2]$ , then the restored image is identical to the scene.

Figure (2.4) is a four-panel composite illustration of inverse filter restorations. All three restorations are performed with *no* additive noise. That is, in each case the blurred scene, figure (2.3), is *not* quantized prior to restoration with the inverse filter.<sup>5</sup> The restored images are virtually indistinguishable from the original scene. Consistent with theory, this simulation illustrates that even if the blurring is excessive, as in figure (2.3[d]), the inverse restoration filter can remove essentially all the blurring caused by image acquisition *provided* additive random noise is non-existent.

The use of the inverse filter is limited in practice because digital images are not noise-free and at high frequencies the product  $\hat{s}[\nu_1, \nu_2]\hat{h}[\nu_1, \nu_2]$  may be small relative to  $\hat{e}[\nu_1, \nu_2]$ . If so, then as illustrated in equation (2.12), the random noise will be greatly boosted relative to the original scene and the restored image may be unacceptable because scene features will be masked by unwanted, enhanced random noise. To illustrate this, figure (2.5) is presented. This figure is the same as figure (2.4) except that the inverse filter is applied *after* 12-bit quantization. To simulate 12-bit quantization, the contrast of the 8-bit aerial image  $s$  was increased by multiplying each pixel value by 16. The real-valued array  $g = s \otimes h$  was then rounded to an integer-valued array with values in the range  $0 \dots 2^{12} - 1$ . This real-to-integer conversion produces quantization noise  $e$  corresponding to an  $\text{SNR} = 2400$  for each of the images  $p = s \otimes h + e$  in figure (2.3).<sup>6</sup>

---

<sup>5</sup>Relative to figure (2.1), this means that  $g = p$ .

<sup>6</sup>After multiplication by 16, the contrast of the scene is  $\sigma_s = 689.2$  and that of quantization noise is  $\sigma_e = 0.288$ .

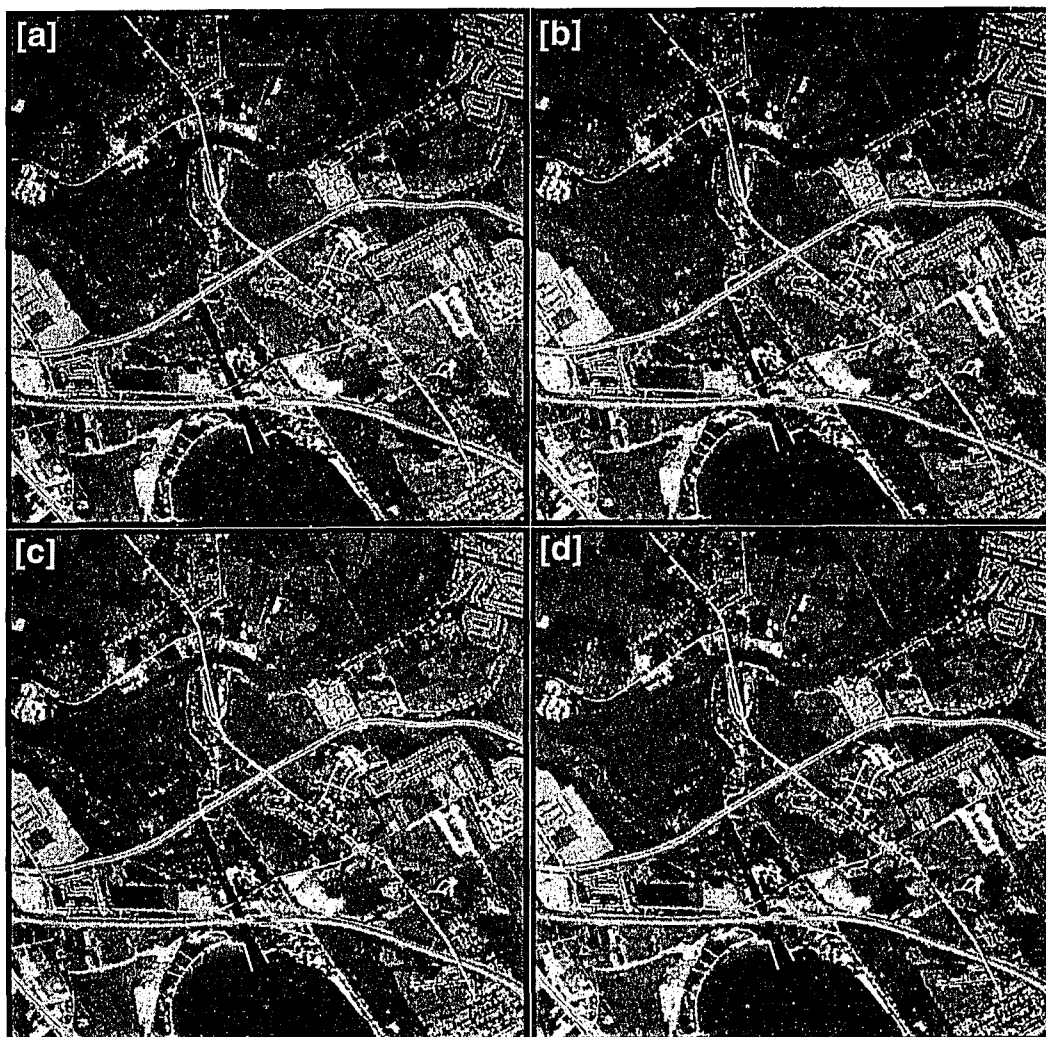


Figure 2.4: Inverse filter restorations with no additive random noise.

As is evident in figure (2.5), even if the SNR is high random noise enhancement can be a severe problem for the inverse filter. The restorations in figures (2.5[c]) and (2.5[d]) are virtually unrecognizable.<sup>7</sup> In comparison, the image in figure (2.5[b]) is a better restoration than the other two, but evidence of enhanced random noise is still quite apparent.

The inevitable enhancement of additive random noise by the inverse restoration filter is well-documented in the literature [2]. The d/d model-based Wiener and CLS restoration filters, discussed next, alleviate this problem to some extent by balancing restoration sharpening against random noise enhancement.

### 2.3.2 Wiener Restoration Filter

The d/d model-based Wiener filter balances image sharpening against random noise enhancement by minimizing the expected value of the end-to-end MSD between the input scene and the output image. The d/d model-based Wiener filter's frequency response is given by

$$\hat{f}[\nu_1, \nu_2] = \frac{\hat{h}^*[\nu_1, \nu_2]}{|\hat{h}[\nu_1, \nu_2]|^2 + \hat{\Phi}_e[\nu_1, \nu_2]/\hat{\Phi}_s[\nu_1, \nu_2]} \quad (2.13)$$

---

<sup>7</sup>Due to high random noise enhancement, the images in figure (2.5[c]) and figure (2.5[d]) had to be normalized for display purposes. In each case, the histogram of the real-valued restored image was clipped at the low and high ends to discard 5 percent of the values. The remaining values were then linearly scaled to the range  $0 \dots 2^{12} - 1$ . The patterns in figure (2.5[d]) are caused by graylevel consolidation that takes place when the real-valued restored image is converted to a 8-bit image for display.

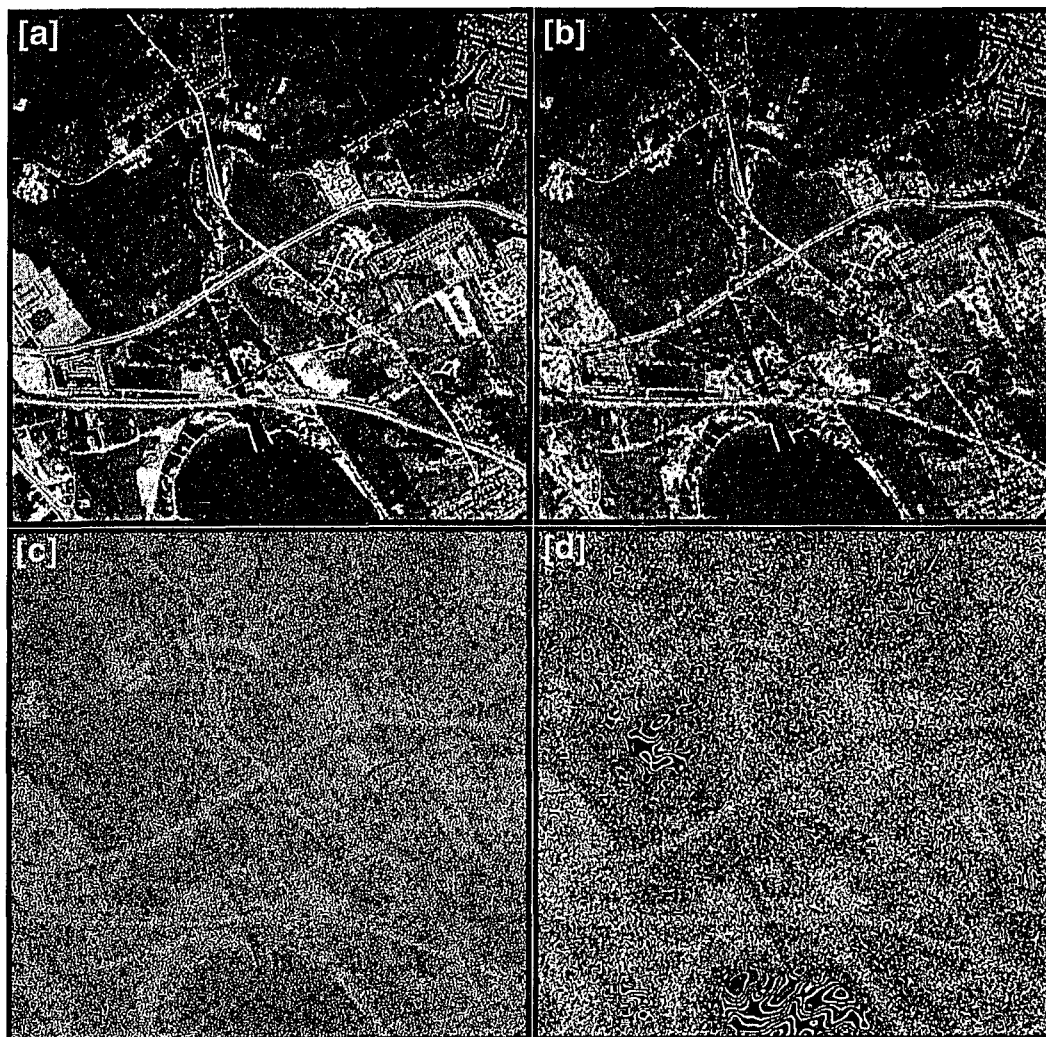


Figure 2.5: Inverse filter restorations with quantization noise.

where  $\hat{h}^*$  is the complex-conjugate of  $\hat{h}$ . The terms  $\hat{\Phi}_e[\nu_1, \nu_2] = E[|\hat{e}[\nu_1, \nu_2]|^2]$  and  $\hat{\Phi}_s[\nu_1, \nu_2] = E[|\hat{s}[\nu_1, \nu_2]|^2]$  are the ensemble-averaged energy of the random noise and the stochastic scene respectively.<sup>8</sup> The non-negative ratio  $\hat{\Phi}_e[\nu_1, \nu_2]/\hat{\Phi}_s[\nu_1, \nu_2]$  is a frequency-dependent reciprocal energy-based SNR. If it were possible to estimate this ratio with perfect accuracy, the resultant restoration filter would be optimal in the sense of minimizing the expected end-to-end MSD with respect to any other (linear) restoration filter.

The ratio  $\hat{\Phi}_e[\nu_1, \nu_2]/\hat{\Phi}_s[\nu_1, \nu_2]$  allows the Wiener filter to moderate its high-boost response in the presence of additive random noise. If this non-negative ratio is not 0 at  $[\nu_1, \nu_2]$ , then by inspection the Wiener filter response is smaller than the inverse filter response — at this frequency the Wiener filter does not sharpen as much as the inverse filter. Consequently, random noise enhancement by the Wiener filter is less pronounced relative to the inverse filter. Depending on the magnitude of the ratio, the Wiener filter may not sharpen significantly (or at all) since doing so would result in unacceptable levels of enhanced random noise. Indeed, in the extreme case where the image is so noisy that  $\hat{\Phi}_e[\nu_1, \nu_2]/\hat{\Phi}_s[\nu_1, \nu_2] \gg |\hat{h}[\nu_1, \nu_2]|$  at all high frequencies, instead of sharpening the Wiener restoration filter will further blur the digital image to suppress random noise.

Examples of d/d model-based Wiener restorations of the blurred and quantized

---

<sup>8</sup>Equation (2.13) is valid when  $\hat{\Phi}_s[\nu_1, \nu_2] \neq 0$ . Otherwise, by convention,  $\hat{f}[\nu_1, \nu_2] = 0$ . That is, if the scene does not have any energy at a particular frequency, the Wiener filter does not need to restore at that frequency.

aerial images are presented in figure (2.6). To generate the Wiener filter response for each of the three blurred images, the actual values of  $|\hat{s}[\nu_1, \nu_2]|^2$  and  $|\hat{e}[\nu_1, \nu_2]|^2$  are used in place of their respective energy spectra.<sup>9</sup> Doing so avoids the issue of how to *estimate* the ratio  $\hat{\Phi}_e[\nu_1, \nu_2]/\hat{\Phi}_s[\nu_1, \nu_2]$ ; this issue is discussed in chapter 4. The restored images in figure (2.6) are sharper than the corresponding unrestored images in figure (2.3) and, although some random noise enhancement is visible in the uniform areas, the level of enhanced random noise is dramatically reduced relative to the inverse filter restorations in figure (2.5).

With no quantization noise the Wiener filter reduces to the inverse filter. The Wiener restorations in this case are indistinguishable from the corresponding inverse filter restorations in figure (2.4).

### 2.3.3 CLS Restoration Filter

The CLS restoration filter attempts to achieve a compromise between image sharpening and random noise enhancement by maximizing the smoothness of the restored image subject to a constraint on how well (in a MSD sense) the restored image agrees with the digital image. The d/d model-based CLS restoration filter's frequency response is given by

$$\hat{f}[\nu_1, \nu_2] = \frac{\hat{h}^*[\nu_1, \nu_2]}{|\hat{h}[\nu_1, \nu_2]|^2 + \alpha |\hat{e}[\nu_1, \nu_2]|^2} \quad (2.14)$$

---

<sup>9</sup>The array  $|\hat{e}[\nu_1, \nu_2]|^2$  is generated by directly computing the quantization noise from the real-valued and integer-valued representations of the blurred image.



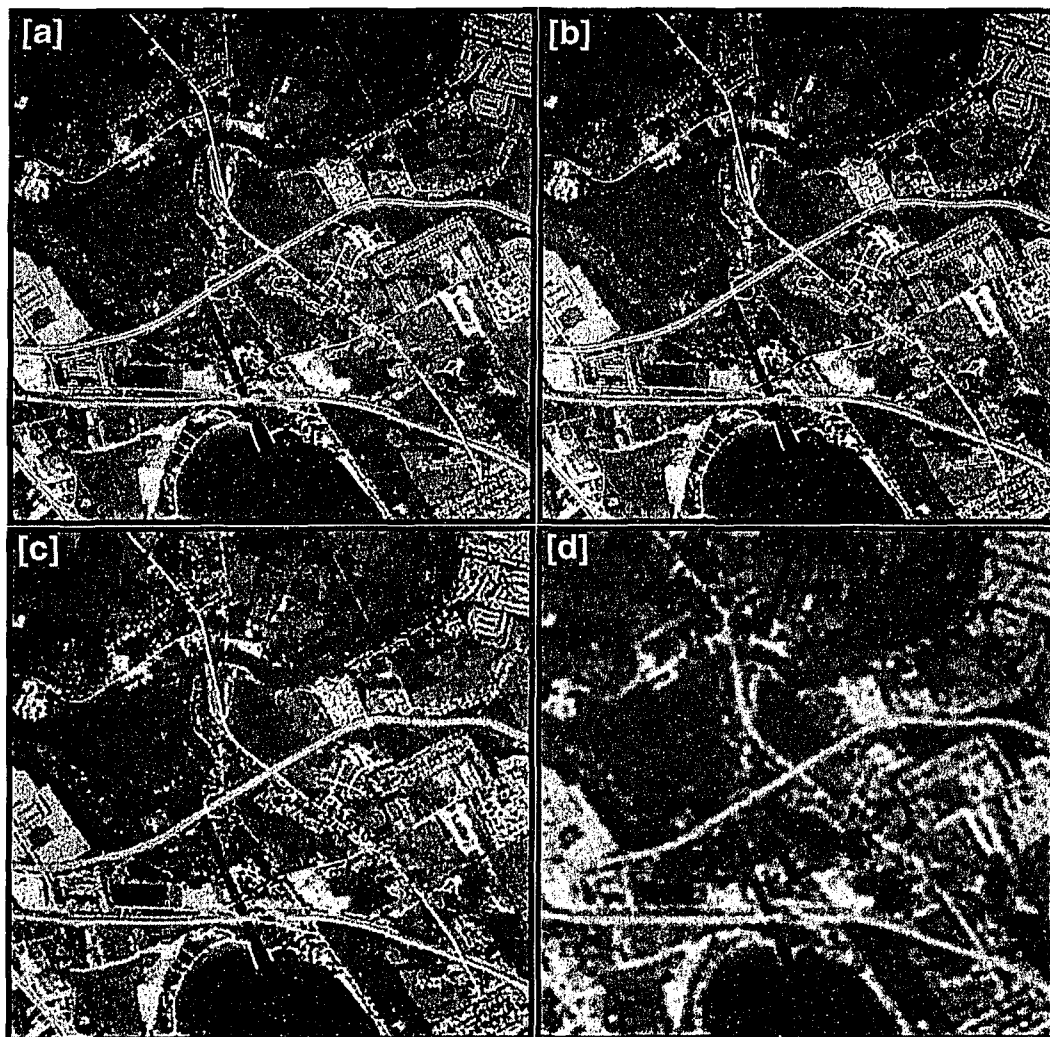


Figure 2.6: Wiener filter restorations with quantization noise.

where  $\hat{c}[\nu_1, \nu_1]$  is a user-specified high-pass filter array, periodic with period  $N_1 \times N_2$ , and  $\alpha$  is a non-negative parameter. In the regularization literature,  $\hat{c}$  (or  $c$ ) is called the *stabilizing functional* [56] and  $\alpha$  is known as the *smoothing parameter* [2]. A common choice for the stabilizing functional is the high-pass filter array

$$\hat{c}[\nu_1, \nu_2] = 2 \left( 1 - \cos(2\pi\omega) \right). \quad (2.15)$$

The radial frequency is  $\omega = \sqrt{(\nu'_1/N_1)^2 + (\nu'_2/N_2)^2}$  where  $\nu'_1 = |\nu_1| \bmod N_1$  and  $\nu'_2 = |\nu_2| \bmod N_2$  make the  $\hat{c}$  array periodic with period  $N_1 \times N_2$ . Although other choices of  $\hat{c}$  have been advocated (see [57]–[59]), because the high-pass filter in equation (2.15) has worked well in a variety of applications, it is used in the simulations to follow. The smoothing parameter  $\alpha$  is determined directly from the digital image and a knowledge of the statistics of the noise [43].

At low frequencies where random noise is usually insignificant compared to the scene,  $\alpha|\hat{c}[\nu_1, \nu_2]|^2$  is small relative to  $|\hat{h}[\nu_1, \nu_2]|^2$ ; this allows the CLS restoration filter to boost low frequencies. At high frequencies where random noise is generally most significant,  $\alpha|\hat{c}[\nu_1, \nu_2]|^2$  is largest relative to  $|\hat{h}[\nu_1, \nu_2]|^2$ ; this prevents the CLS restoration filter from boosting high frequencies, thereby reducing random noise enhancement. In the special case where there is no additive random noise,  $\alpha = 0$  and the CLS restoration filter reduces to the inverse filter; the restored images in figure (2.4) are the result.

Examples of d/d model-based CLS restorations of the blurred and quantized aerial images are presented in figure (2.7). The value of  $\alpha$  for the  $\sigma_1 = \sigma_2 = 0.04$

case is  $9.765 \times 10^{-4}$ . For the other two cases,  $\sigma_1 = \sigma_2 = 0.1$  and  $\sigma_1 = \sigma_2 = 0.25$ , the  $\alpha$  values are  $2.440 \times 10^{-4}$  and  $1.400 \times 10^{-4}$ , respectively. This pattern is consistent with the intuitive need to diminish the degree of regularization with decreasing OTF blur; 1-D profiles of the CLS restoration filter's frequency response are illustrated in figure (2.8).<sup>10</sup> The moderation of the high-boost response of the CLS restoration filter to avoid additive noise enhancement is clearly seen in this figure. At low frequencies, the CLS filter's frequency response is virtually identical to that of the inverse filter. With increasing frequency, however, random noise energy becomes significant and the CLS restoration filter's response drops relative to that of the inverse filter.

In the presence of random (quantization) noise, the CLS restorations in figure (2.7) are clearly superior to the restorations in figure (2.5) obtained by using the inverse filter; this illustrates the effectiveness of the CLS restoration approach. Consistent with the results of previous d/d model-based comparisons of the CLS and Wiener restoration filters (e.g., [61]), the CLS restorations are seen to be similar in quality to those obtained by the Wiener filter.

By inspection, the d/d model-based CLS restoration filter reduces to the d/d model-based Wiener filter if and only if  $\alpha |\hat{c}[\nu_1, \nu_2]|^2 = \hat{\Phi}_e[\nu_1, \nu_2] / \hat{\Phi}_s[\nu_1, \nu_2]$ . If so, the CLS restoration filter produces the best-possible restoration in an expected MSD sense. This result is of theoretical interest only; in practice, the CLS filter is

---

<sup>10</sup>To illustrate all three frequency responses meaningfully on a common vertical scale, the frequency responses in figure (2.8) are expressed in *decibels*.

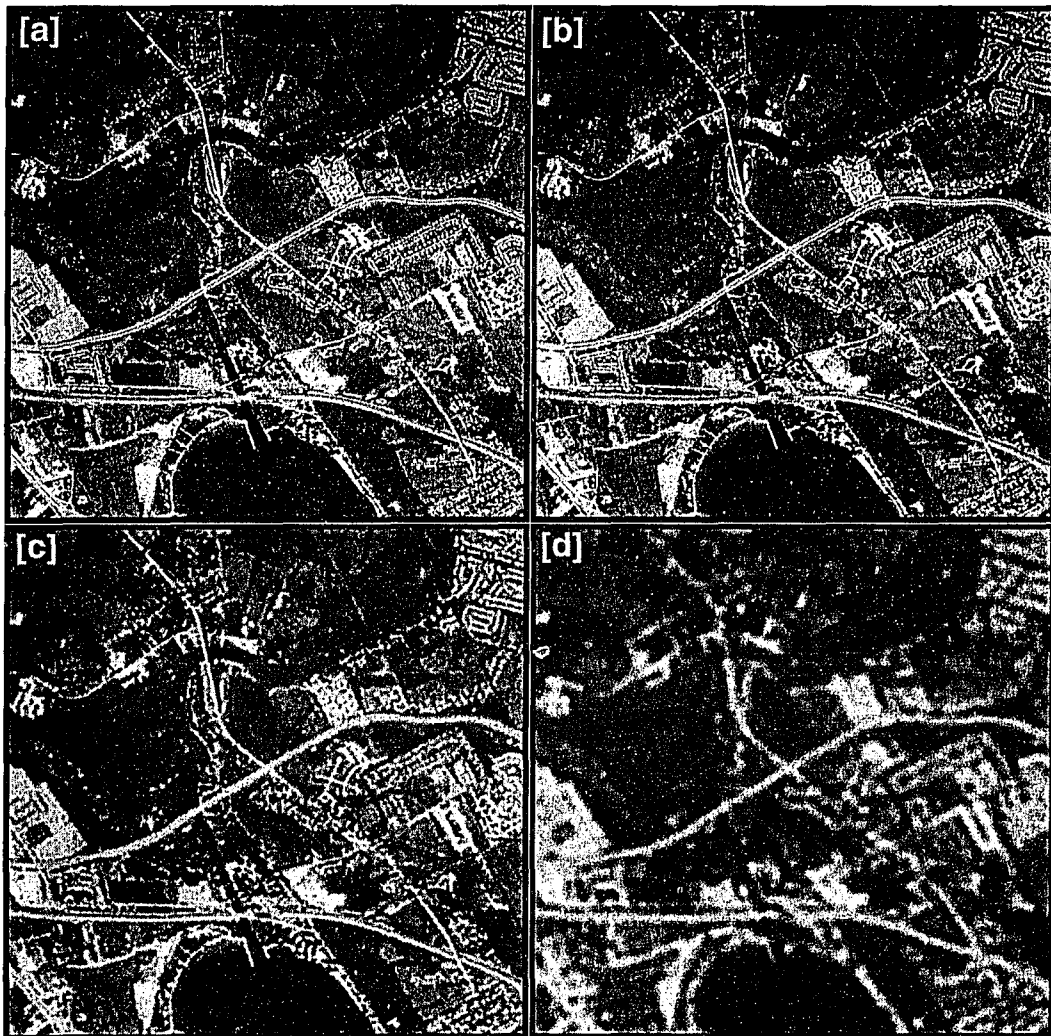


Figure 2.7: CLS filter restorations with quantization noise.

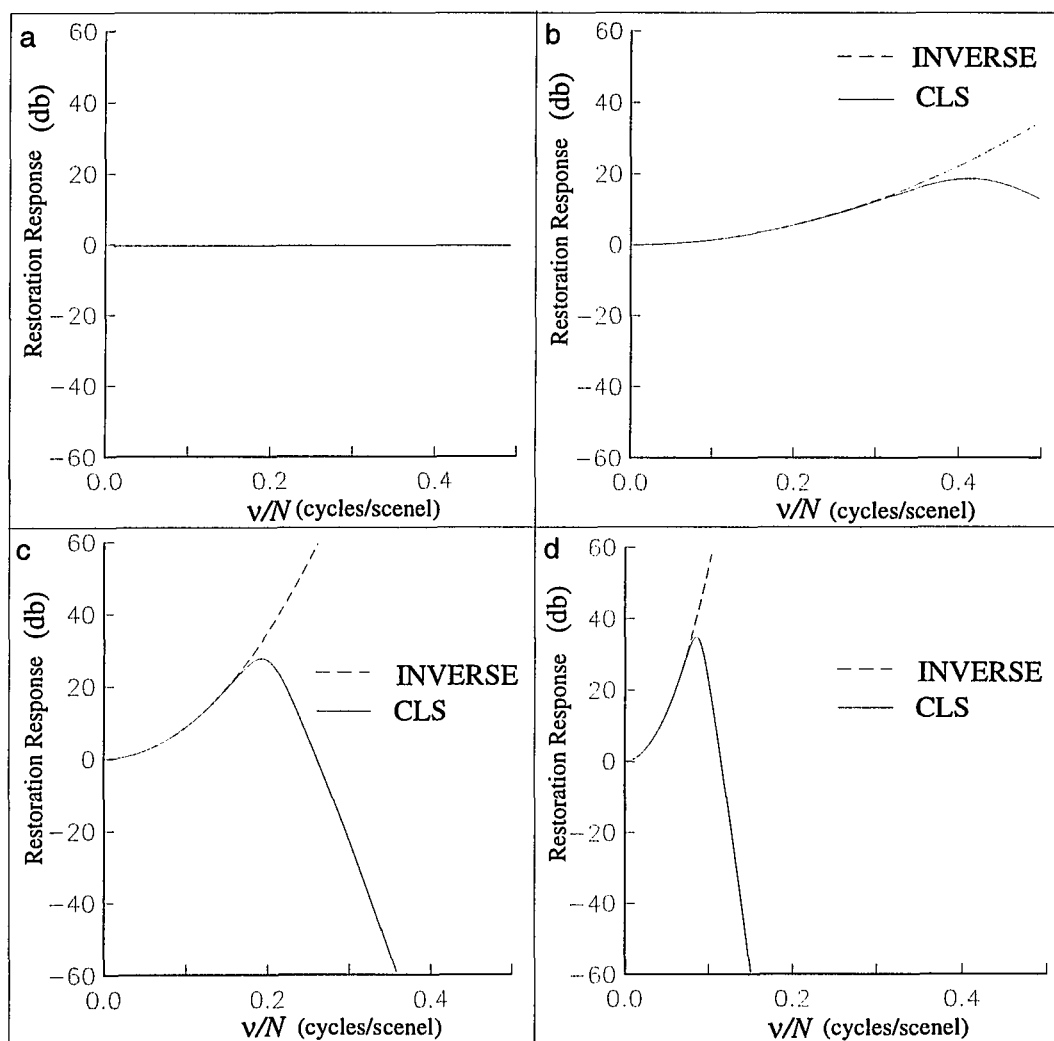


Figure 2.8: 1-D CLS filter frequency response.

never identical to the Wiener filter because the ratio  $\hat{\Phi}_e[\nu_1, \nu_2]/\hat{\Phi}_s[\nu_1, \nu_2]$  cannot be estimated perfectly.

The simulated restorations using the inverse filter, the Wiener filter and the CLS filter serve as good illustrations of an established perception among those practitioners of image restoration who base their work on a d/d system model. This perception is that additive random noise contributed by quantization and/or other sources effectively limits the extent to which optical blurring can be removed by the use of a digital restoration filter. As illustrated in figure (2.4), if random noise is negligible, d/d model-based restoration filters can successfully remove even a large degree of image acquisition blur. In such (ideal) cases, the restoration filter of choice is essentially the inverse filter. When random noise is not negligible, however, the image sharpening effect of the restoration filter has to be balanced against random noise enhancement. As illustrated in figure (2.8), the prescription in such cases is to modify the inverse filter so that the restoration filter's high-boost action is inhibited at (high) frequencies where random noise is significant. The Wiener restoration filter and the CLS restoration filter are good examples of such a prescription.

## 2.4 D/D Model Limitations

As discussed in chapter 1, a digital imaging system uses a continuous-to-discrete sampling process and a discrete-to-continuous reconstruction process. Both of these

processes are ignored by a  $d/d$  model. In this section, simulation is used to investigate the consequences of ignoring these two processes. Theoretical insight into these simulation results is presented in chapter 3.

Figure (2.9) illustrates the image degradation produced if the three  $512 \times 512$  blurred, unrestored images in figure (2.3) are sampled onto a  $128 \times 128$  grid, then enlarged (reconstructed) to  $512 \times 512$  by pixel replication.<sup>11</sup> When compared to the corresponding three images in figure (2.3), the images in figure (2.9) exhibit a phenomenon commonly known as “blockiness”; the blockiness is most apparent in figure (2.9[b]). The important point is that the three corresponding processed images in figures (2.9) and (2.3) are pairwise very similar but *not* identical because sampling and reconstruction produces image degradation.

To illustrate the consequences of ignoring sampling and reconstruction, the three processed images in figure (2.9) were filtered using the *same*  $d/d$  model-based inverse filters as those used to generate the corresponding restorations in figure (2.4). The (false) justification for using the inverse filter in this case is that the images in figure (2.9) are not quantized and so there is no additive random noise. In the absence of random noise, the inverse filter is identical to the  $d/d$  model-based Wiener and CLS restoration filters and therefore should produce the “best” restorations of the aerial scene. The results are illustrated in figure (2.10). When the three processed images in figure (2.10) are compared with the near-perfect restorations

---

<sup>11</sup>Figures (2.3[a]) and (2.9[a]) are the same.

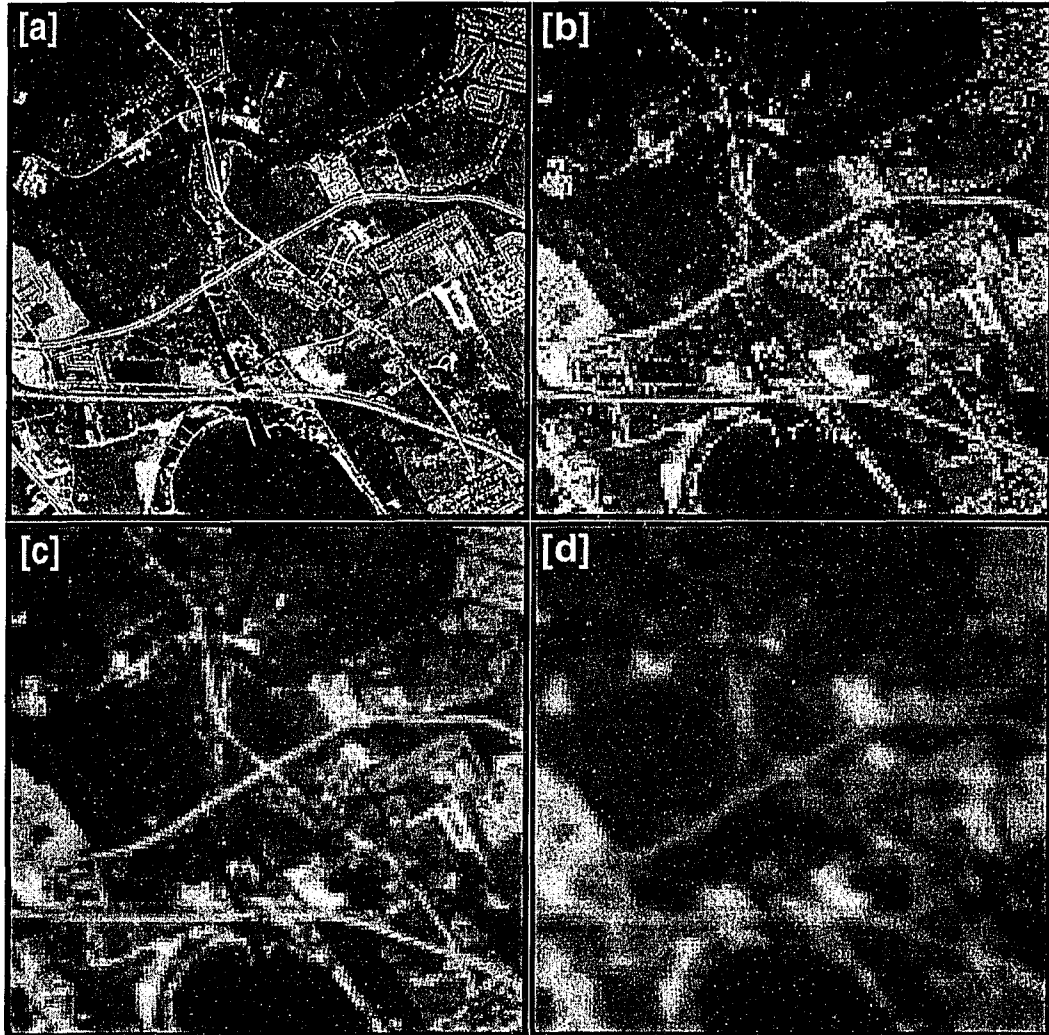


Figure 2.9: Blurred, sampled and pixel-replicated images.



in figure (2.4), it is clear that in this case the d/d model-based inverse filter fails to restore accurately, even though additive random noise is absent.

The artifacts in the figure (2.10) processed images are caused by the combined effect of sampling and reconstruction. In this case the reconstruction process, pixel replication, is naive. To demonstrate that the artifacts visible in figures (2.9) and (2.10) are not due to this naive reconstruction technique alone, figure (2.11) is presented. To produce this figure the  $128 \times 128$  to  $512 \times 512$  reconstruction was implemented via sinc function interpolation instead of pixel replication.<sup>12</sup> The sinc function was used for reconstruction because it is widely (but sometimes erroneously) accepted as the “ideal” reconstruction filter. That is, if a band-limited function is sampled sufficiently then the function can be reconstructed exactly by sinc function interpolation [60].

As in the case of reconstruction by pixel-replication, see figure (2.9), the sinc-reconstructed images in figure (2.11) exhibit sampling and reconstruction artifacts; the artifacts are less severe, however. Figure (2.12) illustrates the inverse filter restorations of the three processed images in figure (2.11). The restored images in figure (2.12) are a significant improvement over the corresponding restored images in figure (2.10). This improvement is attributed to the increased sophistication of sinc reconstruction relative to reconstruction by pixel-replication. Compared to figure (2.4), however, the artifacts in the restored images in figure (2.12) are

---

<sup>12</sup>A mathematical definition of the sinc function and its frequency response are presented in chapter 3.

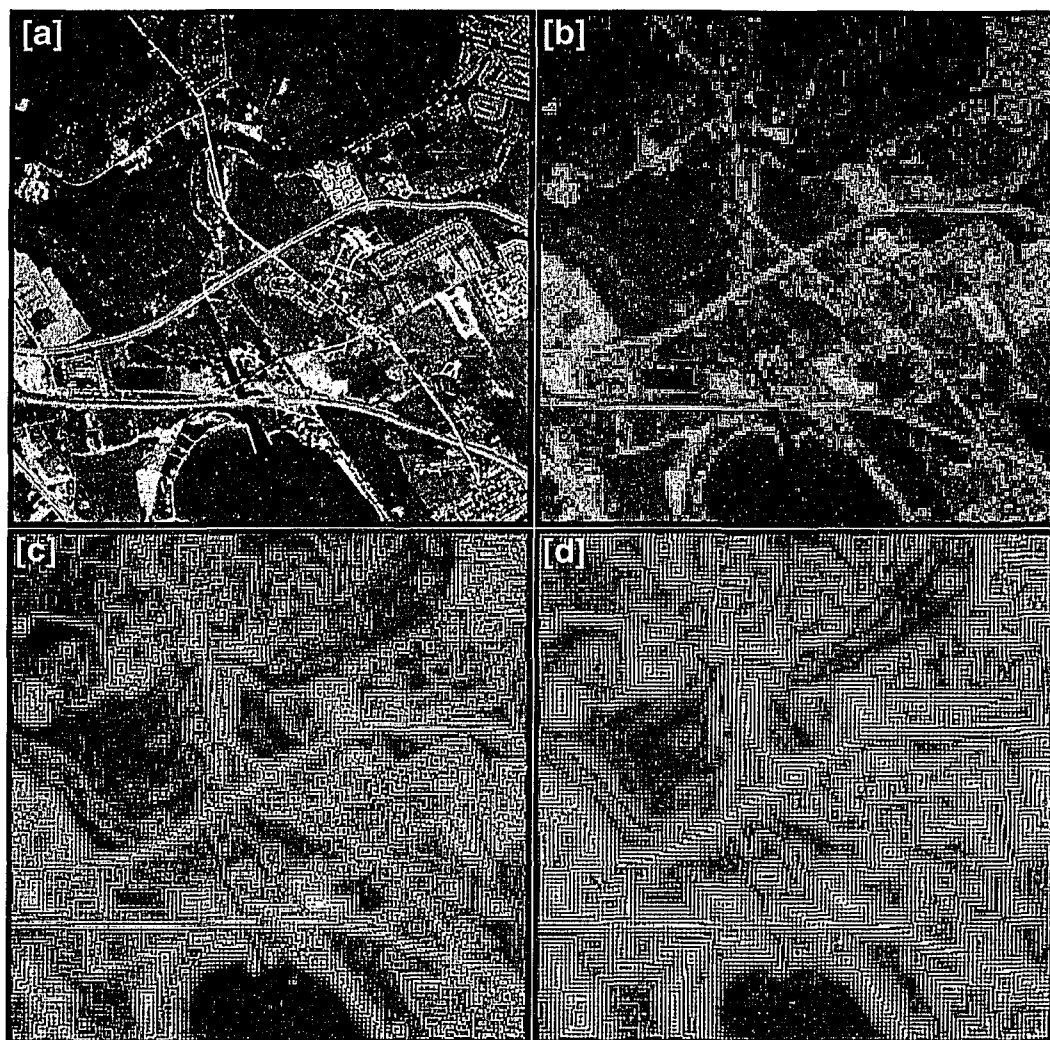


Figure 2.10: Inverse filter restoration of pixel-replicated images.

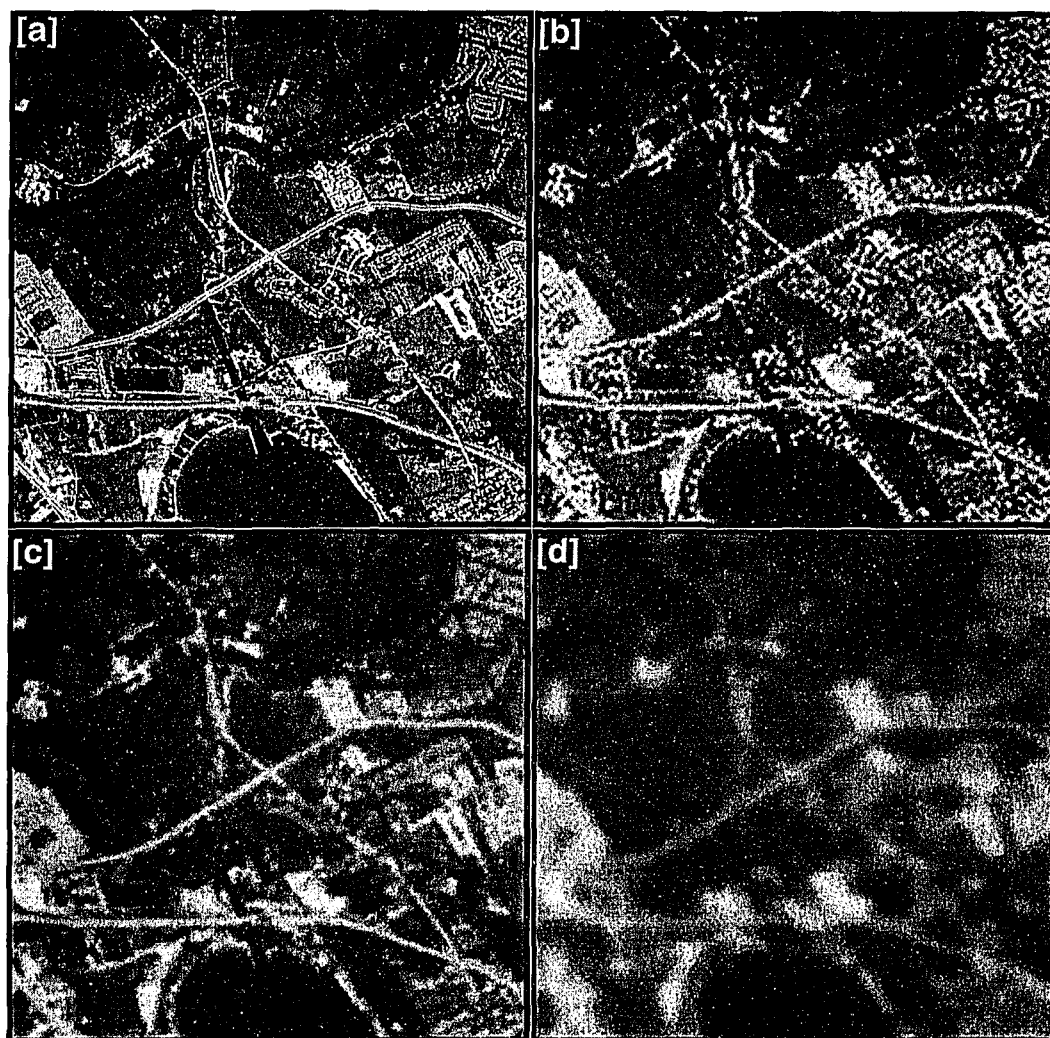


Figure 2.11: Blurred, sampled and sinc-interpolated images.

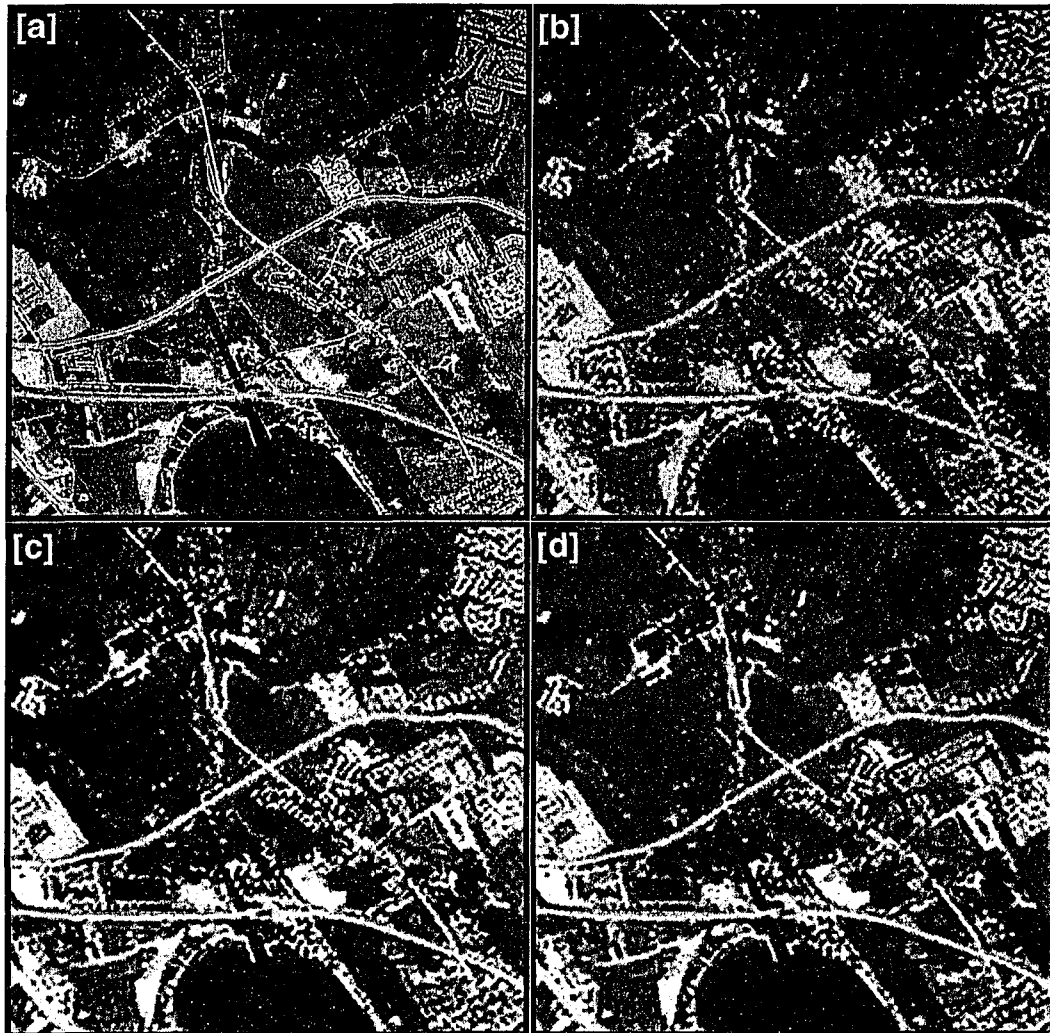


Figure 2.12: Inverse filter restoration of sinc-interpolated images.

nevertheless significant, particularly in figure (2.12[b]). This demonstrates that sampling and reconstruction cause a potentially significant image degradation that can only be partially suppressed by using a sophisticated reconstruction technique.

Sampling and reconstruction degrade a digital image in ways fundamentally different from both image acquisition blur and additive random noise. As illustrated in figures (2.10) and (2.12), if sampling and reconstruction are ignored, as they are in a d/d model, restoration filters may enhance the artifacts created by these processes. The enhancement of these artifacts, independent of the additive random noise enhancement problem illustrated in figure (2.5), can render d/d model-based restorations unacceptable. This is contrary to the perception among those practitioners who use a d/d model exclusively as a basis for digital image restoration.

The results presented in section 2.4 demonstrate the need for a more comprehensive c/d/c system model as the basis for digital restoration filter design. Chapter 3 provides such a model. Subsequent chapters present two c/d/c model-based restoration filters and their applications.

# CHAPTER III

## SAMPLED IMAGING SYSTEMS AND DIGITAL IMAGE RESTORATION

A *continuous-input/discrete-processing/continuous-output* (c/d/c) imaging system model is presented in this chapter. Unlike a d/d model that ignores sampling and reconstruction, a c/d/c model describes the end-to-end digital imaging process more comprehensively, using both continuous and discrete model components as appropriate. By doing so, a c/d/c model provides an explanation for the failure of d/d model-based restoration filters to restore accurately in the presence of sampling and reconstruction. That is, in this chapter simulations based on the c/d/c model illustrate that sampling and reconstruction are a potential source of additive, *scene-dependent* noise. This noise interacts with the restoration process in a fundamental way that limits the extent to which a sampled image can be restored by digital filtering.

### 3.1 A C/D/C Imaging System Model

A c/d/c imaging system model is illustrated in figure (3.1). The input  $s$  is the projection of a continuous scene onto the image acquisition system. The input scene is blurred by the image acquisition PSF  $h$ , then sampled and quantized to

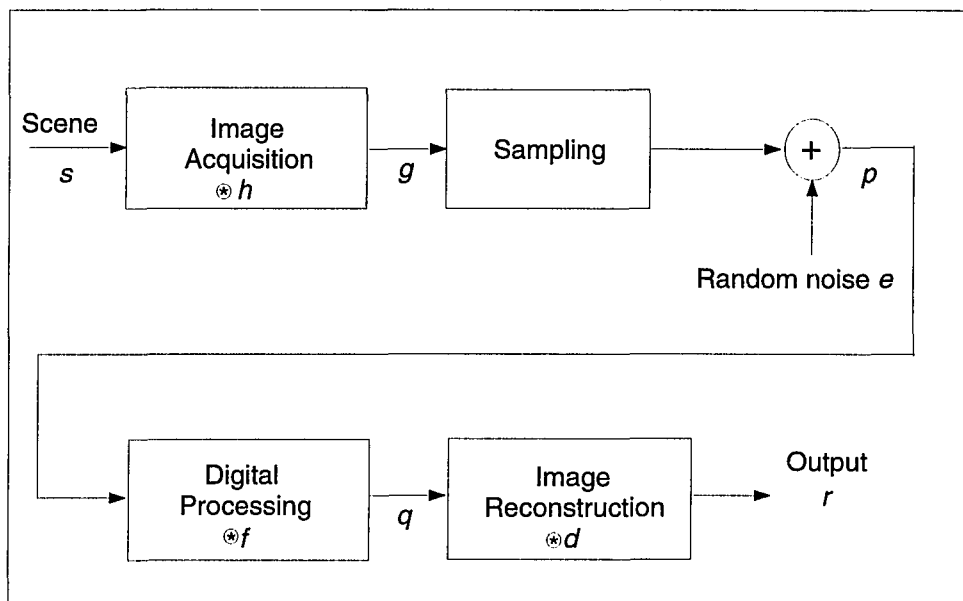


Figure 3.1: A continuous/discrete/continuous (c/d/c) imaging system model

produce a digital image  $p$ . The additive random noise  $e$  is a result of quantization and other sources. A digital restoration filter  $f$  is applied to the digital image to produce a processed digital image  $q$ . The processed digital image is filtered by the reconstruction PSF  $d$  to yield a continuous output image  $r$ .

### 3.1.1 Coordinate System

It is necessary to choose a *common* spatial coordinate system with respect to which all the c/d/c model components can be referenced. By doing so, a corresponding frequency coordinate system is chosen as well. Given the need for a common coordinate system, a decision must be made about whether to use coordinates fixed

relative to the *scene*, or fixed relative to the *image acquisition* system.<sup>1</sup> Although the choice is dictated by tradition and application-specific considerations, to facilitate frequency domain analysis it is desirable that the chosen coordinate system be one in which sampling is *uniform* in both (orthogonal) directions. Such a coordinate system is illustrated in figure (3.2).

The  $(x_1, x_2)$  coordinate system in figure (3.2) is natural for digital imaging systems that use a 2-D staring-array of photo-detectors;  $(x_1, x_2)$  represents a location on the array. Without loss of generality, distances in this coordinate system can be normalized to the inter-detector (inter-pixel) distances with the detector (pixel) centers at the integer grid points  $[n_1, n_2]$ , as indicated. Because of this convention, frequencies  $(\omega_1, \omega_2)$  are measured in cycles/pixel. The sampling frequency in both directions is 1.0 cycles/pixel; the Nyquist frequency is 0.5 cycles/pixel.

### 3.1.2 Image Formation

The continuous input scene  $s$  is *not* a scene as described by a 3-D scene-based coordinate system, but its 2-D optical *projection* onto the  $(x_1, x_2)$  coordinate system. The projection is assumed to be perfect, free of any non-linear geometric distortion.<sup>2</sup> Only the portion of the projected scene that is within the field-of-view (FOV) of

---

<sup>1</sup>A related decision must be made about whether to measure distances in angular or linear coordinates; except for chapter 8, linear coordinates are used throughout the dissertation.

<sup>2</sup>The projection need not be completely free of all image degradations; certain degradations such as atmospheric blurring can be accounted for in the system OTF.



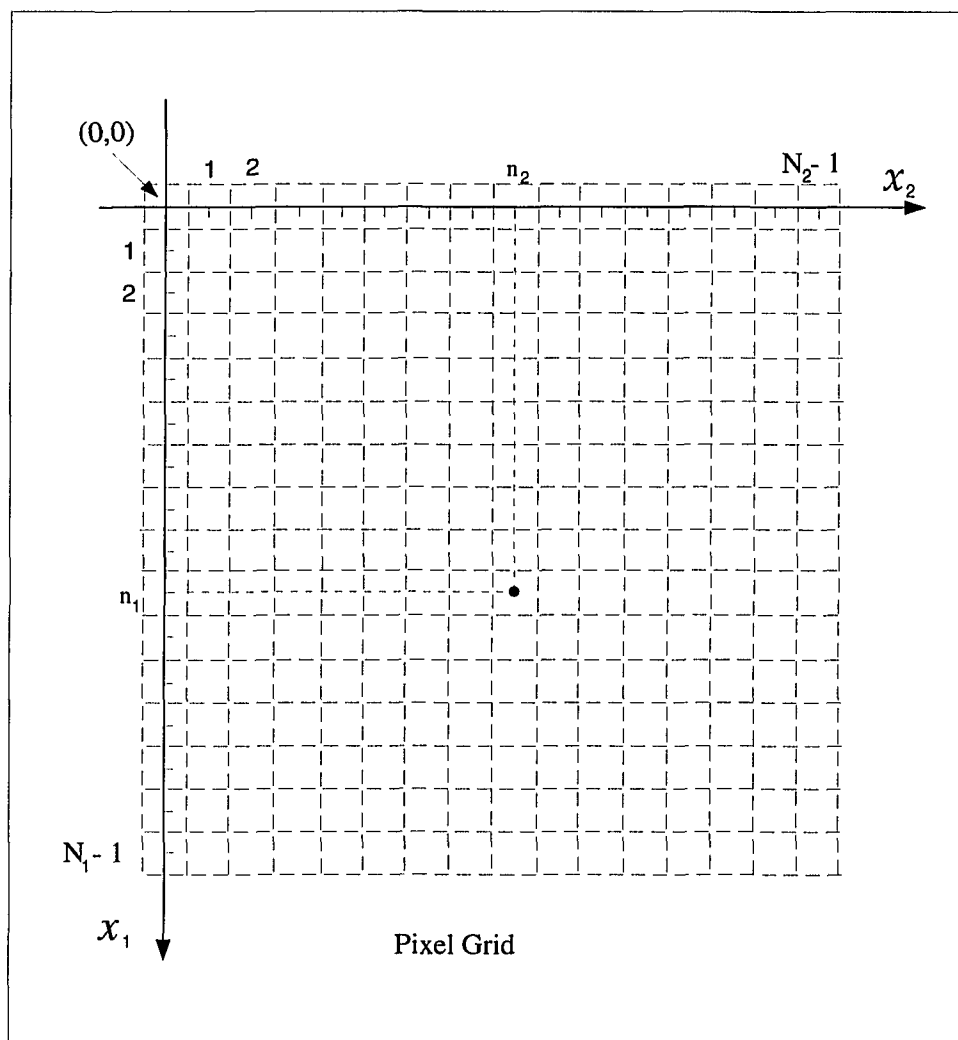


Figure 3.2: A c/d/c model coordinate system

the imaging system is of interest. Relative to the normalized  $(x_1, x_2)$  coordinate system in figure (3.2), the FOV is the region tessellated by the  $N_1 \times N_2$  pixel grid. Except perhaps at the natural edges of the scene defined by the FOV, there is no significant error caused by assuming that the input scene is periodic with period  $N_1 \times N_2$ . The periodicity of the input scene allows it to be represented as a Fourier series

$$s(x_1, x_2) = \sum_{|\nu_1| \leq \tau_1} \sum_{|\nu_2| \leq \tau_2} \hat{S}[\nu_1, \nu_2] \exp(i2\pi x_1 \nu_1 / N_1) \exp(i2\pi x_2 \nu_2 / N_2) \quad (3.1)$$

where  $\nu_1, \nu_2$  are integer-valued frequency indices. The corresponding Fourier series coefficients are

$$\hat{S}[\nu_1, \nu_2] = \frac{1}{N_1 N_2} \int_0^{N_1} \int_0^{N_2} s(x_1, x_2) \exp(-i2\pi x_1 \nu_1 / N_1) \exp(-i2\pi x_2 \nu_2 / N_2) dx_1 dx_2 \quad (3.2)$$

The scene is assumed to be *band-limited* — only  $(2\tau_1 + 1)(2\tau_2 + 1)$  Fourier coefficients are assumed to be non-zero. Although real scenes are not truly band-limited, using equation (3.1) does not necessarily adversely affect the accuracy of a c/d/c model. By choosing the scene's cut-off frequencies  $\tau_1/N_1, \tau_2/N_2$  to be much greater than the Nyquist frequency, one can model sub-pixel-scale detail in the scene; see section 3.2 for more discussion of this point.

Image acquisition is modeled as a convolution of the periodic input scene with an aperiodic function  $h$ . This PSF quantifies all the low-pass filtering effects of image acquisition prior to sampling. The pre-sampled image  $g = s \oplus h$  is the function

defined by convolution as

$$g(x_1, x_2) = \int_{-\infty}^{\infty} \int_{-\infty}^{\infty} h(x'_1, x'_2) s(x_1 - x'_1, x_2 - x'_2) dx'_1 dx'_2 \quad (3.3)$$

Due to the periodicity of  $s$ , the pre-sampled image is also periodic with period  $N_1 \times N_2$ . The corresponding Fourier series coefficients are defined by the convolution theorem as

$$\hat{G}[\nu_1, \nu_2] = \hat{H}(\nu_1/N_1, \nu_2/N_2) \hat{S}[\nu_1, \nu_2] \quad (3.4)$$

where the continuous Fourier transform of  $h$  is the OTF

$$\hat{H}(\omega_1, \omega_2) = \int_{-\infty}^{\infty} \int_{-\infty}^{\infty} h(x_1, x_2) \exp(-i2\pi x_1 \omega_1) \exp(-i2\pi x_2 \omega_2) dx_1 dx_2. \quad (3.5)$$

Although real imaging systems may not be truly linear or shift-invariant, equation (3.3) is widely used to model image acquisition systems. The primary reason for this is that, within limits, linearity and shift-invariance are usually true to a good approximation. Moreover, as observed by Park et al. [62], "... without these assumptions, a mathematical analysis [of a c/d/c model] is virtually impossible". Chapter 8 presents an application where the shift-invariance assumption is false and describes one possible method for using a c/d/c model in this case.

### 3.1.3 Image Sampling and Additive Random Noise

Consistent with the coordinate system in figure (3.2), the pre-sampled image function  $g$  is sampled and quantized to yield the digital image array  $p$ . That is,

$$p[n_1, n_2] = g(n_1, n_2) + e[n_1, n_2] \quad (3.6)$$

where  $e$  denotes additive random noise associated with the image acquisition system (e.g., shot noise, circuit noise and quantization).<sup>3</sup> The additive noise array is assumed to be periodic with period  $N_1 \times N_2$ . Consistent with the periodicity of  $g$  and  $e$ , the digital image  $p$  is periodic with period  $N_1 \times N_2$ . The corresponding DFT array is defined by the sampling theorem as

$$\hat{p}[\nu_1, \nu_2] = \hat{S}[\nu_1, \nu_2] \hat{H}(\nu_1/N_1, \nu_2/N_2) + \hat{e}[\nu_1, \nu_2] + \hat{a}[\nu_1, \nu_2] \quad (3.7)$$

where  $\hat{e}[\nu_1, \nu_2]$  is the DFT array associated with  $e$ . Equation (3.7) is similar to the corresponding d/d model equation, equation (2.6), except for the important additional term

$$\hat{a}[\nu_1, \nu_2] = \sum_{[k_1, k_2] \neq [0, 0]} \hat{S}[\nu_1 - k_1 N_1, \nu_2 - k_2 N_2] \hat{H}(\nu_1/N_1 - k_1, \nu_2/N_2 - k_2). \quad (3.8)$$

This term quantifies the energy in  $g = s \oplus h$  outside the *sampling passband*

$$\{(\omega_1, \omega_2) : -0.5 \leq \omega_1 \leq 0.5, -0.5 \leq \omega_2 \leq 0.5\} \quad (3.9)$$

that folds (*pre-aliases*) into frequencies within the sampling passband. If  $\hat{G}[\nu_1, \nu_2]$  is zero for all  $(\nu_1/N_1, \nu_2/N_2)$  outside the sampling passband then  $\hat{a}[\nu_1, \nu_2] = 0$  for all  $(\nu_1/N_1, \nu_2/N_2)$  within the sampling passband. In this case, there is no pre-aliasing.

In most imaging applications, however,  $g$  is *not* sufficiently sampled. That is, natural scenes typically contain significant sub-pixel-scale detail (energy at frequencies

---

<sup>3</sup>For notational clarity, continuous model components are expressed using a conventional function notation, e.g.,  $s(x_1, x_2)$ , while discrete model components are expressed using an array notation, e.g.,  $p[n_1, n_2]$ .

outside the sampling passband) that are not rejected by the OTF. Therefore, some pre-aliasing is inevitable [10].

### 3.1.4 Digital Processing

Digital processing (restoration filtering) is accomplished by convolving  $p$  with a restoration filter  $f$ . The restoration filter array is assumed to be periodic with period  $N_1 \times N_2$ ; this periodicity facilitates the frequency-domain design of the restoration filter. The filtered image array  $q = p \oplus f$  defined by

$$q[n_1, n_2] = \frac{1}{N_1 N_2} \sum_{n'_1=0}^{N_1-1} \sum_{n'_2=0}^{N_2-1} p[n'_1, n'_2] f[n_1 - n'_1, n_2 - n'_2] \quad (3.10)$$

is periodic with period  $N_1 \times N_2$ . The corresponding DFT array is

$$\hat{q}[\nu_1, \nu_2] = \hat{p}[\nu_1, \nu_2] \hat{f}[\nu_1, \nu_2] \quad (3.11)$$

where  $\hat{f}[\nu_1, \nu_2]$  is the restoration filter DFT array.

### 3.1.5 Image Reconstruction

The final step of a c/d/c model accounts for the discrete-to-continuous transformation required to convert the filtered image array to a continuous (analog) format. The most common instance of a reconstruction process is a display device (e.g., CRT monitor, photographic film) that converts the digital data into continuous form for viewing. Reconstruction for the purpose of display is not, however, the only image reconstruction application. Digital imaging applications involving *non-visual* data (e.g., remote sensing) generally reconstruct the digital image prior to *resampling* for

the purpose of enlargement or registration. Any resampling operation can be modeled as a discrete-to-continuous reconstruction (interpolation) process followed by a (re)sampling process. Therefore, reconstruction is implicit in image enlargement or image registration. Reconstruction, either for the purpose of display or resampling, has the potential for significantly degrading the quality of a digital image [10].

Image reconstruction is modeled as a convolution of the filtered image array  $q$  with an aperiodic reconstruction PSF  $d$ . The reconstructed image function  $r = q \oplus d$  is periodic with period  $N_1 \times N_2$ ; from equations (3.7) and (3.11) its Fourier series coefficients are

$$\hat{R}[\nu_1, \nu_2] = (\hat{S}[\nu_1, \nu_2] \hat{H}(\nu_1/N_1, \nu_2/N_2) + \hat{e}[\nu_1, \nu_2] + \hat{a}[\nu_1, \nu_2]) \hat{f}[\nu_1, \nu_2] \hat{D}(\nu_1/N_1, \nu_2/N_2) \quad (3.12)$$

where the function

$$\hat{D}(\omega_1, \omega_2) = \int_{-\infty}^{\infty} \int_{-\infty}^{\infty} d(x_1, x_2) \exp(-i2\pi x_1 \omega_1) \exp(-i2\pi x_2 \omega_2) dx_1 dx_2 \quad (3.13)$$

is the Fourier transform of the reconstruction PSF. In this dissertation  $\hat{D}(\omega_1, \omega_2)$  is called the reconstruction transfer function (RTF); the RTF characterizes both display PSFs and reconstruction PSFs.

Recall that equation (2.7) characterizes a d/d imaging system model in the frequency domain. Similarly, equation (3.12) provides a complete c/d/c model end-to-end frequency domain characterization. Equation (3.12) is more comprehensive than equation (2.7) because of the presence of the additive aliased term  $\hat{a}[\nu_1, \nu_2]$  and the multiplicative RTF  $\hat{D}(\nu_1/N_1, \nu_2/N_2)$ . In this way, equation (3.12) demonstrates

that image acquisition blur and random noise are not the only sources of degradation in a digital imaging system.

The periodic reconstructed image can be synthesized from its Fourier series coefficients as

$$r(x_1, x_2) = \sum_{\nu_1=-\infty}^{\infty} \sum_{\nu_2=-\infty}^{\infty} \hat{R}[\nu_1, \nu_2] \exp(i2\pi x_1 \nu_1 / N_1) \exp(i2\pi x_2 \nu_2 / N_2). \quad (3.14)$$

In general, although the input scene is band-limited, the reconstructed image may not be band-limited — hence the infinite summation in equation (3.14).<sup>4</sup> The energy in the reconstructed image outside the sampling passband is *spurious*; this spurious energy has been called *post-aliasing* [74].

### 3.2 C/D/C Model-Based Simulation

Simulation is an important computational tool for analyzing the performance of c/d/c model-based restoration filters. In this section, a frequency domain methodology for c/d/c model-based simulation is presented. This simulation methodology is used in this and subsequent chapters to investigate c/d/c model-based restoration filters. The discrete parts of a c/d/c model-based simulation, digital filtering and additive random noise generation, are similar to the corresponding parts of a d/d model-based simulation as discussed in section 2.2. The representation of the scene and the simulation of image acquisition are fundamentally different, how-

---

<sup>4</sup>Because most RTFs are effectively band-limited, for the purpose of simulation the infinite summation can be replaced, with negligible error, by an appropriate finite summation.

ever, as is the simulation of image reconstruction. Therefore, in this section scene representation, image acquisition and image reconstruction are discussed in some detail.

### 3.2.1 Scene Representation

In a c/d/c model-based simulation the scene can be represented in the frequency domain by defining the  $(2\tau_1 + 1)(2\tau_2 + 1)$  Fourier series coefficients  $\hat{S}[\nu_1, \nu_2]$ . Because primary consideration is given to modeling their frequency characteristics rather than their (spatial domain) appearance, scenes modeled in this manner are called *Fourier scenes* [64]. One such Fourier scene model, proposed by Modestino et al. [63], is used in chapter 4. Other Fourier scene models have been proposed for a variety of imaging applications [66]–[72].

Although they provide an excellent mechanism for generating *controlled* input scenes, Fourier scenes generally do not resemble real scenes. Consequently, the results of a c/d/c model-based simulation based on input Fourier scenes may not be visually convincing. As an alternative, high-resolution digital images of actual scenes, such as the *aerial* image used in chapter 2, can be used to simulate *band-limited, continuous* scenes and thereby provide the visual realism lacking in Fourier scenes. When a digital image is used as the input to a c/d/c model-based simulation, its corresponding DFT array can be used to construct the Fourier series coefficients such that the corresponding continuous scene interpolates the digital image *exactly*. The algorithm and associated mathematics for doing this are presented



in Appendix A. This algorithm is used for all the c/d/c model-based simulations in this dissertation.

### 3.2.2 Image Acquisition

The image acquisition PSF/OTF quantifies *all* deterministic (linear, shift-invariant) effects prior to sampling. For a staring-array digital imaging system, the components that contribute to the composite image acquisition OTF are the optics of the imaging system, the signal-conditioning detector circuits (or read-out circuits), jitter (if any), and the detectors themselves. Scanning systems contribute an additional component to the PSF corresponding to the scanning mechanism. As an alternative, digital techniques are now available for directly measuring the composite OTF of actual systems to well beyond the Nyquist frequency, thereby reducing the need for accurate OTF component modeling [73].

In the simulations presented later in this chapter, the parametric OTF model suggested by Johnson [75] is used. This model is

$$\hat{H}(\omega_1, \omega_2) = \exp \left( - \left( \sqrt{\omega_1^2 + \omega_2^2} / \sigma \right)^\beta \right) \quad (3.15)$$

where  $\sigma$  is the OTF scale parameter and  $\beta$  is the OTF shape parameter. If  $\beta = 2$ , the OTF is a 2-D circularly symmetric separable Gaussian; in this case, the OTF is the continuous, aperiodic version of the periodic, discrete Gaussian OTF model used in chapter 2. Johnson's model can be used to approximate the composite OTFs for a wide range of image acquisition devices when component modeling proves to be

difficult.

Figure (3.3) illustrates the OTF in equation (3.15) for  $\beta = 2.0$  and three different values of  $\sigma$ .<sup>5</sup> The OTF for the  $\sigma = 0.75$  cycles/pixel case, figure (3.3[b]), corresponds to an image acquisition system that produces little blurring but significant pre-aliasing. The OTFs for the  $\sigma = 0.50$  and  $\sigma = 0.25$  cases, figures (3.3[c]) and (3.3[d]), produce progressively more blurring, but less pre-aliasing. The dotted response in figure (3.3) represents an “ideal” low-pass filter that corresponds to the pre-sample filtering required to produce sufficient sampling with no blurring within the sampling passband.

### 3.2.3 Image Sampling

The pre-sampled image  $g = s \otimes h$  is sampled on a (rectangular)  $N_1 \times N_2$  grid. The real-valued result is quantized to yield the digital image  $p$ . Quantization produces random noise, the extent of which is quantified by the SNR parameter defined in chapter 2. If appropriate, additive random noise contributed by the electronic components of the image acquisition system can be simulated by adding random values to the quantized image to lower the SNR relative to its value associated with quantization noise only.

---

<sup>5</sup>Figure (3.3[a]) corresponds to  $\sigma = \infty$  which represents an image acquisition system that produces no blurring.

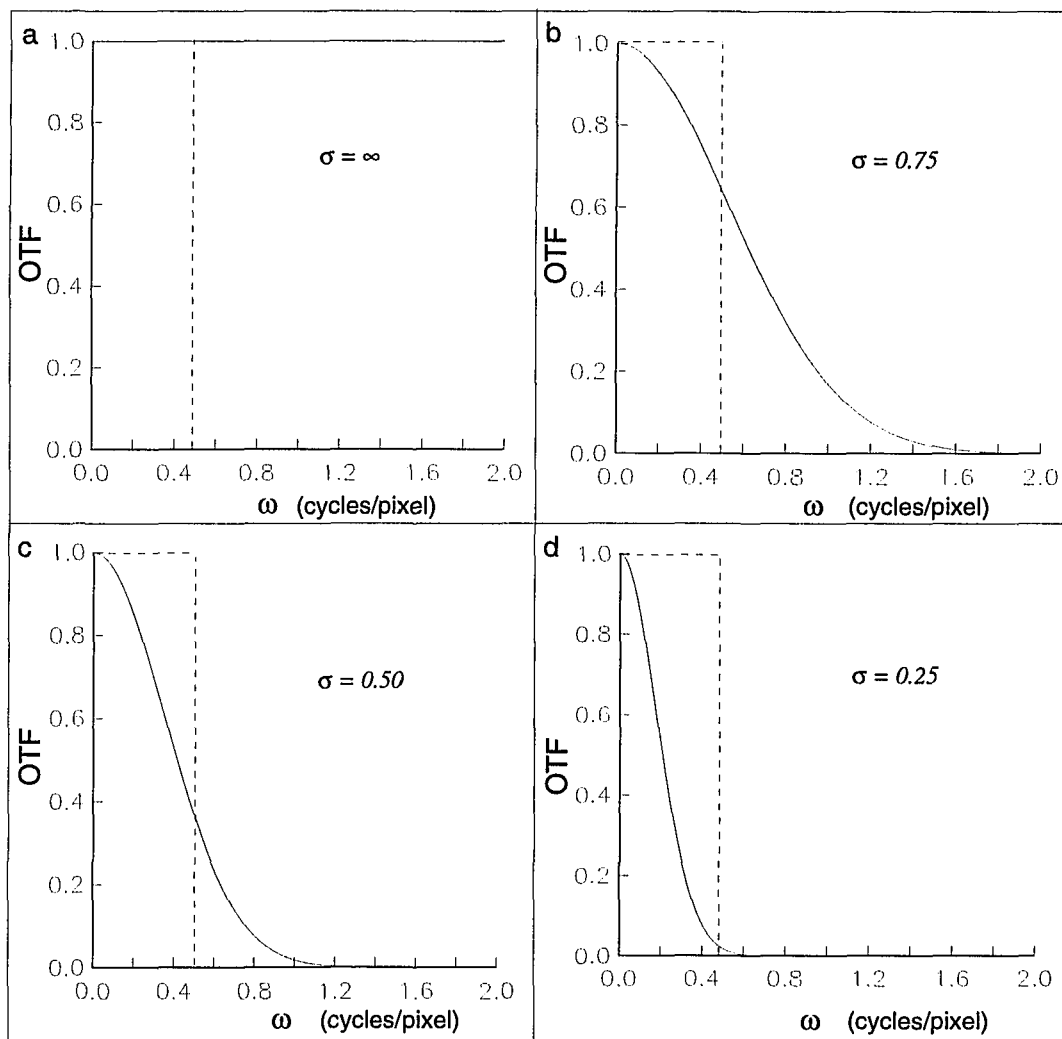


Figure 3.3: Image acquisition OTFs.

### 3.2.4 Digital Processing

Digital processing in a c/d/c model-based simulation is identical to that in a d/d model-based simulation. The  $N_1 \times N_2$  DFT array elements  $\hat{p}[\nu_1, \nu_2]$  are multiplied by the  $N_1 \times N_2$  filter response array elements  $\hat{f}[\nu_1, \nu_2]$  on a frequency-by-frequency basis to generate the  $N_1 \times N_2$  DFT array elements  $\hat{q}[\nu_1, \nu_2]$ .

### 3.2.5 Image Reconstruction

The processed digital image is reconstructed to a continuous image; the RTF characterizes this reconstruction. RTF models for display devices describe the low-pass filtering effects of display reconstruction. Schade's RTF model uses the sum of two Gaussians; one for the nucleus of the display spot and one for a flare about the nucleus due to the finite thickness of the phosphor and optical reflections of the faceplate surfaces in the cathode-ray tube [11]. Schade's two-component RTF model is

$$\hat{D}(\omega_1, \omega_2) = D_1 \exp\left(-(\omega_1^2 + \omega_2^2)/\alpha_1^2\right) + D_2 \exp\left(-(\omega_1^2 + \omega_2^2)/\alpha_2^2\right) \quad (3.16)$$

where  $D_1 = 0.8$ ,  $D_2 = 0.2$ ,  $\alpha_1 = 0.5$  cycles/pixel and  $\alpha_2 = 0.1$  cycles/pixel. Figure (3.4[a]) illustrates a 1-D RTF corresponding to this model. This model causes significant blurring and allows some post-aliasing. The RTF has negligible response beyond 1.0 cycles/pixel; this *effective* band-limit at twice the Nyquist frequency makes the summations in equation (3.14) finite.

Interpolative reconstruction is achieved by using reconstruction PSFs which sat-

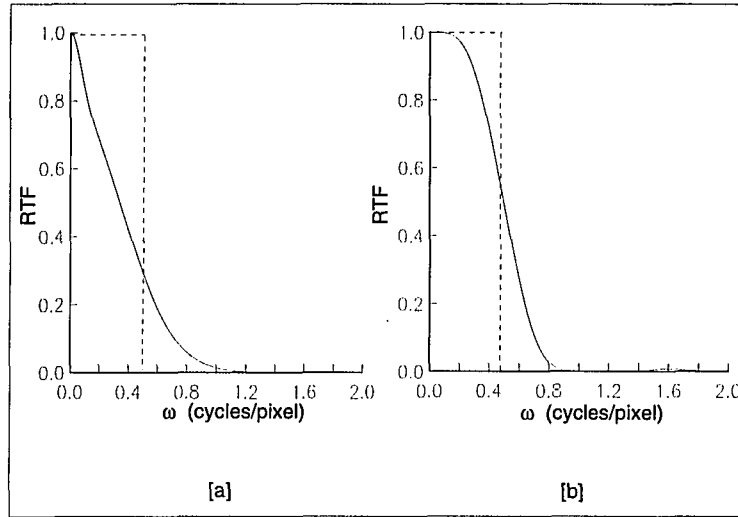


Figure 3.4: Image reconstruction RTFs: [a] Sum of two Gaussians, [b] PCC.

isfy the condition,

$$\sum_{n_1=-\infty}^{\infty} \sum_{n_2=-\infty}^{\infty} d(x_1 - n_1, x_2 - n_2) = 1 \quad (3.17)$$

for all  $(x_1, x_2)$ . This important property of interpolative reconstruction PSFs enables a uniformly gray scene to be reconstructed perfectly from a uniformly gray digital image; physical display devices are generally unable to do so [11]. There are a variety of interpolative image reconstruction PSFs [76]. One popular choice, the *Parametric Cubic Convolution* (PCC) reconstruction PSF, is a finite-support approximation to the sinc reconstruction function [77]. The corresponding default PCC RTF (with  $\alpha = -0.5$ ) is

$$\hat{D}(\omega_1, \omega_2) = \hat{D}_p(\omega_1) \hat{D}_p(\omega_2) \quad (3.18)$$

where for  $\omega \neq 0$

$$\hat{D}_p(\omega) = (\pi\omega)^{-2} \left( 2\text{sinc}^2(\omega) - \text{sinc}(2\omega) - 3\text{sinc}^2(2\omega) + \text{sinc}(4\omega) \right). \quad (3.19)$$

By convention,  $\hat{D}_p(0) = 1.0$ ; a 1-D version of this RTF is illustrated in figure (3.4[b]).

The PCC RTF causes some blurring and allows some post-aliasing. Like Schade's model, equation (3.16), the PCC response is effectively band-limited at twice the Nyquist frequency. In comparison to Schade's display RTF model, however, for a given digital image the PCC interpolator produces less blurring in the sampling passband but more post-aliasing. The dotted line in figure (3.16) represents the low-pass response of the sinc interpolator that was used in chapter 2.

### 3.2.6 C/D/C Model Simulation Examples

Figure (3.5) is a four-panel composite that uses the format introduced in chapter 2. That is, the three reconstructed images correspond to the finite-parameter-value OTFs presented in figure (3.3). As in chapter 2, figure (3.5[a]) is the input scene.

To produce figure (3.5) the three pre-sampled blurred images  $g = s \otimes h$  are sampled on a  $N_1 \times N_2 = 128 \times 128$  grid. Gaussian-distributed “white” noise (with a standard deviation of 0.86) is added to the sampled images; this results in an SNR of 50.<sup>6</sup> The digital images  $p$  are reconstructed (without restoration) using the PCC

---

<sup>6</sup>Truly Gaussian random noise is *not* integer-valued and therefore cannot be added to the sampled images in the spatial domain — doing so would make  $p$  real-valued. Therefore, to achieve the exact SNR of 50, the random noise is added in the frequency domain by adding the appropriate  $\hat{e}$  to  $\hat{p}$ .

RTF and displayed as  $512 \times 512$  images. Consistent with the OTF frequency characteristics in figure (3.3), the reconstructed images in figure (3.5) become increasingly more blurred as the OTF scale parameter  $\sigma$  is decreased. The reconstructed images in figure (3.5) also exhibit artifacts. The artifacts are most visible in figure 3.5[b]), which is the least blurred. Consistent with the results in section (2.4) and as demonstrated in the next section, the artifacts are caused by insufficient sampling and imperfect reconstruction.

Figure (3.6) is identical to figure (3.5) with the exception that the digital images are reconstructed (without any restoration) using Schade's RTF model. Consistent with figure (3.4), each of the three reconstructed images is more blurred than their corresponding PCC reconstructions; a distinct (albeit faint) checker-board pattern is also visible in all the reconstructed images. This checker-board pattern is present because Schade's display PSF model does not obey equation (3.17).

### 3.3 C/D/C Model-Based Digital Image Restoration

With the help of simulation, it was demonstrated in chapter 2 that if image acquisition blur is the only source of image degradation then digital restoration filtering can successfully remove essentially all of this degradation. If, however, the blurred digital image is also sampled and reconstructed, then the same digital restoration (inverse) filter no longer works satisfactorily. This illustrates that sampling and reconstruction introduces a significant image degradation that interferes with the

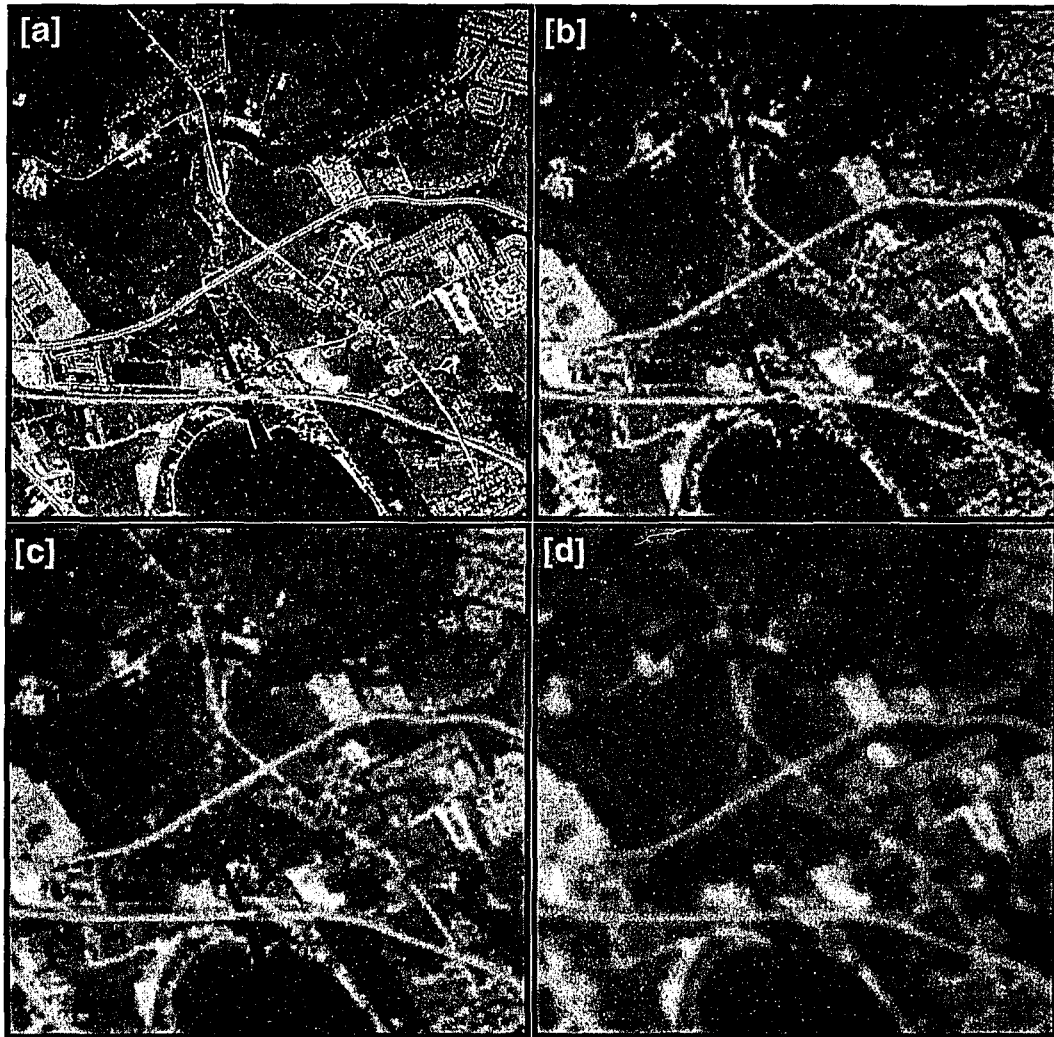


Figure 3.5: PCC reconstruction of the blurred and sampled aerial scene (no restoration).



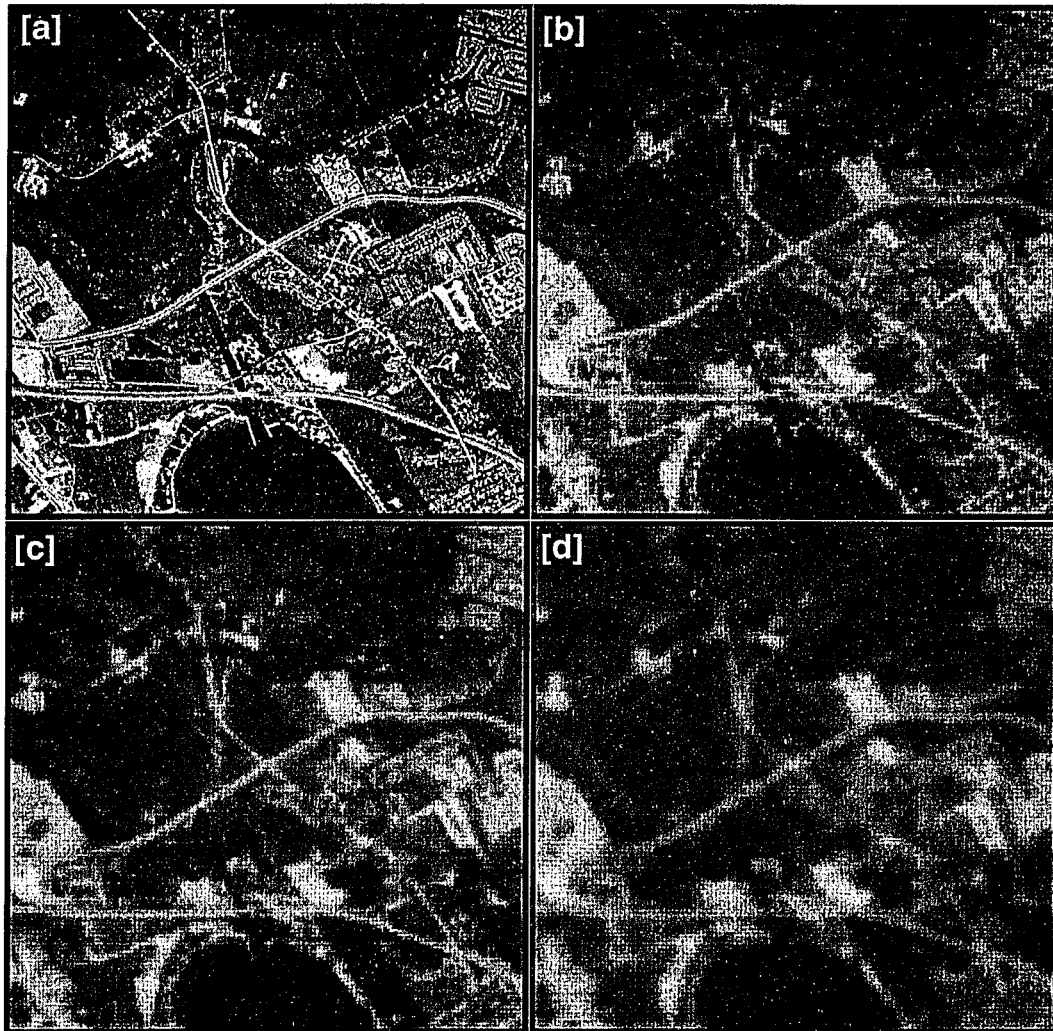


Figure 3.6: Display reconstruction of the blurred and sampled aerial scene (no restoration).

restoration process in a fundamental way. This section provides an explanation for the simulation results in chapter 2.<sup>7</sup> This explanation is based on a c/d/c model-based argument that pre-aliasing and post-aliasing (generally referred to as aliasing) together contribute *scene-dependent* aliased noise.<sup>8</sup> This scene-dependent aliased noise is enhanced by a high-boost restoration filter; the result is the kind of artifacts present in figures (2.10) and (2.12).

A theoretical justification for the characterization of aliasing as scene-dependent additive noise is based on the observation that the Fourier series coefficients of the reconstructed image, equation (3.12), can be written as

$$\hat{R}[\nu_1, \nu_2] = \hat{R}_c[\nu_1, \nu_2] + \hat{R}_e[\nu_1, \nu_2] + \hat{R}_a[\nu_1, \nu_2]. \quad (3.20)$$

The three terms on the right-hand-side of equation (3.20) are defined as follows.

The *cascaded* (or filtered) term is

$$\hat{R}_c[\nu_1, \nu_2] = \hat{D}(\nu_1/N_1, \nu_2/N_2) \hat{f}[\nu_1, \nu_2] \hat{H}(\nu_1/N_1, \nu_2/N_2) \hat{S}[\nu_1, \nu_2]. \quad (3.21)$$

This term corresponds to the end-to-end c/d/c system output with an accounting for the low-pass filtering effects of image acquisition, the high-boost filtering effects of image restoration and the low-pass filtering effects of image reconstruction. This term is analogous to the output of a c/c model.

---

<sup>7</sup>This section is based on material that appears in two recent SPIE articles, [62] and [78].

<sup>8</sup>There is a subtle difference in the model used for the simulation results presented in section 2.4 of chapter 2 and the c/d/c model in this chapter. In chapter 2, the underlying c/d/c model switched the order of the digital processing and image reconstruction modules.

The (scene-independent) *random noise* term is

$$\hat{R}_e[\nu_1, \nu_2] = \hat{D}(\nu_1/N_1, \nu_2/N_2) \hat{f}[\nu_1, \nu_2] \hat{e}[\nu_1, \nu_2]. \quad (3.22)$$

This term corresponds to the random effect of system noise, modulated by the high-boost filtering effect of image restoration and the low-pass filtering effect of image reconstruction. This term explains the random noise enhancement by a restoration filter, as demonstrated in figure (2.5). If the SNR is very high this term is effectively non-existent.

The scene-dependent *aliased noise* term is

$$\hat{R}_a[\nu_1, \nu_2] = \hat{D}(\nu_1/N_1, \nu_2/N_2) \hat{f}[\nu_1, \nu_2] \hat{a}[\nu_1, \nu_2]. \quad (3.23)$$

This term corresponds to the frequency folding effect of sampling, modulated by the high-boost filtering effect of image restoration and the low-pass filtering effects of image reconstruction. This term quantifies the extent to which pixel-scale (and larger) artifacts are created by pre-aliasing as well as the extent to which sub-pixel-scale artifacts are created by post-aliasing. As evident in figures (2.9) and (2.11), these artifacts are generally present even if the digital image is free of additive random noise. From equation (3.23) it is clear that restoration can enhance aliasing artifacts, as demonstrated in figures (2.10) and (2.12).

The spatial domain equivalent of equation (3.20) is

$$r(x_1, x_2) = r_c(x_1, x_2) + r_e(x_1, x_2) + r_a(x_1, x_2) \quad (3.24)$$

where

$$r_a(x_1, x_2) = \sum_{\nu_1=-\infty}^{\infty} \sum_{\nu_2=-\infty}^{\infty} \hat{R}_a[\nu_1, \nu_2] \exp(i2\pi\nu_1 x_1/N_1) \exp(i2\pi\nu_2 x_2/N_2) \quad (3.25)$$

is the aliased noise component image and  $r_c$ ,  $r_e$  are defined analogously.<sup>9</sup> From equation (3.24) it is clear that the aliased noise component image is an *additive* source of error (noise), much like random noise.

In support of the characterization of the aliased component image as scene-dependent additive noise, the aerial scene can be processed to generate the three component images. Figure (3.7) is a composite illustration of a reconstructed image along with the three component images. No digital restoration processing is employed — relative to figure (3.1) this means that  $p = q$ . Figure (3.7[a]) is the reconstructed image  $r$  produced by an OTF scale parameter of 0.75 and PCC reconstruction. The random noise SNR is 50. Figure (3.7[b]) is the cascaded component  $r_c$ , and figures (3.7[c]) and (3.7[d]) are the random and aliased noise components  $r_e$  and  $r_a$ , respectively. The reconstructed image and the cascaded component image are displayed “as is”, with no contrast-stretching. The noise component image and the aliased component image, however, have had their mean values shifted from zero to mid-gray and then have been independently contrast-stretched.

Consistent with the mathematical characterizations of the component images, when no restoration is performed the cascaded component, figure (3.7[b]), is a low-

---

<sup>9</sup>As DISCUSSEd in subsection 3.2.5, in practice the infinite summations in equation (3.25) and the analogous equations for  $r_c$  and  $r_e$  can be reduced to finite summations.

pass filtered version of the original scene, figure (3.5[a]). The random noise component, figure (3.7[c]), does not contain any meaningful (scene-related) spatial structure. Like the random noise component, the aliased component, figure (3.7[d]), is a noise image, but with a significant difference — the features present in the aliased component image correlate perfectly with the visual artifacts in the reconstructed image, figure (3.7[a]), providing a qualitative justification for the *scene-dependent* (additive) noise characterization of aliasing.

Figure (3.8) illustrates the effect of restoration on each component of the reconstructed image. Restoration is applied by using an ad-hoc (periodic) restoration filter whose frequency response in the sampling passband is given by

$$\hat{f}[\nu_1, \nu_2] = \frac{\hat{H}^*(\nu_1/N_1, \nu_2/N_2)\hat{D}^*(\nu_1/N_1, \nu_2/N_2)}{|\hat{H}(\nu_1/N_1, \nu_2/N_2)\hat{D}(\nu_1/N_1, \nu_2/N_2)|^2 + \epsilon^2}. \quad (3.26)$$

Periodicity is imposed by replicating this response beyond the sampling passband. The filter response is empirically modified by the parameter  $\epsilon$  to avoid unbounded response. This naive restoration filter accounts for image acquisition blurring and image reconstruction blurring but ignores aliasing and random noise; more comprehensive c/d/c model-based restoration filters are presented in chapters 4 and 5. In equation (3.26)  $\hat{H}$  is the OTF defined in equation (3.15) with  $\beta = 2.0$  and  $\sigma = 1.0$  and  $\hat{D}$  is the PCC RTF defined in equation (3.19); the value of  $\epsilon$  is 0.01. Figure (3.8) illustrates the resulting reconstructed and component images. Except for the use of this filter, the processing (including contrast-stretching for the purposes of display) is identical to the processing used to generate the images in figure (3.7).

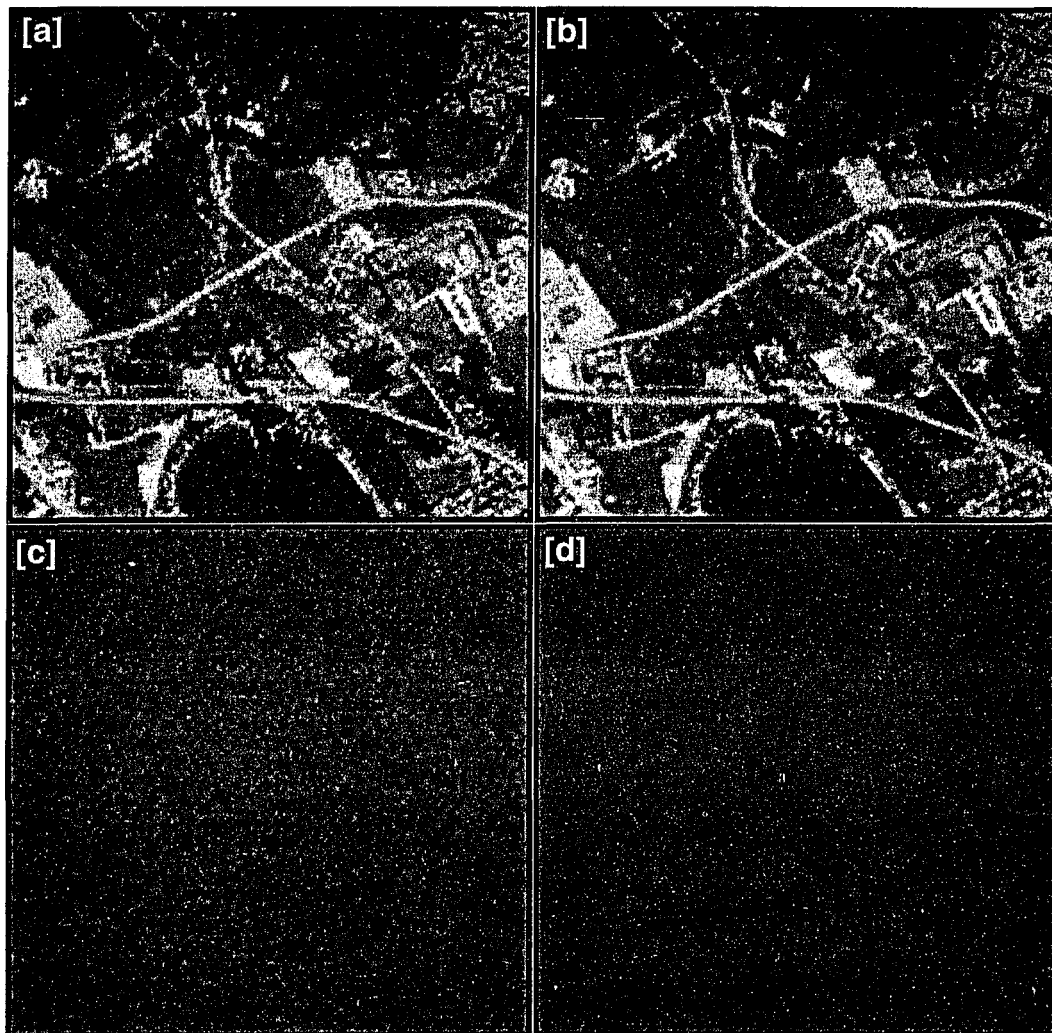


Figure 3.7: Reconstructed aerial and component images (no restoration).

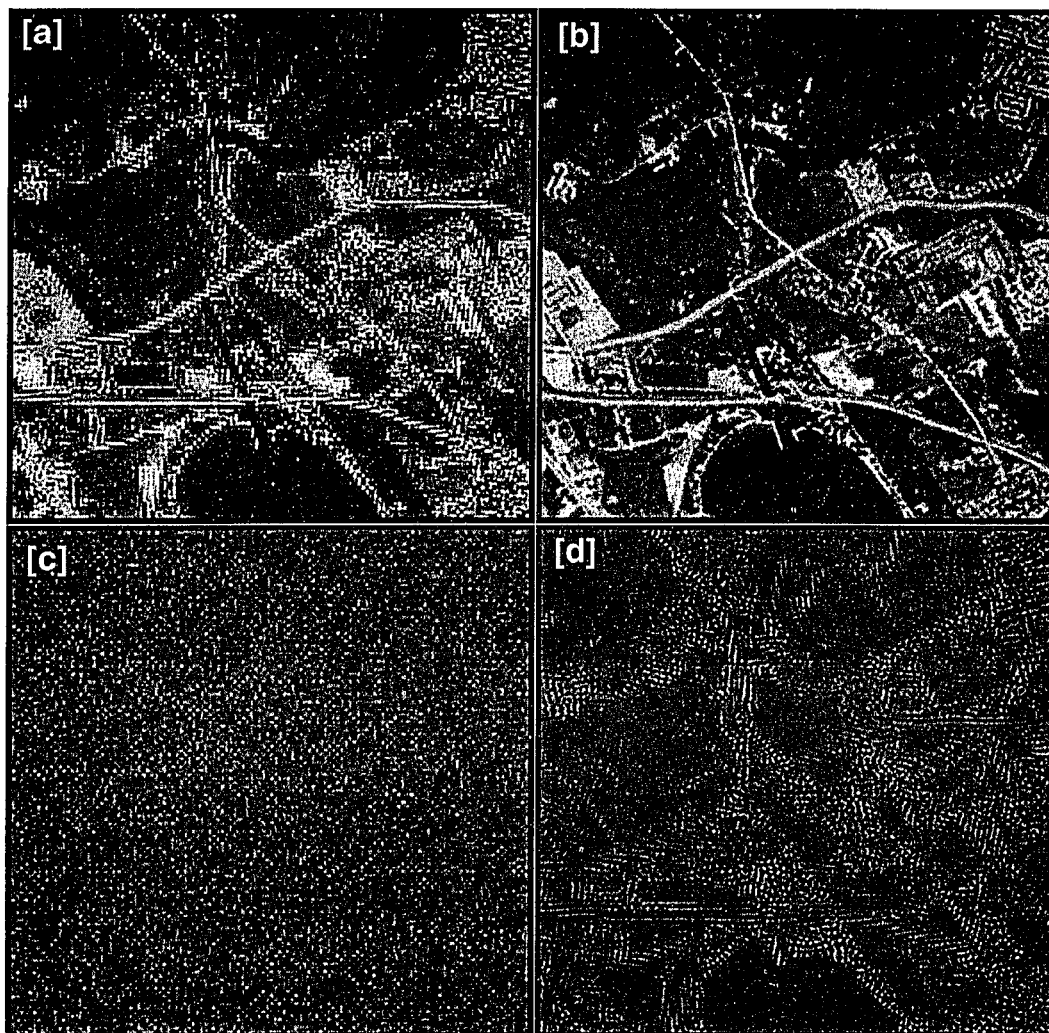


Figure 3.8: High-pass filtered aerial and component images.

The restoration filter defined in equation (3.26) attempts to compensate for the blurring produced by image acquisition and PCC reconstruction. The compensation is independent of  $\hat{a}[\nu_1, \nu_2]$  and  $\hat{e}[\nu_1, \nu_2]$ . Therefore, if the energy of either the aliased noise component or the random noise component (or both) is large at some frequencies, significant artifact enhancement will occur, as illustrated in figure (3.8). When the images in figure (3.8) are compared with the corresponding images in figure (3.7), the enhancement of both the random and aliased noise components is evident. Although the restored image in figure (3.8[a]) (which is physically realizable) and the cascaded component image in figure (3.8[b]) (which is *not* physically realizable) are considerably sharper, the net effect of using the inverse restoration filter is to corrupt the restored image with amplified aliasing artifacts.

As demonstrated in this section, (pre- and post-) aliasing due to sampling and reconstruction can be an important source of degradation in digital (sampled) imaging systems. For digital image restoration to be effective, a *c/d/c* system model must be used to account for sampling and reconstruction *and* the restoration technique must balance its high-boost action against the potential for enhancing both random and aliased noise. The *c/d/c* model-based Wiener and CLS restoration filters presented in chapters 4 and 5 are examples of such restoration techniques.



## CHAPTER IV

### C/D/C MODEL-BASED WIENER IMAGE RESTORATION

This chapter describes a c/d/c model-based Wiener restoration filter. The filter is derived by minimizing the expected end-to-end MSD between the reconstructed image and the ideal scene; in this sense the Wiener filter is optimal. Simulations presented in this chapter illustrate, however, that the c/d/c model-based Wiener has limited practical utility. That is, although it is optimal, the Wiener filter cannot be applied rigorously in a practical restoration application.

#### 4.1 Wiener Filter Derivation

Relative to the c/d/c system model in figure (3.1), the end-to-end MSD is

$$\|s - r\|^2 = \frac{1}{N_1 N_2} \int_0^{N_1} \int_0^{N_2} |s(x_1, x_2) - r(x_1, x_2)|^2 dx_1 dx_2. \quad (4.1)$$

From Parseval's equation, the spatial domain expression for the end-to-end MSD can be written in the frequency domain as

$$\|s - r\|^2 = \sum_{\nu_1=-\infty}^{\infty} \sum_{\nu_2=-\infty}^{\infty} |\hat{S}[\nu_1, \nu_2] - \hat{R}[\nu_1, \nu_2]|^2. \quad (4.2)$$

By using equations (3.7), (3.12) and (4.2), the end-to-end MSD can be expressed as

$$\|s - r\|^2 = \sum_{\nu_1=-\infty}^{\infty} \sum_{\nu_2=-\infty}^{\infty} |\hat{S}[\nu_1, \nu_2] - \hat{p}[\nu_1, \nu_2] \hat{f}[\nu_1, \nu_2] \hat{D}(\nu_1/N_1, \nu_2/N_2)|^2. \quad (4.3)$$

The c/d/c model-based Wiener filter is derived by assuming that the input scene is stochastic and then minimizing the *expected* end-to-end MSD. That is, the Wiener filter minimizes the restoration metric

$$J^2 = E[\|s - r\|^2]. \quad (4.4)$$

Because the c/d/c model-based Wiener filter minimizes the end-to-end MSD in an average sense, it will not, in general, minimize the end-to-end MSD for a particular scene. This is an important theoretical point that also has practical ramifications that are discussed in section 4.2.

For each frequency index pair  $[\nu_1, \nu_2]$ ,  $J^2$  is quadratic in the (complex-valued) unknown restoration filter coefficient  $\hat{f}[\nu_1, \nu_2]$ . That is,  $J^2$  can be expressed as

$$J^2 = \sum_{\nu_1=-\infty}^{\infty} \sum_{\nu_2=-\infty}^{\infty} \left( \hat{\Phi}_s[\nu_1, \nu_2] - \hat{B}[\nu_1, \nu_2] \hat{f}^*[\nu_1, \nu_2] - \hat{B}^*[\nu_1, \nu_2] \hat{f}[\nu_1, \nu_2] + \hat{A}[\nu_1, \nu_2] |\hat{f}[\nu_1, \nu_2]|^2 \right) \quad (4.5)$$

with the coefficients

$$\begin{aligned} \hat{B}[\nu_1, \nu_2] &= E[\hat{S}[\nu_1, \nu_2] \hat{p}^*[\nu_1, \nu_2] \hat{D}^*(\nu_1/N_1, \nu_2/N_2)] \\ \hat{A}[\nu_1, \nu_2] &= \hat{\Phi}_p[\nu_1, \nu_2] |\hat{D}(\nu_1/N_1, \nu_2/N_2)|^2 \end{aligned} \quad (4.6)$$

where  $\hat{\Phi}_p[\nu_1, \nu_2] = E[|\hat{p}[\nu_1, \nu_2]|^2]$  denotes the expected energy of the digital image and  $\hat{\Phi}_s[\nu_1, \nu_2] = E[|\hat{S}[\nu_1, \nu_2]|^2]$  is the expected energy of the scene.

Since the restoration filter is periodic with period  $N_1 \times N_2$ , only a *finite* number of restoration filter transfer values can be specified. For that reason, it is desirable

to reduce equation (4.5) to a sum over a  $N_1 \times N_2$  frequency period. This objective can be achieved by using the following lemma.<sup>1</sup>

**Lemma 4.1.1** *Let  $\hat{\Gamma}[\nu_1, \nu_2]$  be a complex-valued aperiodic sequence and  $\hat{\Delta}[\nu_1, \nu_2]$  be a complex-valued periodic sequence with period  $N_1 \times N_2$ . If*

$$\langle \hat{\Gamma}[\nu_1, \nu_2] \rangle = \sum_{k_1=-\infty}^{\infty} \sum_{k_2=-\infty}^{\infty} \hat{\Gamma}[\nu_1 - k_1 N_1, \nu_2 - k_2 N_2]$$

*is absolutely convergent for all  $[\nu_1, \nu_2]$  then :*

(i) *the sequence defined by  $\langle \hat{\Gamma}[\nu_1, \nu_2] \rangle$  is periodic with period  $N_1 \times N_2$ ;*

(ii)

$$\langle \hat{\Gamma}^*[\nu_1, \nu_2] \rangle = \langle \hat{\Gamma}[\nu_1, \nu_2] \rangle^* ;$$

(iii)

$$\sum_{\nu_1=-\infty}^{\infty} \sum_{\nu_2=-\infty}^{\infty} \hat{\Delta}[\nu_1, \nu_2] \hat{\Gamma}[\nu_1, \nu_2] = \sum_{\nu_1=0}^{N_1-1} \sum_{\nu_2=0}^{N_2-1} \hat{\Delta}[\nu_1, \nu_2] \langle \hat{\Gamma}[\nu_1, \nu_2] \rangle ;$$

(iv)

$$\langle \hat{\Delta}[\nu_1, \nu_2] \hat{\Gamma}[\nu_1, \nu_2] \rangle = \hat{\Delta}[\nu_1, \nu_2] \langle \hat{\Gamma}[\nu_1, \nu_2] \rangle .$$

---

<sup>1</sup>A 1-D equivalent of part (iii) of this lemma appears without proof in [13].

**Proof:**

(i) The periodicity of the sequence defined by  $\langle \hat{\Gamma}[\nu_1, \nu_2] \rangle$  is established as follows:

$$\begin{aligned}
 \langle \hat{\Gamma}[\nu_1 + N_1, \nu_2 + N_2] \rangle &= \sum_{k_1=-\infty}^{\infty} \sum_{k_2=-\infty}^{\infty} \hat{\Gamma}[\nu_1 - k_1 N_1 + N_1, \nu_2 - k_2 N_2 + N_2] \\
 &= \sum_{k_1=-\infty}^{\infty} \sum_{k_2=-\infty}^{\infty} \hat{\Gamma}[\nu_1 - N_1(k_1 - 1), \nu_2 - N_2(k_2 - 1)] \\
 &= \sum_{k'_1=-\infty}^{\infty} \sum_{k'_2=-\infty}^{\infty} \hat{\Gamma}[\nu_1 - k'_1 N_1, \nu_2 - k'_2 N_2] \\
 &= \langle \hat{\Gamma}[\nu_1, \nu_2] \rangle.
 \end{aligned}$$

The proof of (ii) follows from the observation that the  $\langle \cdot \rangle$  operator and the complex conjugation operator are both linear. Therefore, their relative order can be interchanged without affecting the result.

The proof of (iii) is based on the following counting argument:

$$\begin{aligned}
 &\sum_{\nu_1=-\infty}^{\infty} \sum_{\nu_2=-\infty}^{\infty} \hat{\Delta}[\nu_1, \nu_2] \hat{\Gamma}[\nu_1, \nu_2] \\
 &= \sum_{k_1=-\infty}^{\infty} \sum_{k_2=-\infty}^{\infty} \left( \sum_{\nu_1=0}^{N_1-1} \sum_{\nu_2=0}^{N_2-1} \hat{\Delta}[\nu_1 - k_1 N_1, \nu_2 - k_2 N_2] \hat{\Gamma}[\nu_1 - k_1 N_1, \nu_2 - k_2 N_2] \right) \\
 &= \sum_{\nu_1=0}^{N_1-1} \sum_{\nu_2=0}^{N_2-1} \sum_{k_1=-\infty}^{\infty} \sum_{k_2=-\infty}^{\infty} \hat{\Delta}[\nu_1, \nu_2] \hat{\Gamma}[\nu_1 - k_1 N_1, \nu_2 - k_2 N_2] \\
 &= \sum_{\nu_1=0}^{N_1-1} \sum_{\nu_2=0}^{N_2-1} \hat{\Delta}[\nu_1, \nu_2] \sum_{k_1=-\infty}^{\infty} \sum_{k_2=-\infty}^{\infty} \hat{\Gamma}[\nu_1 - k_1 N_1, \nu_2 - k_2 N_2] \\
 &= \sum_{\nu_1=0}^{N_1-1} \sum_{\nu_2=0}^{N_2-1} \hat{\Delta}[\nu_1, \nu_2] \langle \hat{\Gamma}[\nu_1, \nu_2] \rangle.
 \end{aligned}$$

The proof of (iv) can be established as follows:

$$\begin{aligned}
& \langle \hat{\Delta}[\nu_1, \nu_2] \hat{\Gamma}[\nu_1, \nu_2] \rangle \\
&= \sum_{k_1=-\infty}^{\infty} \sum_{k_2=-\infty}^{\infty} \hat{\Delta}[\nu_1 - k_1 N_1, \nu_2 - k_2 N_2] \hat{\Gamma}[\nu_1 - k_1 N_1, \nu_2 - k_2 N_2] \\
&= \hat{\Delta}[\nu_1, \nu_2] \sum_{k_1=-\infty}^{\infty} \sum_{k_2=-\infty}^{\infty} \hat{\Gamma}[\nu_1 - k_1 N_1, \nu_2 - k_2 N_2] \\
&= \hat{\Delta}[\nu_1, \nu_2] \langle \hat{\Gamma}[\nu_1, \nu_2] \rangle.
\end{aligned}$$

**Q.E.D**

Using lemma 4.1.1, equation (4.4) reduces to

$$\begin{aligned}
J^2 &= \sum_{\nu_1=0}^{N_1-1} \sum_{\nu_2=0}^{N_2-1} \left( \langle \hat{\Phi}_s[\nu_1, \nu_2] \rangle - \langle \hat{B}[\nu_1, \nu_2] \rangle \hat{f}^*[\nu_1, \nu_2] \right. \\
&\quad \left. - \langle \hat{B}[\nu_1, \nu_2] \rangle^* \hat{f}[\nu_1, \nu_2] + \langle \hat{A}[\nu_1, \nu_2] \rangle |\hat{f}[\nu_1, \nu_2]|^2 \right) \quad (4.7)
\end{aligned}$$

where, as a result of the  $N_1 \times N_2$  periodicity of  $\hat{p}[\nu_1, \nu_2]$ ,  $\hat{\Phi}_p[\nu_1, \nu_2]$  and  $\hat{f}[\nu_1, \nu_2]$ ,

$$\begin{aligned}
\langle \hat{B}[\nu_1, \nu_2] \rangle &= E[\hat{p}^*[\nu_1, \nu_2] \langle \hat{S}[\nu_1, \nu_2] \hat{D}^*(\nu_1/N_1, \nu_2/N_2) \rangle] \\
\langle \hat{A}[\nu_1, \nu_2] \rangle &= \hat{\Phi}_p[\nu_1, \nu_2] \langle |\hat{D}(\nu_1/N_1, \nu_2/N_2)|^2 \rangle. \quad (4.8)
\end{aligned}$$

For each  $[\nu_1, \nu_2]$ , the minimum expected MSD is determined by choosing  $\hat{f}[\nu_1, \nu_2]$  to minimize  $J^2$ ; this minimization can be accomplished by completing the square as

$$J^2 = J_{\min}^2 + \sum_{\nu_1=0}^{N_1-1} \sum_{\nu_2=0}^{N_2-1} \langle \hat{A}[\nu_1, \nu_2] \rangle |\hat{f}[\nu_1, \nu_2] - \hat{f}_w[\nu_1, \nu_2]|^2 \quad (4.9)$$

where the (periodic) c/d/c model-based Wiener filter is <sup>2</sup>

$$\hat{f}_w[\nu_1, \nu_2] = \frac{\langle \hat{B}[\nu_1, \nu_2] \rangle}{\langle \hat{A}[\nu_1, \nu_2] \rangle} \quad (4.10)$$

---

<sup>2</sup>If the denominator in equation (4.10) is zero then, by convention,  $\hat{f}_w[\nu_1, \nu_2] = 0$ .

and

$$J_{\min}^2 = \sum_{\nu_1=0}^{N_1-1} \sum_{\nu_2=0}^{N_2-1} \left( \hat{\Phi}_s[\nu_1, \nu_2] - |\hat{f}_w[\nu_1, \nu_2]|^2 \langle \hat{A}[\nu_1, \nu_2] \rangle \right) \quad (4.11)$$

is the residual error, *independent* of  $\hat{f}$ . Each term in the summation in equation (4.9) is non-negative; this is used to prove the following theorem which establishes that the c/d/c model-based Wiener filter defined in equation (4.10) is the optimal linear restoration filter.

**Theorem 4.1.2** *If  $\langle \hat{A}[\nu_1, \nu_2] \rangle \neq 0$  for all  $[\nu_1, \nu_2]$  then  $J^2$  achieves its minimum value of  $J_{\min}^2$  if and only if  $\hat{f}[\nu_1, \nu_2] = \hat{f}_w[\nu_1, \nu_2]$  for all  $[\nu_1, \nu_2]$  where  $\hat{f}_w[\nu_1, \nu_2]$  is defined by equation (4.10).*

To evaluate the numerator and the denominator in equation (4.10), it is necessary to make statistical assumptions about the scene and the random noise [14]. One statistical assumption is that the scene's sidebands are uncorrelated so that

$$E[\hat{S}[\nu_1, \nu_2] \hat{S}^*[\nu_1 + k_1 N_1, \nu_2 + k_2 N_2]] = \begin{cases} \hat{\Phi}_s[\nu_1, \nu_2] & [k_1, k_2] = [0, 0] \\ 0 & \text{otherwise.} \end{cases} \quad (4.12)$$

For a band-limited scene, most of these terms are naturally zero; the number of possibly non-zero terms, if any, is determined by the scene's cut-off frequency and the sampling frequency. In general, only the  $|k_1| \leq \tau_1/N_1, |k_2| \leq \tau_2/N_2$  sideband terms are potentially non-zero. The uncorrelated sideband assumption forces *all* of these terms to be zero. The other statistical assumption is that the additive random

noise is zero-mean and scene-independent so that

$$\begin{aligned} E[\hat{S}[\nu_1, \nu_2]\hat{e}[\nu_1, \nu_2]] &= 0 & E[\hat{S}[\nu_1, \nu_2]\hat{e}^*[\nu_1, \nu_2]] &= 0 \\ E[\hat{S}^*[\nu_1, \nu_2]\hat{e}[\nu_1, \nu_2]] &= 0 & E[\hat{S}^*[\nu_1, \nu_2]\hat{e}^*[\nu_1, \nu_2]] &= 0 \end{aligned} \quad (4.13)$$

As a consequence of these two statistical assumptions, equation (4.8) can be simplified to

$$\begin{aligned} \langle \hat{B}[\nu_1, \nu_2] \rangle &= \langle \hat{\Phi}_s[\nu_1, \nu_2] \hat{H}^*(\nu_1/N_1, \nu_2/N_2) \hat{D}^*(\nu_1/N_1, \nu_2/N_2) \rangle \\ \langle \hat{A}[\nu_1, \nu_2] \rangle &= \langle \hat{\Phi}_s[\nu_1, \nu_2] |\hat{H}(\nu_1/N_1, \nu_2/N_2)|^2 + \hat{\Phi}_a[\nu_1, \nu_2] + \hat{\Phi}_e[\nu_1, \nu_2] \rangle \\ &\quad \langle |\hat{D}(\nu_1/N_1, \nu_2/N_2)|^2 \rangle \end{aligned} \quad (4.14)$$

where  $\hat{\Phi}_e[\nu_1, \nu_2] = E[|\hat{e}[\nu_1, \nu_2]|^2]$  is the expected energy of the random noise and

$$\hat{\Phi}_a[\nu_1, \nu_2] = \sum_{[k_1, k_2] \neq [0, 0]} \hat{\Phi}_s[\nu_1 - k_1 N_1, \nu_2 - k_2 N_2] |\hat{H}(\nu_1/N_1 - k_1, \nu_2/N_2 - k_2)|^2 \quad (4.15)$$

is the expected energy of the aliased noise. The resulting form of the c/d/c model-based Wiener filter is summarized by the following corollary to theorem 4.1.2.

**Corollary 4.1.3** *If the two statistical assumptions stated in equations (4.12) and (4.13) are true, then the c/d/c model-based Wiener filter is*

$$\hat{f}_w[\nu_1, \nu_2] = \frac{\langle \hat{B}[\nu_1, \nu_2] \rangle}{\langle \hat{A}[\nu_1, \nu_2] \rangle}$$

where  $\langle \hat{A}[\nu_1, \nu_2] \rangle$  and  $\langle \hat{B}[\nu_1, \nu_2] \rangle$  are defined in equation (4.14).

This simplified Wiener filter reduces to the d/d model-based Wiener restoration filter (equation (2.13)) if the following c/d/c model conditions are satisfied:

- $\hat{\Phi}_a[\nu_1, \nu_2] = 0$  within the sampling passband;
- $\hat{D}(\omega_1, \omega_2) = 1$  within the sampling passband;
- $\hat{D}(\omega_1, \omega_2) = 0$  outside the sampling passband;

When these three conditions are satisfied, the folded terms in the numerator and the denominator in corollary 4.1.3 are zero in the sampling passband. That is, for  $(\nu_1/N_1, \nu_2/N_2)$  in the sampling passband the numerator and the denominator are

$$\begin{aligned}\langle \hat{B}[\nu_1, \nu_2] \rangle &= \hat{\Phi}_s[\nu_1, \nu_2] \hat{H}^*(\nu_1/N_1, \nu_2/N_2) \\ \langle \hat{A}[\nu_1, \nu_2] \rangle &= \hat{\Phi}_s[\nu_1, \nu_2] |\hat{H}(\nu_1/N_1, \nu_2/N_2)|^2 + \hat{\Phi}_e[\nu_1, \nu_2].\end{aligned}\quad (4.16)$$

If both coefficients are divided by  $\hat{\Phi}_s[\nu_1, \nu_2]$  (assuming that this term is non-zero for all frequency index pairs  $[\nu_1, \nu_2]$ ), the result is the d/d model-based Wiener filter response defined in equation (2.13).

The “ $\hat{\Phi}_a[\nu_1, \nu_2] = 0$  within the sampling passband” condition is a mathematical description of sufficient sampling. The pre-sampled image  $g = s \oplus h$  is sufficiently sampled only if the scene  $s$  does not have any energy beyond the sampling passband or the PSF  $h$  rejects all frequencies outside the sampling passband. The “ $\hat{D}(\omega_1, \omega_2) = 1$  within the sampling passband” and the “ $\hat{D}(\omega_1, \omega_2) = 0$  outside the sampling passband” conditions jointly require that the reconstruction PSF must be the sinc reconstruction PSF

$$d(x_1, x_2) = \frac{\sin(\pi x_1)}{\pi x_1} \frac{\sin(\pi x_2)}{\pi x_2}. \quad (4.17)$$



As discussed in chapters 2 and 3, the assumptions about sufficient sampling and sinc reconstruction are unrealistic because in practice aliasing and non-ideal reconstruction are inevitable. Therefore, in practice the c/d/c model-based Wiener filter does not reduce to the d/d model-based Wiener filter.

## 4.2 Wiener Restoration Problems

Although the c/d/c model-based Wiener filter is, in theory, the MSD optimal linear restoration filter, there are several *conceptual* and *computational* problems associated with any implementation of this filter. In particular, the computational problem makes it difficult to apply the Wiener filter rigorously in practical restoration applications.

### 4.2.1 Conceptual Problems

To apply the simplified Wiener filter rigorously,  $\hat{\Phi}_s[\nu_1, \nu_2]$  has to be known for every  $|\nu_1| \leq \tau_1, |\nu_2| \leq \tau_2$ . Also  $\hat{\Phi}_e[\nu_1, \nu_2]$  has to be known at each frequency in the sampling passband. Because they are ensemble-averaged statistics, in a practical restoration application these energy spectra are never known; they have to be estimated from the noisy, sampled digital image. If  $|\hat{S}[\nu_1, \nu_2]|^2$  and  $|\hat{e}[\nu_1, \nu_2]|^2$  are known, as they are in a simulation environment, then it is natural to use them as estimates of  $\hat{\Phi}_s[\nu_1, \nu_2]$  and  $\hat{\Phi}_e[\nu_1, \nu_2]$ . Doing so is analogous to using *one* sample data point to estimate an unknown population statistic; the result is not the c/d/c model-based Wiener

restoration filter defined in corollary 4.1.3.

In addition, the two statistical assumptions used to derive the simplified Wiener filter also create conceptual problems. The scene-independent, zero-mean random noise assumption, equation (4.13), is a common assumption for many d/d model-based restoration filters including the d/d model-based Wiener filter presented in chapter 2. For some applications, this assumption may be valid. For example, if quantization is the only source of random noise in the system, then it is correctly modeled as scene-independent, zero-mean noise. For most digital imaging systems, however, quantization is *not* the only source of random noise. The electronic components of the image acquisition system also contribute random noise (for example, shot-noise and dark-current noise) that may dominate quantization noise. Unlike quantization noise, this “electronic” noise may not be scene-independent or zero-mean [79]. If so, then the Wiener filter indicated in corollary (4.1.3) is not optimal.

Like the statistical assumption about the random noise, the assumption about uncorrelated scene sidebands, equation (4.12), is another example of the use of some statistical license. Some after-the-fact theoretical justification for this assumption can be provided only for limited interpretations of an “ensemble” of scenes. For example, if the scene ensemble is defined to be the (infinite) collection of randomly sub-pixel shifted versions of a particular scene, then the uncorrelated sidebands assumption can be shown to be true [80]. For a general ensemble, however, there is no assurance that the uncorrelated sidebands assumption is necessarily valid.

### 4.2.2 Computational Problems

To compute the simplified Wiener filter values using corollary 4.1.3 it is necessary to know  $\hat{\Phi}_s[\nu_1, \nu_2]$  and  $\hat{\Phi}_e[\nu_1, \nu_2]$ . As discussed in subsection 4.2.1, however, these two statistics are unknown and it is virtually impossible to estimate them. Estimation of the corresponding sample statistics  $|\hat{S}[\nu_1, \nu_2]|^2$  and  $|\hat{e}[\nu_1, \nu_2]|^2$  is possible. In general,  $|\hat{S}[\nu_1, \nu_2]|^2$  is much harder to estimate than  $|\hat{e}[\nu_1, \nu_2]|^2$  [65].

Spectral estimation has been a much researched problem in the context of a d/d model [81]–[88]. For a d/d model, assuming that the additive random noise is zero-mean and independent of the scene, the energy spectrum of the scene is related to the energy spectrum of the digital image as

$$\hat{\Phi}_p[\nu_1, \nu_2] = \hat{\Phi}_s[\nu_1, \nu_2]|\hat{h}[\nu_1, \nu_2]|^2 + \hat{\Phi}_e[\nu_1, \nu_2]. \quad (4.18)$$

For a given digital image it is  $|\hat{p}[\nu_1, \nu_2]|^2$  not  $\hat{\Phi}_p[\nu_1, \nu_2]$ , that is known. Therefore, for the purpose of spectral estimation, equation (4.18) is replaced by

$$|\hat{p}[\nu_1, \nu_2]|^2 = |\hat{s}[\nu_1, \nu_2]|^2|\hat{h}[\nu_1, \nu_2]|^2 + |\hat{e}[\nu_1, \nu_2]|^2. \quad (4.19)$$

Although this equation can be solved for  $|\hat{s}[\nu_1, \nu_2]|^2$  provided  $|\hat{p}[\nu_1, \nu_2]|^2$ ,  $|\hat{h}[\nu_1, \nu_2]|^2$  and  $|\hat{e}[\nu_1, \nu_2]|^2$  are known for all  $[\nu_1, \nu_2]$ ,  $|\hat{e}[\nu_1, \nu_2]|^2$  is never known with perfect accuracy in practice, and so the solution for  $|\hat{s}[\nu_1, \nu_2]|^2$  derived from equation (4.19) will always have an associated error. In general, this error will be small at low frequencies but significant at the higher frequencies where  $|\hat{e}[\nu_1, \nu_2]|^2$  may be large relative to  $|\hat{s}[\nu_1, \nu_2]|^2|\hat{h}[\nu_1, \nu_2]|^2$ . If the resulting estimate of  $|\hat{s}[\nu_1, \nu_2]|^2$  is less

than  $\hat{\Phi}_s[\nu_1, \nu_2]$  then the Wiener filter will not sharpen adequately at that frequency. If, instead, the estimated  $|\hat{S}[\nu_1, \nu_2]|^2$  is greater than  $\hat{\Phi}_s[\nu_1, \nu_2]$  then the Wiener filter will sharpen more than necessary at that frequency, perhaps boosting random noise in the process.

Spectral estimation in the context of a c/d/c model is an even greater challenge due to the presence of both random noise *and* aliased noise. The c/d/c model analog to equation (4.19) is

$$|\hat{p}[\nu_1, \nu_2]|^2 = |\hat{S}[\nu_1, \nu_2]|^2 |\hat{H}(\nu_1/N_1, \nu_2/N_2)|^2 + |\hat{e}[\nu_1, \nu_2]|^2 + |\hat{a}[\nu_1, \nu_2]|^2. \quad (4.20)$$

Unlike equation (4.19), because of the presence of the unknown aliased noise term  $|\hat{a}[\nu_1, \nu_2]|^2$  equation (4.20) cannot be solved for  $|\hat{S}[\nu_1, \nu_2]|^2$  even if  $|\hat{e}[\nu_1, \nu_2]|^2$  is known. Because of these problems, as demonstrated in section 4.3, for a c/d/c model the use of *parametric models* for the scene's energy spectrum to synthesize the Wiener filter is more acceptable than the direct estimation approach.

### 4.3 Simulated Wiener Restorations

As in chapters 2 and 3, in this section a simulation is used to illustrate model-based Wiener restoration filtering. The simulation compares the c/d/c model-based Wiener restoration obtained by using  $|\hat{S}[\nu_1, \nu_2]|^2$  to estimate  $\hat{\Phi}_s[\nu_1, \nu_2]$  with a more practical Wiener restoration in which a parametric model is used to esti-

mate  $\hat{\Phi}_s[\nu_1, \nu_2]$ .<sup>3</sup> The Wiener restoration filter obtained by using  $|\hat{S}[\nu_1, \nu_2]|^2$  instead of  $\hat{\Phi}_s[\nu_1, \nu_2]$  provides a reference for visual comparison. This simulation illustrates that the mathematical rigor associated with the c/d/c model-based Wiener filter derivation is lost when ad-hoc techniques are used to compute the filter transfer function values. Moreover, accurate restoration using such an ad-hoc technique requires significant computational effort.

The  $512 \times 512$  aerial image, figure (4.1[a]), is blurred with the Gaussian OTF defined by equation (3.15) with  $\sigma = 0.25$  cycles/pixel. As illustrated in figure (3.3[d]), this OTF produces significant image acquisition blurring; the corresponding digital image is therefore, a good candidate for restoration. The result is sampled on a  $128 \times 128$  pixel grid. Uniformly distributed random noise with  $\text{SNR} = 32$  is added to the sampled image. Figure (4.1[b]) is the PCC reconstruction of this sampled image, without restoration. Figure (4.1[c]) and (4.1[d]) are the two Wiener restored images, again using PCC reconstruction. To generate figure (4.1[c]), the Wiener filter is computed by using  $|\hat{S}[\nu_1, \nu_2]|^2$  for  $\hat{\Phi}_s[\nu_1, \nu_2]$  and  $|\hat{e}[\nu_1, \nu_2]|^2$  for  $\hat{\Phi}_e[\nu_1, \nu_2]$ . To generate figure (4.1[d]), the Wiener filter is computed by using a parametric energy spectrum model proposed by Modestino et al. [63]

$$\hat{\Phi}_s[\nu_1, \nu_2] = \frac{2\pi\mu}{\mu^2 + 4\pi^2((\nu_1/N_1)^2 + (\nu_2/N_2)^2)^{3/2}} \quad (4.21)$$

The model parameter  $\mu$  corresponds to the mean spatial detail of the scene (in

---

<sup>3</sup>In this simulation the actual energy in the random noise is used in each case to isolate the scene spectral estimation problem.

pixel dimensions) and controls the extent to which the scene has energy at high frequencies — the smaller the value of  $\mu$ , the greater the presence of high contrast, pixel-scale features in the scene.

To use equation (4.21) a best value of  $\mu$  was computed as follows. First, two boundary values,  $\mu = 0.5$  pixels and  $\mu = 7.0$  pixels were chosen arbitrarily. These boundary values correspond to two different scene energy spectra; 0.5 corresponds to the case where the model over-estimates the true scene energy spectrum and 7.0 corresponds to the case where the model under-estimates the true scene energy spectrum. Beginning with  $\mu = 0.5$  and ending with  $\mu = 7.0$ , 14 restored (and reconstructed) images were produced at  $\mu$  intervals of 0.5. To avoid having to choose the best restoration solely by the subjective process of visual inspection, each reconstructed image was “fed-back” into the image acquisition system to generate a (noise-free) digital image  $p'$ . That is, each reconstructed image  $r$  was blurred by the same Gaussian OTF used to generate  $p$ ;  $r \oplus h$  was then sampled on a  $128 \times 128$  grid to create each  $p'$ . The reconstructed image for which

$$\|p - p'\|^2 = \frac{1}{N_1 N_2} \sum_{n_1=0}^{N_1-1} \sum_{n_2=0}^{N_2-1} |p[n_1, n_2] - p'[n_1, n_2]|^2 \quad (4.22)$$

was the *smallest* was selected as the best realizable Wiener restoration. For this simulation,  $\mu = 1.5$  yielded the lowest value of  $\|p - p'\|^2$ ; the corresponding restored image, reconstructed using PCC, is illustrated in figure (4.1[d]). Figures (4.1[c]) and (4.1[d]) are virtually indistinguishable demonstrating that this feed-back technique produces accurate restorations, albeit with a great deal of computational effort.

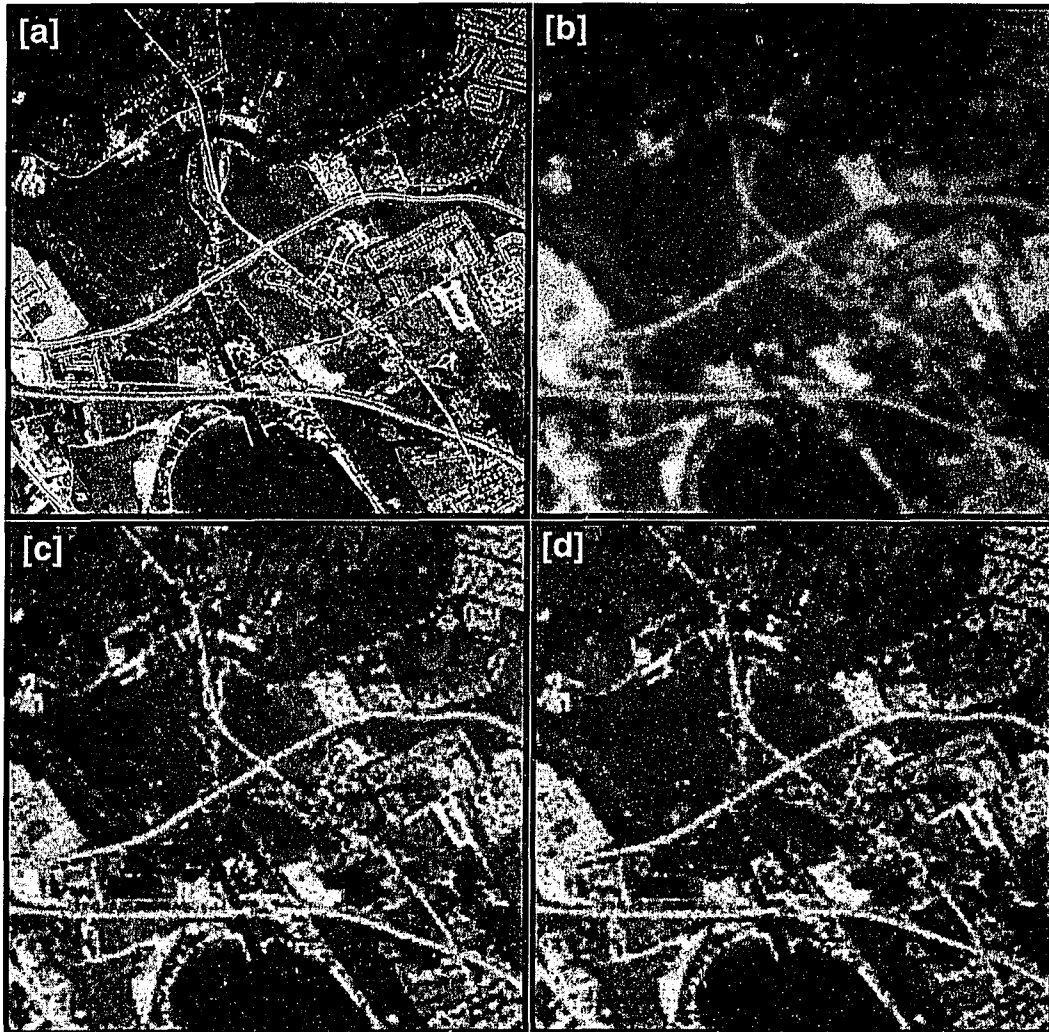


Figure 4.1: Simulated  $c/d/c$  model-based Wiener restorations.

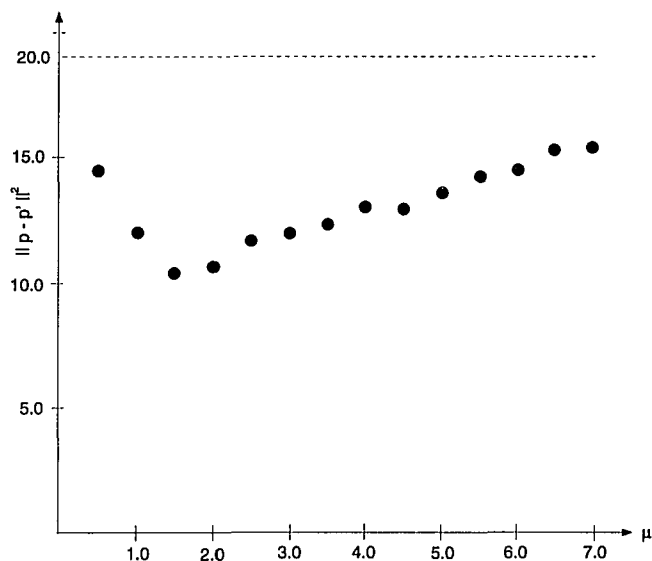


Figure 4.2:  $\|p - p'\|^2$  versus  $\mu$ .

Had this computational effort not been expended (for example, if a value of  $\mu$  had been chosen arbitrarily), the quality of the restored image may not have been as good. Figure (4.2) illustrates the variation of  $\|p - p'\|^2$  versus  $\mu$  for the 14 candidate restorations. The dotted line in figure (4.2) is the value of  $\|p - p'\|^2$  for the unrestored image.

The simulation presented in this section illustrates that although the c/d/c model-based Wiener filter is derived with considerable mathematical rigor, its implementation generally relies on ad-hoc techniques to refine the  $\hat{\Phi}_s[\nu_1, \nu_2]$  estimate; this process can require significant computation. Compared to the Wiener filter, the CLS restoration filter described in chapter 5 generates near-optimal restorations rigorously.



# CHAPTER V

## C/D/C MODEL-BASED CLS IMAGE RESTORATION

Although restoration filters based on a d/d system model do not account for image sampling and reconstruction, the traditional CLS filter is based on such a model [43]. This is a problem because, as demonstrated in chapter 2, failure to account for sampling and reconstruction can produce unsatisfactory restorations. In this chapter, the traditional d/d model-based CLS restoration filter is extended to account for sampling and reconstruction by using a c/d/c system model.<sup>1</sup> In comparison to the derivation of the c/d/c model-based Wiener restoration filter, the derivation of the c/d/c model-based CLS restoration filter is intuitively more acceptable because statistical assumptions about the unknown scene and the random noise are *not* required. For this reason, unlike the c/d/c model-based Wiener filter, the c/d/c model-based CLS restoration filter can be applied rigorously. Simulated restorations are presented to demonstrate the effectiveness of the c/d/c model-based CLS restoration filter for a range of imaging conditions.

---

<sup>1</sup>A 1-D c/d/c model-based CLS filter derivation was presented in a recent article [89]. This chapter extends that derivation to 2-D.

## 5.1 CLS Filter Derivation

Constrained least-squares (CLS) image restoration is a linear image restoration technique in which the *smoothness* of the restored image is maximized subject to a constraint on the fidelity of the restored image. In this context smoothness is a subjective attribute of image quality that is used to describe the extent to which an image lacks high-frequency pixel-scale detail. Controlling image smoothness in restoration applications is important because, as illustrated in chapters 2 and 3, high-frequency features may be spurious, enhanced noise.

Relative to the c/d/c model in figure (3.1), the objective of CLS restoration is to design the restoration filter  $f$  so that the restored image  $r$  is indistinguishable from the original scene  $s$  in the sense that if both  $r$  and  $s$  were input to this model then, except for additive random noise, they would produce statistically indistinguishable digital images. In general, infinitely many choices of the restoration filter can satisfy this objective. For this reason, the CLS filter derivation regularizes the restoration process by imposing a smoothness constraint on the restored image, thereby making the restoration filter well-defined. The CLS restoration metric thus consists of a *smoothness* term

$$S^2 = \|c \oplus r\|^2 = \frac{1}{N_1 N_2} \int_0^{N_1} \int_0^{N_2} |c(x_1, x_2) \oplus r(x_1, x_2)|^2 dx_1 dx_2 \quad (5.1)$$

and a *fidelity* term

$$F^2 = \|p - p'\|^2 = \frac{1}{N_1 N_2} \sum_{n_1=0}^{N_1-1} \sum_{n_2=0}^{N_2-1} |p[n_1, n_2] - p'[n_1, n_2]|^2. \quad (5.2)$$

The smoothness term  $S^2$  is stated in terms of a *user specified* (continuous, aperiodic) high-pass filter convolution kernel  $c$ . If the restoration filter is chosen to make the smoothness term small, restored images are rejected that would otherwise possess a great deal of potentially spurious energy at high frequencies. As illustrated in chapter 3, this rejection is desirable because spurious high frequency energy tends to manifest itself as patterned noise in the restored image.

The fidelity term  $F^2$  is the MSD between the (known) digital image  $p$  and the hypothetical digital image  $p'$  that would be generated if the input scene were  $r$ . From lemma 4.1.1 and the c/d/c model equations in chapter 3 the DFT array corresponding to  $p'$  is

$$\begin{aligned}\hat{p}'[\nu_1, \nu_2] &= \langle \hat{R}[\nu_1, \nu_2] \hat{H}(\nu_1/N_1, \nu_2/N_2) \rangle \\ &= \langle \hat{p}[\nu_1, \nu_2] \hat{f}[\nu_1, \nu_2] \hat{D}(\nu_1/N_1, \nu_2/N_2) \hat{H}(\nu_1/N_1, \nu_2/N_2) \rangle \\ &= \hat{p}[\nu_1, \nu_2] \hat{f}[\nu_1, \nu_2] \langle \hat{H}(\nu_1/N_1, \nu_2/N_2) \hat{D}(\nu_1/N_1, \nu_2/N_2) \rangle.\end{aligned}\quad (5.3)$$

If the restoration filter is chosen to make the fidelity term small, restored images are rejected which would otherwise result in images  $p'$  which differ significantly from  $p$ . The same fidelity metric was used, albeit in an ad-hoc fashion, to generate figure (4.1[d]).

Relative to the c/d/c model in figure 3.1 the CLS restoration metric is

$$J^2 = \alpha S^2 + F^2 \quad (5.4)$$

where  $\alpha$  is a positive, user specified real-valued parameter that weights the smooth-

ness term relative to the fidelity term. The c/d/c model-based CLS restoration filter is derived by choosing  $f$  to minimize  $J^2$ . Because the CLS restoration metric is not defined in an ensemble averaged sense, the c/d/c model-based CLS filter can be designed for a particular digital image  $p$ .

Using Parseval's equation, the expression for  $J^2$  can be written equivalently in the frequency domain as

$$J^2 = \alpha \sum_{\nu_1=-\infty}^{\infty} \sum_{\nu_2=-\infty}^{\infty} |\hat{C}(\nu_1/N_1, \nu_2/N_2) \hat{R}[\nu_1, \nu_2]|^2 + \sum_{\nu_1=0}^{N_1-1} \sum_{\nu_2=0}^{N_2-1} |\hat{p}[\nu_1, \nu_2] - \hat{p}'[\nu_1, \nu_2]|^2. \quad (5.5)$$

In equation (5.5),  $\hat{C}$  denotes the continuous Fourier transform of the high-pass filter convolution kernel  $c$  and is defined analogously to  $\hat{H}$  in equation (3.5).

The smoothness term can be written in terms of the unknown restoration filter coefficients  $\hat{f}[\nu_1, \nu_2]$ . Doing so yields

$$S^2 = \sum_{\nu_1=-\infty}^{\infty} \sum_{\nu_2=-\infty}^{\infty} |\hat{C}(\nu_1/N_1, \nu_2/N_2) \hat{D}(\nu_1/N_1, \nu_2/N_2)|^2 |\hat{f}[\nu_1, \nu_2]|^2 |\hat{p}[\nu_1, \nu_2]|^2. \quad (5.6)$$

The summations in equation (5.6) can be reduced to a finite sum over  $N_1 \times N_2$  frequencies by using lemma 4.1.1. That is, equation (5.6) can be re-written as

$$S^2 = \sum_{\nu_1=0}^{N_1-1} \sum_{\nu_2=0}^{N_2-1} \langle |\hat{C}(\nu_1/N_1, \nu_2/N_2) \hat{D}(\nu_1/N_1, \nu_2/N_2)|^2 \rangle |\hat{f}[\nu_1, \nu_2]|^2 |\hat{p}[\nu_1, \nu_2]|^2. \quad (5.7)$$

Substituting equation (5.3) in the fidelity term yields

$$F^2 = \sum_{\nu_1=0}^{N_1-1} \sum_{\nu_2=0}^{N_2-1} |\hat{p}[\nu_1, \nu_2]|^2 \left| 1 - \hat{f}[\nu_1, \nu_2] \langle \hat{H}(\nu_1/N_1, \nu_2/N_2) \hat{D}(\nu_1/N_1, \nu_2/N_2) \rangle \right|^2. \quad (5.8)$$

Using equations (5.7) and (5.8), equation (5.5) can be expressed as a quadratic polynomial in  $\hat{f}[\nu_1, \nu_2]$  of the form

$$J^2 = \sum_{\nu_1=0}^{N_1-1} \sum_{\nu_2=0}^{N_2-1} \left( 1 - \hat{B}[\nu_1, \nu_2] \hat{f}^*[\nu_1, \nu_2] - \hat{B}^*[\nu_1, \nu_2] \hat{f}[\nu_1, \nu_2] + \hat{A}[\nu_1, \nu_2] |\hat{f}[\nu_1, \nu_2]|^2 \right) |\hat{p}[\nu_1, \nu_2]|^2 \quad (5.9)$$

where

$$\begin{aligned} \hat{B}[\nu_1, \nu_2] &= \left\langle \hat{H}^*(\nu_1/N_1, \nu_2/N_2) \hat{D}^*(\nu_1/N_1, \nu_2/N_2) \right\rangle \\ \hat{A}[\nu_1, \nu_2] &= \alpha \left\langle |\hat{D}(\nu_1/N_1, \nu_2/N_2) \hat{C}(\nu_1/N_1, \nu_2/N_2)|^2 \right\rangle \\ &\quad + \left| \left\langle \hat{H}(\nu_1/N_1, \nu_2/N_2) \hat{D}(\nu_1/N_1, \nu_2/N_2) \right\rangle \right|^2. \end{aligned} \quad (5.10)$$

As in the case of the c/d/c model-based Wiener filter, the minimization of  $J^2$  is accomplished by completing the square as

$$J^2 = J_{\min}^2 + \sum_{\nu_1=0}^{N_1-1} \sum_{\nu_2=0}^{N_2-1} \hat{A}[\nu_1, \nu_2] |\hat{p}[\nu_1, \nu_2]|^2 |\hat{f}[\nu_1, \nu_2] - \hat{f}_c[\nu_1, \nu_2]|^2 \quad (5.11)$$

where the (periodic) c/d/c model-based CLS restoration filter is

$$\hat{f}_c[\nu_1, \nu_2] = \frac{\hat{B}[\nu_1, \nu_2]}{\hat{A}[\nu_1, \nu_2]} \quad (5.12)$$

and

$$J_{\min}^2 = \sum_{\nu_1=0}^{N_1-1} \sum_{\nu_2=0}^{N_2-1} |\hat{p}[\nu_1, \nu_2]|^2 \left[ 1 - |\hat{f}_c[\nu_1, \nu_2]|^2 \hat{A}[\nu_1, \nu_2] \right] \quad (5.13)$$

is the residual error *independent* of  $\hat{f}$ .<sup>2</sup> Each term in the summation in equation (5.11) is non-negative; this is used to prove the following theorem which establishes that the CLS filter in equation (5.12) minimizes  $J^2$ .

---

<sup>2</sup>If  $\hat{A}[\nu_1, \nu_2] = 0$  then, by convention,  $\hat{f}_c[\nu_1, \nu_2] = 0$ .

**Theorem 5.1.1** *If  $\hat{A}[\nu_1, \nu_2] \neq 0$  and  $|\hat{p}[\nu_1, \nu_2]|^2 \neq 0$  for all  $[\nu_1, \nu_2]$  then  $J^2$  achieves its minimum value of  $J_{\min}^2$  if and only if  $\hat{f}[\nu_1, \nu_2] = \hat{f}_c[\nu_1, \nu_2]$  for all  $[\nu_1, \nu_2]$  where  $\hat{f}_c[\nu_1, \nu_2]$  is defined by equation (5.12).*

The d/d model-based CLS restoration filter

$$\hat{f}_c[\nu_1, \nu_2] = \frac{\hat{h}^*[\nu_1, \nu_2]}{|\hat{h}[\nu_1, \nu_2]|^2 + \alpha|\hat{c}[\nu_1, \nu_2]|^2} \quad (5.14)$$

and the c/d/c model-based CLS restoration filter

$$\hat{f}_c[\nu_1, \nu_2] = \frac{\langle \hat{H}^*(\nu_1/N_1, \nu_2/N_2) \hat{D}^*(\nu_1/N_1, \nu_2/N_2) \rangle}{|\langle \hat{H}(\nu_1/N_1, \nu_2/N_2) \hat{D}(\nu_1/N_1, \nu_2/N_2) \rangle|^2 + \alpha|\langle \hat{C}(\nu_1/N_1, \nu_2/N_2) \hat{D}(\nu_1/N_1, \nu_2/N_2) \rangle|^2} \quad (5.15)$$

are not identical. One notable difference is in the presence of the folding operator  $\langle \cdot \rangle$  that is applied to the (aperiodic) Fourier transforms in the numerator and the denominator in equation (5.15); there is no frequency-folding in equation (5.14).

For a particular choice of  $\alpha$  and  $\hat{C}$ , the c/d/c model-based CLS filter reduces to the d/d model-based CLS filter if and only if the reconstruction function is the sinc function in the spatial domain. Exact sinc reconstruction is impossible; in practice, neither physical RTFs nor interpolative RTFs have the ideal low-pass response of the sinc filter. Therefore, the d/d model-based CLS filter does not have the same frequency response as the c/d/c model-based CLS filter. For digital imaging systems the c/d/c model-based CLS filter should be used instead of the d/d model-based CLS filter.

Recall that the derivation of the  $c/d/c$  model-based Wiener filter in chapter 4 assumed that the input scene is stochastic and required two statistical assumptions about the scene and the additive random noise. In particular, that derivation required that the scene's sidebands be uncorrelated and that the random noise be scene-independent. The derivation of the CLS restoration filter does not place any such restrictions on either the scene model or the noise model. From a theoretical standpoint, this makes the  $c/d/c$  model-based CLS restoration filter more general than the  $c/d/c$  model-based Wiener filter. From a practical standpoint, this allows the  $c/d/c$  model-based CLS filter to be used in a broader class of image restoration applications than the  $c/d/c$  model-based Wiener filter including, for example, restoration applications where additive random noise is scene-dependent.

## 5.2 CLS Filter Computation

The CLS restoration filter response is defined in terms of the image acquisition PSF  $h$ , the display reconstruction PSF  $d$ , and two user-specified items — the weighting parameter  $\alpha$  and the high-pass filter  $c$ . Of these,  $h$  and  $d$  are assumed to be known *a priori*; the only “unknowns” in equation (5.15) are  $\alpha$  and  $C$ . This section discusses methods for specifying these two items.

In the context of  $c/d/c$  model-based CLS restoration,  $c$  and  $\alpha$  are used to minimize the enhancement of both random noise and aliased noise. Random noise and aliased noise are generally negligible at low frequencies. Therefore, at low frequen-

cies it is generally safe to allow the CLS restoration filter to invert the blurring caused by image acquisition and image reconstruction. At high frequencies both random noise and aliased noise may not be negligible. If so, the CLS restoration filter must moderate its high-boost action at high frequencies to avoid the type of artifacts illustrated in figure (3.8[a]). To achieve such a restoration filter response  $\hat{C}$  must be a high-pass filter.

There is no universally accepted choice for  $c$  (or  $\hat{C}$ ) — several high-pass filters have been advocated for d/d model-based CLS restoration filters [57].<sup>3</sup> Two common choices for  $\hat{C}$  are

$$\hat{C}(\omega_1, \omega_2) = 4(1 - \cos(2\pi\omega_1))(1 - \cos(2\pi\omega_2)). \quad (5.16)$$

and

$$\hat{C}(\omega_1, \omega_2) = (\omega_1^2 + \omega_2^2)^{k/2}. \quad (5.17)$$

In equation (5.17) the integer parameter  $k$  is called the *order* of  $c$ ; the larger the order, the greater is the high-boost action of this high-pass filter. If desired the order can be implemented as an interactive procedure, allowing the user to select a value that results in the (visually) best restored image.

Given a choice of  $c$ , values for the smoothing parameter  $\alpha$  can be computed in several different ways [58]. The *Chi-Square Choice* technique has been successfully

---

<sup>3</sup>Indeed, as demonstrated by simulation later in this chapter, one attractive feature of the CLS restoration technique is the relative insensitivity of the restored image to the choice of  $c$  (or  $\hat{C}$ ), provided  $\alpha$  is computed by the method described in this section.



used in the context of d/d model-based CLS restorations, provided the standard deviation of the random noise can be accurately estimated [43]. Using this technique, a value of  $\alpha$  is computed by forcing the expected fidelity term  $F^2$  to be equal to the variance of the random noise. That is, the equation

$$F^2(\alpha) = \sigma_e^2 \quad (5.18)$$

is solved for the unknown  $\alpha$  with

$$F^2(\alpha) = \alpha^2 \sum_{\nu_1=0}^{N_1-1} \sum_{\nu_2=0}^{N_2-1} |\hat{p}[\nu_1, \nu_2]|^2 \left| \frac{\langle |\hat{C}(\nu_1/N_1, \nu_2/N_2) \hat{D}(\nu_1/N_1, \nu_2/N_2)|^2 \rangle}{\left| \langle \hat{H}(\nu_1/N_1, \nu_2/N_2) \hat{D}(\nu_1/N_1, \nu_2/N_2) \rangle \right|^2 + \alpha \langle |\hat{C}(\nu_1/N_1, \nu_2/N_2) \hat{D}(\nu_1/N_1, \nu_2/N_2)|^2 \rangle} \right|^2 \quad (5.19)$$

Because  $F^2$  is a *monotone increasing* function of  $\alpha$  with

$$F^2(0) = 0 < \sigma_e^2 < F^2(\infty) = \|p\|^2 \quad (5.20)$$

where

$$\|p\|^2 = \frac{1}{N_1 N_2} \sum_{n_1=0}^{N_1-1} \sum_{n_2=0}^{N_2-1} |p[n_1, n_2]|^2 \quad (5.21)$$

Equation (5.18) can be solved numerically for  $\alpha$ . That is, by starting with  $\alpha = 0$  and incrementing by a fixed value (e.g., 1.0), two values of  $\alpha$ , say  $\alpha_1$  and  $\alpha_2$ , can be found such that

$$F^2(\alpha_1) < \sigma_e^2 < F^2(\alpha_2). \quad (5.22)$$

At this point, bi-section can be applied to find a value of  $\alpha$  for which the relative error  $|F^2(\alpha) - \sigma_e^2|/\sigma_e^2$  is arbitrarily small. The number of iterations required for the

bi-section algorithm to converge is dependent on  $F$ , the choice of  $\alpha_1$ ,  $\alpha_2$ , and the desired accuracy. The typical number of iterations ranges from 10 to 50 for relative errors on the order of  $10^{-6}$ .

An accurate (numerical) solution for  $\alpha$  reflects a balance between too much high-frequency noise and too little sharpening in the reconstructed image. That is, for a given  $c$ , if the value of  $\alpha$  is too small, the CLS restoration filter will amplify high frequencies more than desired, possibly amplifying both random and aliased noise as well. In contrast, if the value of  $\alpha$  is too large the CLS restoration filter will over-correct for noise by making the values of the filter response at higher spatial frequencies lower than actually required, thereby decreasing the high-boost effect of the restoration filter.

In some applications, such as “smart” digital cameras that employ relatively simple in-line digital filtering techniques, it is not possible to recompute the CLS restoration filter values for different scenes. If so, then the CLS restoration filter has to be designed for an ensemble of scenes. This is accomplished by replacing  $|\hat{p}[\nu_1, \nu_2]|^2$  with by  $\hat{\Phi}_p[\nu_1, \nu_2]$  in equation (5.19) to yield a value of  $\alpha$  that is optimum with respect to an ensemble of scenes. Using  $\hat{\Phi}_p[\nu_1, \nu_2]$  in place of  $|\hat{p}[\nu_1, \nu_2]|^2$  requires that ensemble statistics of the digital image  $\hat{\Phi}_p[\nu_1, \nu_2]$  be estimated prior to solving equation (5.18). Estimating  $\hat{\Phi}_p[\nu_1, \nu_2]$  is, in theory, easier than estimating  $\hat{\Phi}_s[\nu_1, \nu_2]$  because there is no need to account for image acquisition blur and noise. That is, if a set of representative digital images are available, then  $\hat{\Phi}_p[\nu_1, \nu_2]$  can be estimated

as the average of their energy spectra.

In the ideal case where there is no random noise (i.e.  $\sigma_e = 0$ ) the optimum value of  $\alpha$  is 0. If so, the c/d/c model-based CLS restoration filter reduces to

$$\hat{f}_c[\nu_1, \nu_2] = \frac{1}{\langle \hat{H}(\nu_1/N_1, \nu_2/N_2) \hat{D}(\nu_1/N_1, \nu_2/N_2) \rangle} \quad (5.23)$$

This dissertation takes equation (5.23) as the definition of the c/d/c model-based *inverse filter*.<sup>4</sup> To do so is intuitive because equation (5.23) is the limiting case of the c/d/c model-based CLS restoration filter as the SNR approaches  $\infty$ , just as the d/d model-based inverse filter, equation (2.11), is the SNR  $\rightarrow \infty$  limiting case of the d/d model-based CLS restoration filter.

### 5.3 Simulated CLS Restorations

To demonstrate the effectiveness of the c/d/c model-based CLS restoration filter, simulated c/d/c model-based CLS restorations are presented in this section. These simulations demonstrate that the c/d/c model-based CLS filter can restore effectively across a range of image acquisition blur, random noise and aliased noise. The simulations also demonstrate that CLS restorations are relatively insensitive to the choice of the high-pass filter  $\hat{C}$  when  $\alpha$  is computed using the technique described in the previous section.

In the first simulation, the results of which are illustrated in figure (5.1), the

---

<sup>4</sup>There is no existing definition of the c/d/c model-based inverse restoration filter in the literature.

processing used to generate the three images in figure (3.5) is repeated with the c/d/c model-based CLS restoration filter. The format of figure (5.1) is identical to that of figure (3.5); the top-left image is the original scene and the remaining three are restored images using PCC reconstruction. To generate the CLS filter in each case, the high-pass filter defined in equation (5.17) is used with  $k = 2$ . The Chi-Square Choice method is used to compute  $\alpha$ .

The SNR for this simulation is 50 ( $\sigma_e = 0.8615$ ); this SNR value denotes a significant amount of random noise. Pairwise comparison of the images in figures (3.5) and (5.1) makes the image quality improvement due to the use of the CLS filter obvious; each of the restored images in figure (5.1) is sharper than the corresponding unrestored image in figure (3.5). Some random and aliased noise enhancement is visible in all three restored images; unlike the inverse filter restorations in chapter 2, however, this noise enhancement is not severe enough to mask image detail. The values of  $\alpha$  for the  $\sigma = 0.75$ ,  $\sigma = 0.5$  and  $\sigma = 0.25$  cases are  $1.1525 \times 10^{-5}$ ,  $7.6293 \times 10^{-6}$  and  $1.1583 \times 10^{-7}$  respectively.

To test the CLS restoration filter under very low SNR conditions, the previous simulation was repeated with a SNR of 10 ( $\sigma_e = 4.3075$ ). In spite of the 5-fold decrease in the SNR, the effects of random noise were not apparent in the reconstructed images; they are virtually identical to the corresponding images in figure (3.5) and therefore not shown. The CLS restorations for the SNR = 10 case are illustrated in figure (5.2[b]–[d]); they are not identical to the restorations illustrated in fig-

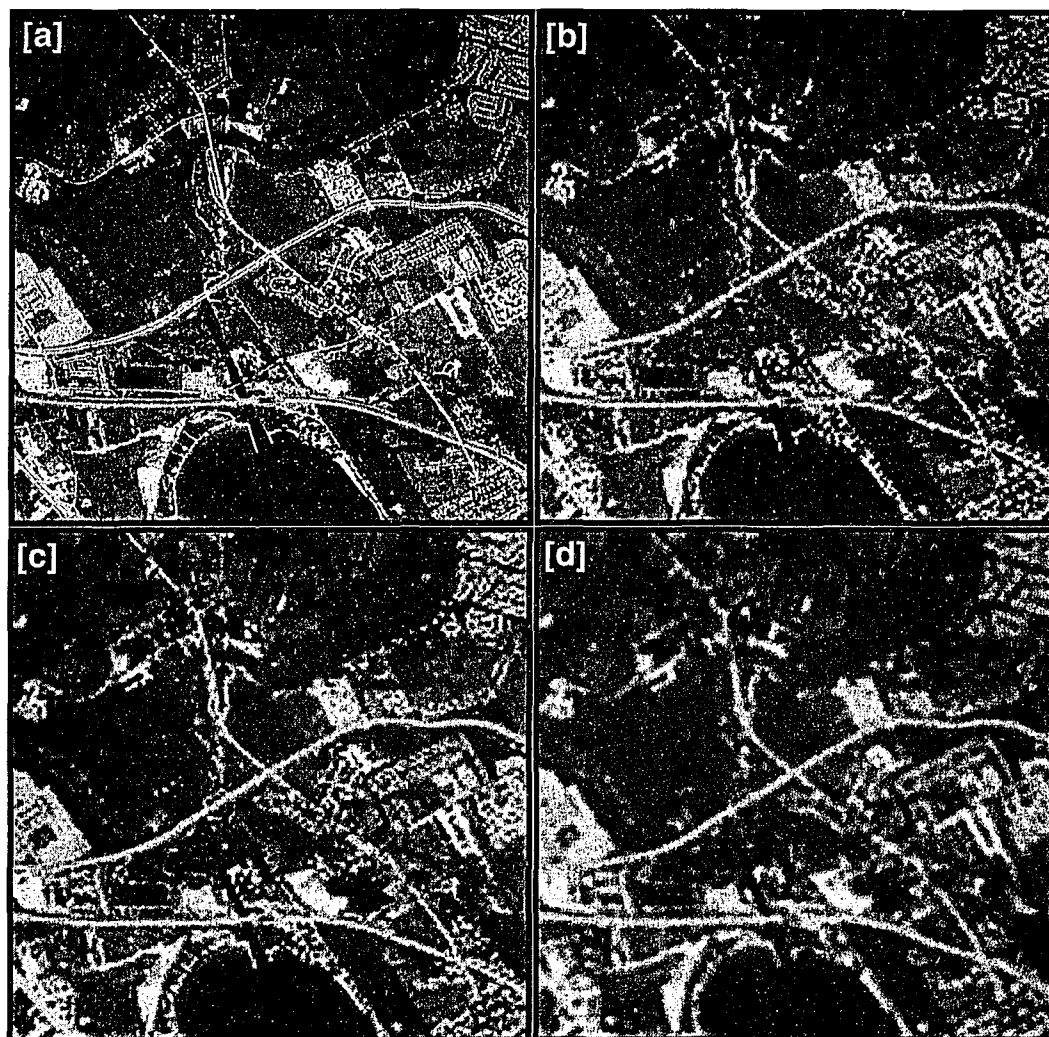


Figure 5.1:  $C/d/c$  model-based CLS restorations with  $\text{SNR} = 50$ .

ure (5.1). In particular, each of the restorations for the  $\text{SNR} = 50$  case is sharper than the corresponding restoration for the  $\text{SNR} = 10$  case. This observation is consistent with the expectation that the c/d/c model-based CLS filter moderates its high-boost response in accordance with the amount of additive random noise present in the image.

Figure (5.3) illustrates 1-D profiles of the CLS filter's frequency response for the two different SNRs.<sup>5</sup> The solid and dashed curves correspond to the  $\text{SNR} = 50$  and the  $\text{SNR} = 10$  case, respectively. In each of the three OTF cases, the two CLS filter responses are virtually identical at low frequencies; at high frequencies, however, the restoration filter response for the  $\text{SNR} = 10$  case is smaller than that for the  $\text{SNR} = 50$  case. This moderation is explained by the larger  $\alpha$  values for the  $\text{SNR} = 10$  case compared to the  $\text{SNR} = 50$  case; for the  $\sigma = 0.75$ ,  $\sigma = 0.5$  and  $\sigma = 0.25$  cases the corresponding  $\alpha$  values for the  $\text{SNR} = 10$  case are  $6.1035 \times 10^{-5}$ ,  $1.2207 \times 10^{-4}$  and  $2.4414 \times 10^{-4}$  respectively.

To demonstrate that the c/d/c model-based CLS filter modifies its high-boost response in response to aliased noise in the same manner as it does for random noise, another simulation is presented. In this simulation, the aerial scene is blurred with the Gaussian OTF defined in equation (3.15), then sampled onto different-sized pixel grids. PCC reconstruction is used to generate the reconstructed output images. Figure (5.4) is a 4-panel composite illustrating the unrestored output images.

---

<sup>5</sup>As in figure (2.8), the restoration filter's discrete frequency response is expressed in db and is plotted as a continuous curve.

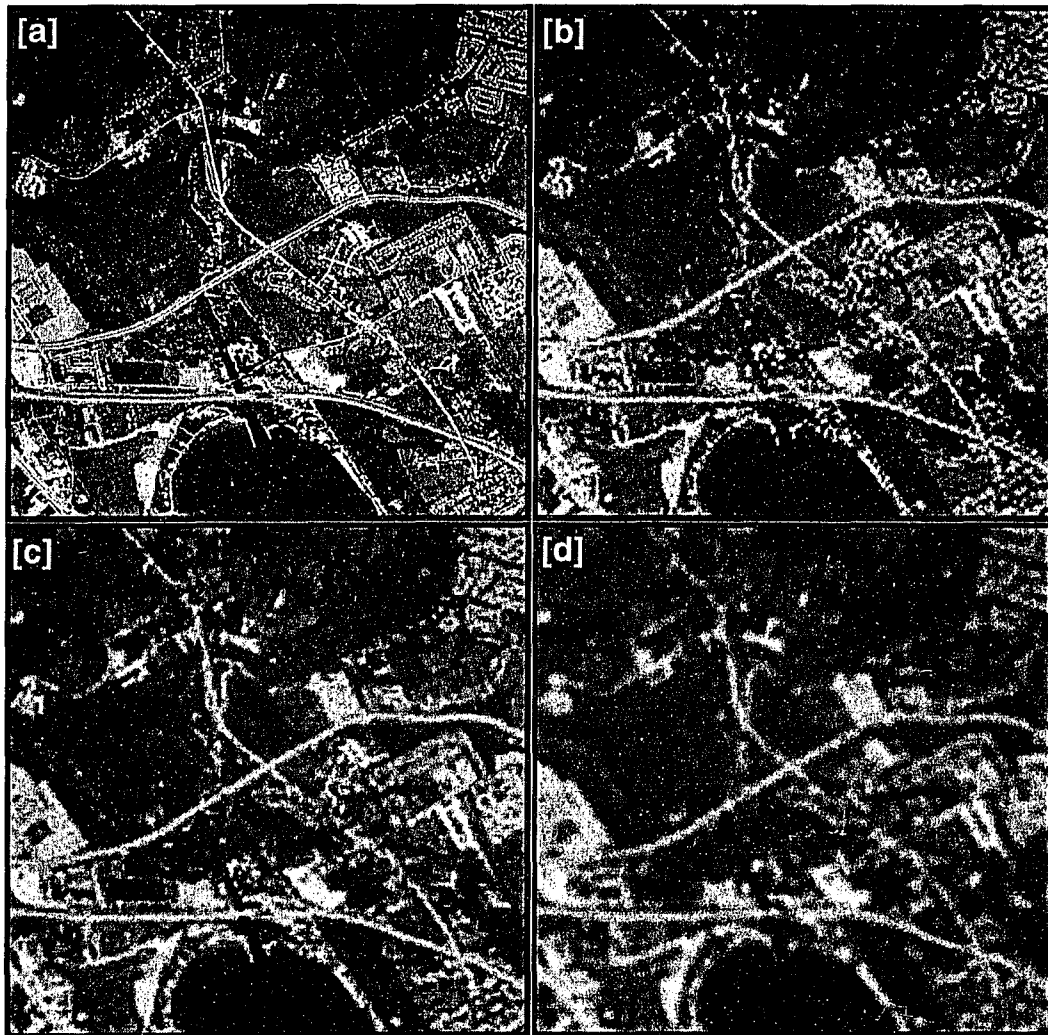


Figure 5.2: C/d/c model-based CLS restorations with  $\text{SNR} = 10$ .

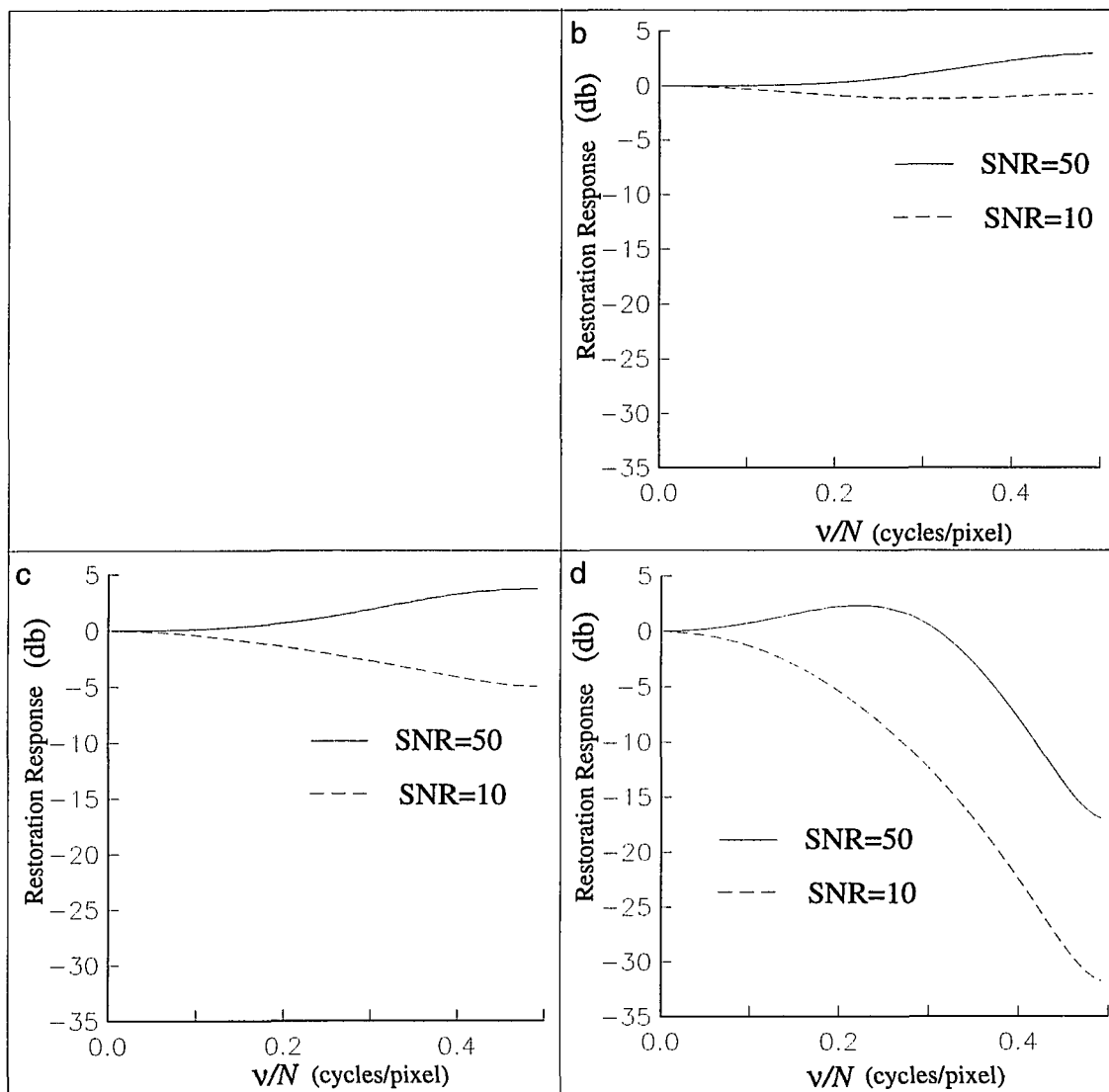


Figure 5.3: C/d/c model-based CLS filter responses for different SNRs.



Figure (5.4[a]) is the original  $512 \times 512$  aerial scene; figures (5.4[b]–[d]) are the un-restored outputs obtained by using a  $256 \times 256$ , a  $128 \times 128$  and a  $64 \times 64$  pixel grid respectively. In figure (5.4[b]) the OTF scale parameter is  $\sigma = 0.25$  (cycles/pixel); in figures (5.4[c]) and (5.4[d]) the parameter value is 0.5 and 1.0 respectively. Note that these values of  $\sigma$  generate identical pre-sampled images  $g = s \otimes h$ . Random noise with  $\sigma_e = 0.0236$  is added to each of the three sampled images; this results in an SNR of 2000 in each case.<sup>6</sup> Consistent with the characterization of aliasing as scene-dependent noise, the un-restored output images exhibit artifacts; the artifacting become more severe as the sampling density is decreased. This artifacting can be quantified by defining the aliased noise variance as

$$\sigma_a^2 = \sum_{\nu_1=1}^{N_1-1} \sum_{\nu_2=1}^{N_2-1} |\hat{a}[\nu_1, \nu_2]|^2 \quad (5.24)$$

Using this definition, figure (5.4[b]), which exhibits the least amount of artifacting, corresponds to the lowest  $\sigma_a^2 = 0.0208$  while figure (5.4[d]), which exhibits the greatest amount of artifacting, corresponds to the highest  $\sigma_a^2 = 0.1121$ .

Figure (5.5) illustrates the c/d/c model-based CLS restorations of the corresponding images in figure (5.4). To generate the CLS restoration filter the high-pass filter defined in equation (5.18) is used with  $k = 2$ . The Chi-Square Choice method is used to compute  $\alpha$ . For the case where the level of aliased noise is the

---

<sup>6</sup>A very high SNR is purposely chosen to minimize the effects of random noise since the objective of this simulation is to demonstrate the ability of the c/d/c model-based CLS restoration filter to account for aliased noise.

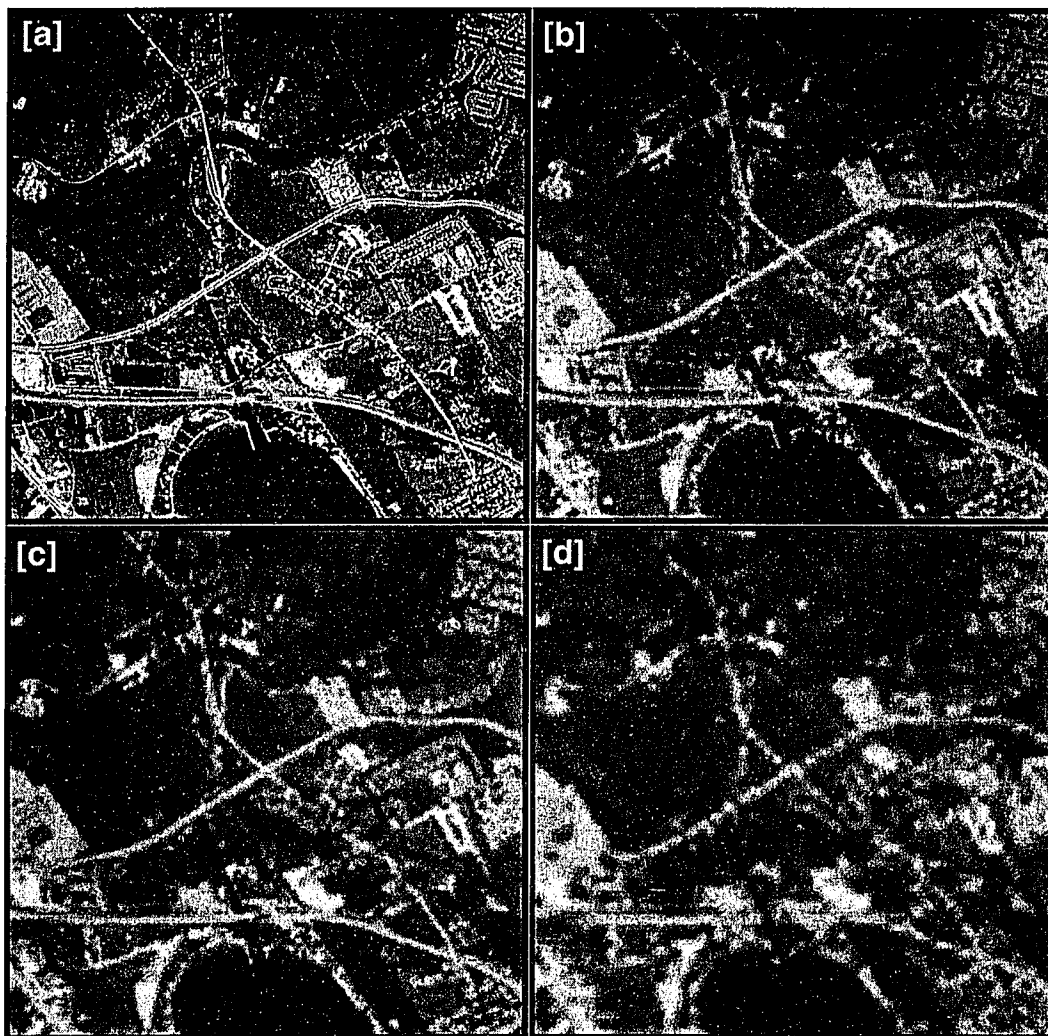


Figure 5.4: PCC reconstruction of aerial scene with different sampling grids.

lowest, figure (5.5[b]), the CLS restoration is much sharper than the corresponding unrestored image, figure (5.4[b]), and virtually indistinguishable from the original. In this case, the CLS filter removes virtually all the blurring caused by the OTF and the RTF. As the level of aliased noise increases, however, to avoid enhancing aliased noise the CLS filter does not sharpen as much. This is most easily seen in figure (5.6) that illustrates the different CLS filter responses for the three different sampling grids.

In all the simulated CLS restorations presented so far, equation (5.17) with  $k = 2$  has been used for the high-pass filter  $\hat{C}$  to synthesize the CLS filter. In the next simulation three different user-defined high-pass filters are used to restore the same digital image of the aerial scene with the c/d/c model-based CLS restoration filter. Figure (5.7) is a 4-panel composite illustrating the scene and the three restored images. The three CLS restoration filters are synthesized by using equation (5.17) for  $\hat{C}(\omega_1, \omega_2)$  with  $k = 2, 4$  and  $6$ . Figure (5.7[a]) is the original aerial scene and the remaining three restored images ([b],[c] and [d]) are CLS restorations with  $k = 2, 4$  and  $6$ . Figure (5.8[a]) illustrates the high-pass filter responses for the three values of  $k$ . In all three cases a Gaussian OTF with  $\sigma = 0.5$  is used, the SNR is 50, and PCC reconstruction is used. As evident from figures (5.7[b]–[d]), the three restored images are visually similar although a different high-pass filter is used in each case to synthesize the CLS filter. The  $\alpha$  values corresponding to the  $k = 2, 4$  and  $6$  are  $7.6293 \times 10^{-6}$ ,  $3.7252 \times 10^{-9}$  and  $9.0943 \times 10^{-13}$ , respectively. The virtually

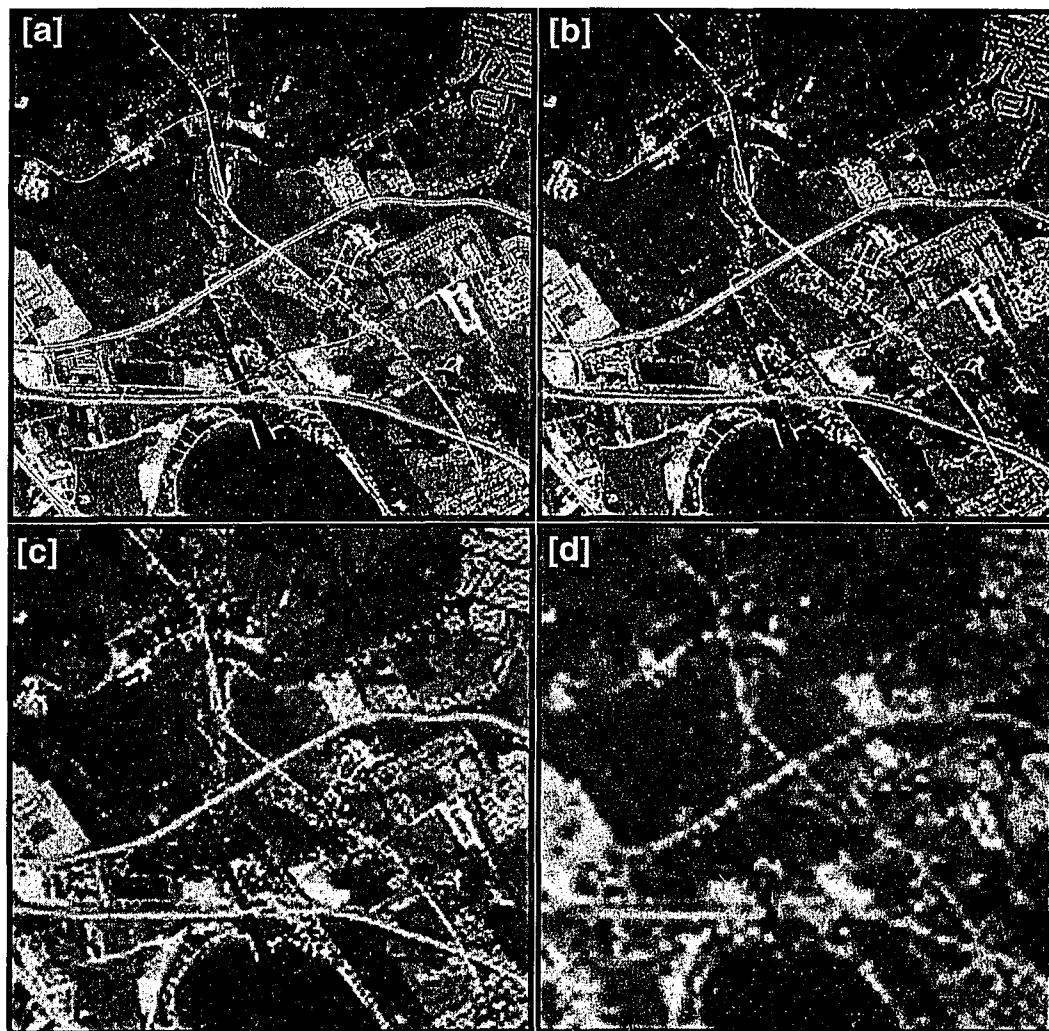


Figure 5.5: C/d/c model-based CLS restorations with different sampling grids.

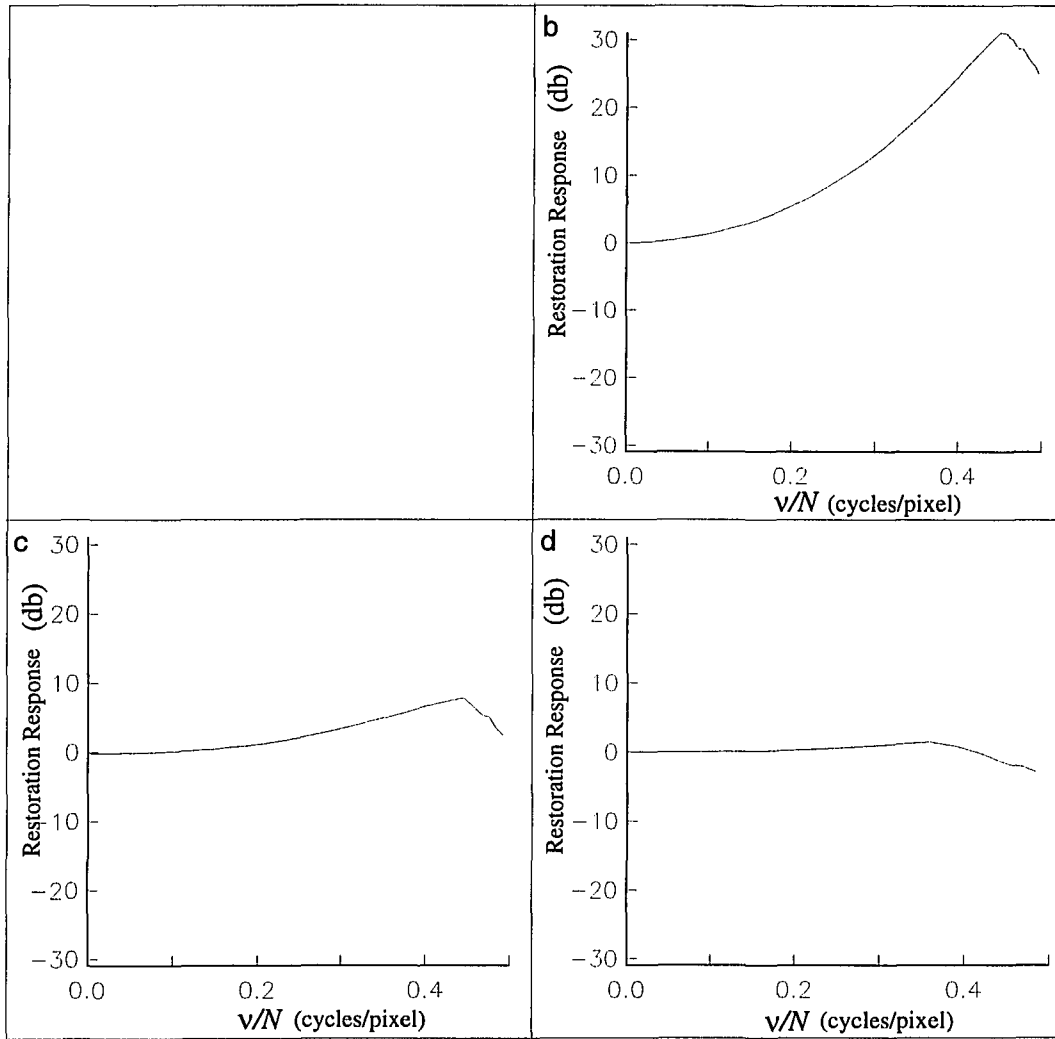


Figure 5.6: C/d/c model-based CLS filter responses with different sampling grids.

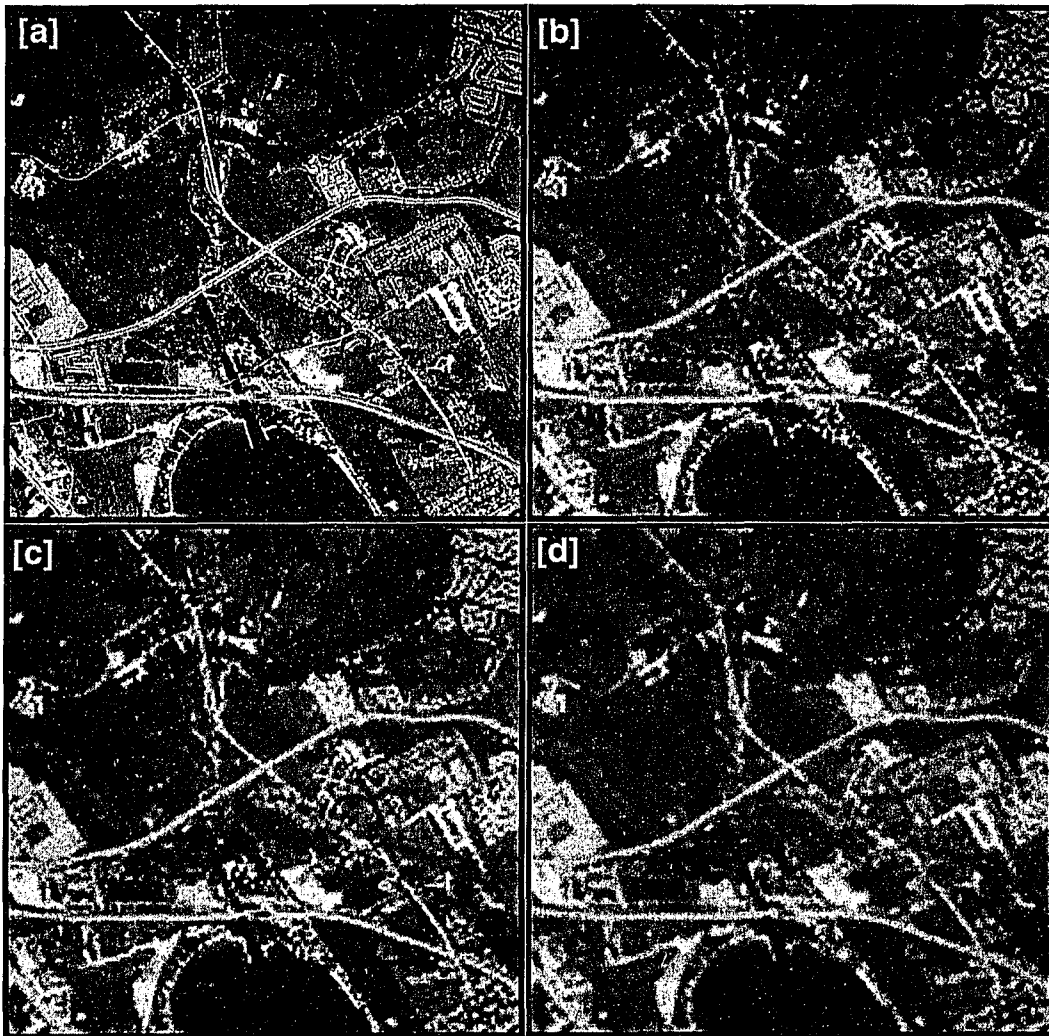


Figure 5.7: C/d/c model-based CLS restorations corresponding to different user-supplied high-pass filters.

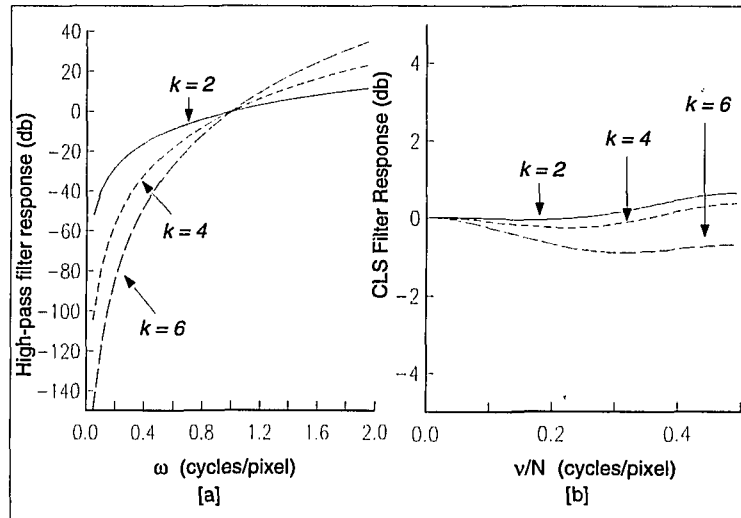


Figure 5.8: C/d/c model-based CLS filter responses with different user-supplied high-pass filters.

identical restorations are explained by these  $\alpha$  values that decrease in magnitude as  $k$  increases. That is, as the high-pass response of the filter  $\hat{C}$  is increased,  $\alpha$  becomes smaller to compensate. Figure (5.8[b]) illustrates the three CLS filter responses corresponding to  $k = 2, 4$  and  $6$ . This simulation demonstrates how the Chi-Square Choice method adjusts  $\alpha$  correctly in an attempt to maintain the fidelity of the restored image when different user-supplied high-pass filters are used.

The simulations presented in this section demonstrate that the c/d/c model-based CLS restoration filter is effective across a range of imaging conditions. The c/d/c model-based CLS filter is able to de-blur image acquisition blur and image reconstruction blur effectively when random and aliased noise are negligible. When random noise and/or aliased noise are not negligible the CLS filter correctly mod-

erates its high-boost response to minimize noise enhancement. Moreover, the CLS filter has a built-in “self-correcting” mechanism that makes it relatively insensitive (within limits) to user-input. Chapter 6 presents a technique that allows the c/d/c model-based restoration filter to be implemented as a small-kernel convolution in the spatial domain. Chapter 7 presents c/d/c model-based CLS restorations of thermal images using the small-kernel CLS restoration filter.



# CHAPTER VI

## SPATIAL DOMAIN CLS RESTORATION

Because the  $c/d/c$  model-based CLS restoration filter is derived in the frequency domain, it is natural to implement this filter in the frequency domain as well. Although the frequency domain provides valuable insight into the filter design process, for some applications it is not the correct domain for implementation. Recent research by Reichenbach et al. [47] has demonstrated that the  $c/d/c$  model-based Wiener filter can be implemented as a small-kernel convolution in the spatial domain. This chapter builds on their research to show that the  $c/d/c$  model-based CLS restoration filter presented in chapter 5 can be implemented effectively and efficiently in a similar fashion.

### 6.1 Spatial Domain Restoration

As demonstrated in chapter 5, the  $c/d/c$  model-based CLS restoration filter is designed in the frequency domain thereby suggesting the frequency domain as a natural domain for the implementation of the filter. A frequency domain implementation of the CLS restoration filter, equation (5.16), using equation (3.11) requires that the  $N_1 \times N_2$  DFT array  $\hat{p}$  be computed. Furthermore, the restored image  $q$  must be recovered from its  $N_1 \times N_2$  DFT array  $\hat{q}$  by computing an inverse discrete Fourier

transform. Even if FFTs are used to compute the forward and inverse DFT arrays, a frequency domain implementation of the CLS restoration filter requires significant processing power and computer memory to store the complex-valued DFT coefficients. For those applications that are subject to stringent timing constraints and cannot afford expensive hardware, a frequency domain implementation of the c/d/c model-based CLS filter is of limited practical utility.

As an alternative to a frequency domain implementation, the c/d/c model-based CLS restoration filter can be implemented in the spatial domain by convolution. That is, the restored image  $q = p \oplus f$  can be computed as

$$q[n_1, n_2] = \frac{1}{N_1 N_2} \sum_{n'_1=0}^{N_1-1} \sum_{n'_2=0}^{N_2-1} f[n'_1, n'_2] p[n_1 - n'_1, n_2 - n'_2]. \quad (6.1)$$

If the unconstrained  $N_1 \times N_2$  kernel array  $f$  is not “small”, then equation (6.1) requires  $N_1^2 N_2^2$  (real) multiplications and as many additions.

If the periodic CLS restoration kernel is small — that is, if it has only a few non-zero values per period — the number of multiplications and additions can be reduced significantly. Convolution of a  $N_1 \times N_2$  digital image with a small  $K_1 \times K_2$  CLS restoration kernel requires  $K_1 N_1 K_2 N_2$  multiplications and additions; if  $K_1 \ll N_1$  and  $K_2 \ll N_2$  then this complexity reduction is significant. If, for example, a small  $5 \times 5$  CLS restoration kernel is used, a spatial domain implementation is much more efficient than a frequency domain implementation. Moreover, a spatial domain implementation that uses a small CLS restoration kernel is also amenable to direct hardware implementation.

The small-kernel approach is based on the observation that, in general, each restored image pixel value is principally determined by the values of pixels in a relatively small neighborhood of the corresponding image pixel; the greater the distance of an image pixel from the pixel being restored, the smaller its contribution to the restored value. Thus, it is reasonable to expect that if only the most significant values of the restoration filter are used in the convolution (by setting the insignificant restoration kernel values to zero), the quality of the restored image should not be significantly affected. If the adverse effects of using a small-kernel are indeed negligible, then using a small-kernel is the most efficient way to implement the  $c/d/c$  model-based CLS restoration filter.

One method of generating a small periodic restoration kernel is to truncate the unconstrained kernels by using a periodic *window function* centered at  $[0, 0]$ . If this window function is a periodic 2-D rectangle function then the restoration filter values are left *unchanged* within the window and set to zero outside (modulo the period). Because the sharp cut-off of such a window introduces undesirable ringing in the restoration filter's transfer function  $\hat{f}[\nu_1, \nu_2]$ , alternative windowing functions have been used [48]–[50]. Other related techniques have also been advocated in the literature [51][52].

All these windowing techniques are *ad hoc* in the sense that the restoration filter is designed, in the frequency domain, under the assumption that it will not be modified. There is no coordination between the restoration filter design process

and the filter implementation process. A more rigorous technique is required which will account for the processing constraints in the design of the restoration kernel to avoid the problem of designing one filter and applying a different one. In section 6.2, such a rigorous technique is presented in the context of the c/d/c model-based CLS filter. This technique was originally proposed by Reichenbach et al. [47] in the context of the c/d/c model-based Wiener filter.

## 6.2 Small CLS Restoration Kernels

A small c/d/c model-based CLS restoration kernel is defined by specifying a non-empty spatial constraint set  $\theta$  of pixels for which the restoration kernel element can be non-zero. All elements that are *not* in this set are set to zero. Therefore, in the spatial domain the (periodic) CLS restoration kernel is constrained by the property

$$f[n_1, n_2] = 0 \quad \text{if } [n_1 \bmod N_1, n_2 \bmod N_2] \notin \theta. \quad (6.2)$$

In practice, one virtually always chooses the constraint set  $\theta$  to produce an origin-centered  $(2t_1 + 1) \times (2t_2 + 1)$  CLS restoration kernel with typical values of  $t_1, t_2$  in the range 1, 2, 3.<sup>1</sup> The resultant small-kernel CLS restoration kernel is applied as

$$q[n_1, n_2] = \frac{1}{N_1 N_2} \sum_{n'_1=-t_1}^{t_1} \sum_{n'_2=-t_2}^{t_2} f[n'_1, n'_2] p[n_1 - n'_1, n_2 - n'_2]. \quad (6.3)$$

The spatial constraint set  $\theta$  is application-dependent and represents a trade-off between restoration accuracy (since the constrained kernel does not have the same

---

<sup>1</sup>The technique presented in this section does not require that the spatial constraint set have this special structure; the technique is valid for any constraint set.

frequency response as the unconstrained kernel) and computational complexity. To minimize the effect of the spatial constraint on the quality of the restored image,  $\theta$  should include all the significant elements of the unconstrained CLS restoration kernel  $f$ . As the cardinality of the constraint set  $|\theta|$  is increased, however, so does the amount of computation required to implement the restoration filter. There is some evidence suggesting that for most cases restoration kernels larger than  $7 \times 7$  do not significantly improve the quality of the restored image [47].

The DFT coefficients of the spatially constrained CLS restoration filter are defined as

$$\hat{f}_s[\nu_1, \nu_2] = \frac{1}{N_1 N_2} \sum_{[n_1, n_2] \in \theta} f[n_1, n_2] W_1[n_1, \nu_1] W_2[n_2, \nu_2] \quad (6.4)$$

where  $W_1, W_2$  are the complex-valued  $N_1 \times N_1, N_2 \times N_2$  Fourier matrices defined as

$$W_1[n, \nu] = \exp(-i2\pi n\nu/N_1) \quad W_2[n, \nu] = \exp(-i2\pi n\nu/N_2). \quad (6.5)$$

To compute the non-zero c/d/c model-based CLS restoration kernel elements, equation (5.9) is re-written in terms of the constrained kernel. Doing so yields

$$\begin{aligned}
J^2 = & \sum_{\nu_1=0}^{N_1-1} \sum_{\nu_2=0}^{N_2-1} \left( |\hat{p}[\nu_1, \nu_2]|^2 \right. \\
& - \hat{B}[\nu_1, \nu_2] \left( \frac{1}{N_1 N_2} \sum_{[n_1, n_2] \in \theta} f_s^*[n_1, n_2] W_1^*[n_1, \nu_1] W_2^*[n_2, \nu_2] \right) \\
& - \hat{B}^*[\nu_1, \nu_2] \left( \frac{1}{N_1 N_2} \sum_{[n_1, n_2] \in \theta} f_s[n_1, n_2] W_1[n_1, \nu_1] W_2[n_2, \nu_2] \right) \\
& \left. + \hat{A}[\nu_1, \nu_2] \left| \frac{1}{N_1 N_2} \sum_{[n_1, n_2] \in \theta} f_s[n_1, n_2] W_1[n_1, \nu_1] W_2[n_2, \nu_2] \right|^2 \right)
\end{aligned} \tag{6.6}$$

where

$$\begin{aligned}
\hat{B}[\nu_1, \nu_2] &= |\hat{p}[\nu_1, \nu_2]|^2 \left\langle \hat{H}^*(\nu_1/N_1, \nu_2/N_2) \hat{D}^*(\nu_1/N_1, \nu_2/N_2) \right\rangle \\
\hat{A}[\nu_1, \nu_2] &= |\hat{p}[\nu_1, \nu_2]|^2 \left( \alpha \left\langle |\hat{D}(\nu_1/N_1, \nu_2/N_2) \hat{C}(\nu_1/N_1, \nu_2/N_2)|^2 \right\rangle \right. \\
&\quad \left. + \left| \left\langle \hat{H}(\nu_1/N_1, \nu_2/N_2) \hat{D}(\nu_1/N_1, \nu_2/N_2) \right\rangle \right|^2 \right).
\end{aligned} \tag{6.7}$$

Equation (6.6) can be written as

$$\begin{aligned}
J^2 = & \sum_{\nu_1=0}^{N_1-1} \sum_{\nu_2=0}^{N_2-1} |\hat{p}[\nu_1, \nu_2]|^2 \\
& - \frac{1}{N_1 N_2} \sum_{[n_1, n_2] \in \theta} f_s^*[n_1, n_2] \sum_{\nu_1=0}^{N_1-1} \sum_{\nu_2=0}^{N_2-1} \hat{B}[\nu_1, \nu_2] W_1^*[n_1, \nu_1] W_2^*[n_2, \nu_2] \\
& - \frac{1}{N_1 N_2} \sum_{[n_1, n_2] \in \theta} f_s[n_1, n_2] \sum_{\nu_1=0}^{N_1-1} \sum_{\nu_2=0}^{N_2-1} \hat{B}^*[\nu_1, \nu_2] W_1[n_1, \nu_1] W_2[n_2, \nu_2] \\
& + \frac{1}{N_1^2 N_2^2} \sum_{[n_1, n_2] \in \theta} \sum_{[n'_1, n'_2] \in \theta} f_s^*[n_1, n_2] f_s^*[n'_1, n'_2] \\
& \quad \sum_{\nu_1=0}^{N_1-1} \sum_{\nu_2=0}^{N_2-1} \hat{A}[\nu_1, \nu_2] W_1[n_1 - n'_1, \nu_1] W_2[n_2 - n'_2, \nu_2]
\end{aligned}$$

which simplifies to

$$\begin{aligned}
J^2 = & \sum_{\nu_1=0}^{N_1-1} \sum_{\nu_2=0}^{N_2-1} |\hat{p}[\nu_1, \nu_2]|^2 - \frac{1}{N_1 N_2} \sum_{[n_1, n_2] \in \theta} f_s^*[n_1, n_2] b[n_1, n_2] \\
& - \frac{1}{N_1 N_2} \sum_{[n_1, n_2] \in \theta} f_s[n_1, n_2] b^*[n_1, n_2] \\
& + \frac{1}{N_1^2 N_2^2} \sum_{[n_1, n_2] \in \theta} \sum_{[n'_1, n'_2] \in \theta} f_s^*[n_1, n_2] f_s^*[n'_1, n'_2] a[n_1 - n'_1, n_2 - n'_2]
\end{aligned} \tag{6.8}$$

where  $a, b$  are the  $N_1 \times N_2$  inverse DFT arrays corresponding to  $\hat{A}, \hat{B}$  defined in equation (6.7).

Minimizing  $J^2$  with respect to the elements of the constrained restoration kernel yields [47]

$$\frac{1}{N_1 N_2} \sum_{[n'_1, n'_2] \in \theta} f[n'_1, n'_2] a[n_1 - n'_1, n_2 - n'_2] = b[n_1, n_2] \quad [n_1, n_2] \in \theta. \tag{6.9}$$

Equation (6.9) is a linear system of equations with  $|\theta|$  unknowns (the non-zero values of the CLS restoration kernel) and  $|\theta|$  equations. Solving this system of linear equations yields the spatially constrained CLS kernel. That is, this equation can be written in matrix form as

$$\mathbf{A}_\theta \mathbf{f}_s = \mathbf{b}_\theta \tag{6.10}$$

where  $\mathbf{A}_\theta$  is the  $|\theta| \times |\theta|$  submatrix formed by including only those rows and columns of the  $N_1 \times N_2$  array  $a$  that appear in the constraint set. Both  $\mathbf{f}_s$  and  $\mathbf{b}_\theta$  are  $|\theta| \times 1$  vectors; the elements of  $\mathbf{f}_s$  are the (unknown) small CLS kernel elements in lexicographic order and  $\mathbf{b}_\theta$  contains the elements of the array  $b$  that are in the constraint set  $\theta$ , in the same lexicographic order.

In theory, the system of linear equations defined in equation (6.9) will always have unique solutions for the  $|\theta|$  constrained CLS kernel elements as long as  $\hat{A}[\nu_1, \nu_2] \neq 0$  for all  $[\nu_1, \nu_2]$ .<sup>2</sup> Assuming that a unique solution for equation (6.9) exists, if  $|\theta| = N_1 N_2$  then the  $N_1 \times N_2$  CLS restoration kernel obtained by solving equation (6.10) is identical to the  $N_1 \times N_2$  array obtained by computing the inverse DFT of  $\hat{f}_c$  defined in theorem 5.1.1. That is, if no constraints are imposed on the CLS restoration kernel support, then a spatial domain implementation and a frequency domain implementation of the c/d/c model-based CLS restoration filter yield identical results. This limiting property is of little practical interest but can serve as a consistency check for an implementation of the small-kernel generation technique.

### 6.3 Simulated Small-Kernel CLS Restorations

In this section simulation is used to demonstrate that the small-kernel CLS restoration filter produces restorations that are virtually indistinguishable from those produced by the spatially unconstrained CLS filter. In figure (6.1) the spatially unconstrained CLS restoration in figure (5.1[c]) is compared to restorations obtained by using a  $7 \times 7$ , a  $5 \times 5$  and a  $3 \times 3$  small CLS restoration kernel. Figure (6.1[a]) is the spatially unconstrained restoration (identical to figure 5.1[c]); figures (6.1[b]–

---

<sup>2</sup>A mathematical justification for this statement is presented in the context of the c/d/c model-based Wiener filter in [47]. The justification in the context of the c/d/c model-based CLS restoration is the same and, therefore, not repeated here.



[d]), correspond to the  $7 \times 7$ ,  $5 \times 5$  and  $3 \times 3$  small-kernel CLS restorations respectively. The three small restoration kernels are:<sup>3</sup>

$$\begin{array}{ccc} +0.0158 & -0.4068 & +0.0158 \\ -0.4068 & +2.5642 & -0.4068 \\ +0.0158 & -0.4068 & +0.0158 \end{array}$$

$$\begin{array}{ccccc} -0.0092 & +0.0158 & +0.0785 & +0.0158 & -0.0092 \\ +0.0158 & -0.0679 & -0.3307 & -0.0679 & +0.0158 \\ +0.0785 & -0.3307 & +1.9464 & -0.3307 & +0.0785 \\ +0.0158 & -0.0679 & -0.3307 & -0.0679 & +0.0158 \\ -0.0092 & +0.0158 & +0.0785 & +0.0158 & -0.0092 \end{array}$$

$$\begin{array}{cccccc} -0.0015 & +0.0053 & -0.0012 & -0.0010 & -0.0012 & +0.0053 & -0.0015 \\ +0.0053 & -0.0136 & +0.0232 & +0.0893 & +0.0232 & -0.0136 & +0.0053 \\ -0.0012 & +0.0232 & -0.0012 & -0.3567 & -0.0012 & +0.0232 & -0.0012 \\ -0.0010 & +0.0893 & -0.3567 & +2.0958 & -0.3567 & +0.0893 & -0.0010 \\ -0.0012 & +0.0232 & -0.0012 & -0.3567 & -0.0012 & +0.0232 & -0.0012 \\ +0.0053 & -0.0136 & +0.0232 & +0.0893 & +0.0232 & -0.0136 & +0.0053 \\ -0.0015 & +0.0053 & -0.0012 & -0.0010 & -0.0012 & +0.0053 & -0.0015 \end{array}$$

The  $7 \times 7$  center of the unconstrained kernel is

---

<sup>3</sup>The common multiplicative constant  $N_1 N_2 / w$  where  $w$  is the sum of the kernel elements is not shown.

-0.0016	+0.0055	-0.0013	-0.0012	-0.0013	+0.0055	-0.0016
+0.0055	-0.0140	+0.0246	+0.0911	+0.0246	-0.0140	+0.0055
-0.0013	+0.0246	-0.0019	-0.3712	-0.0019	+0.0246	-0.0013
-0.0012	+0.0911	-0.3712	+2.9158	-0.3712	+0.0911	-0.0012
-0.0013	+0.0246	-0.0019	-0.3712	-0.0019	+0.0246	-0.0013
+0.0055	-0.0140	+0.0246	+0.0911	+0.0246	-0.0140	+0.0055
-0.0016	+0.0055	-0.0013	-0.0012	-0.0013	+0.0055	-0.0016

The small CLS restoration kernel values are different from the corresponding unconstrained kernel values. In general, the difference between the small kernel values and the unconstrained values diminishes as the kernel size is increased.

By comparing the small-kernel restorations with the spatially unconstrained restoration in figure (6.1) it becomes clear that using small CLS restoration kernels does not significantly change the appearance of the restored image. The MSD between the unconstrained CLS kernel restoration and each of the small CLS kernel restorations is 1.00, 3.38 and 5.43 for the  $7 \times 7$ , the  $5 \times 5$  and the  $3 \times 3$  kernel respectively. The MSD are small compared to the contrast of the original scene and explain why no significant differences can be seen in the images presented in figure (6.1). Consistent with intuition and the restoration filter kernels presented, the MSD decreases as the kernel size is increased.

Three difference images presented are presented in figure (6.2). These zero-mean difference images have had their mean value shifted to 128.0 and have been iden-

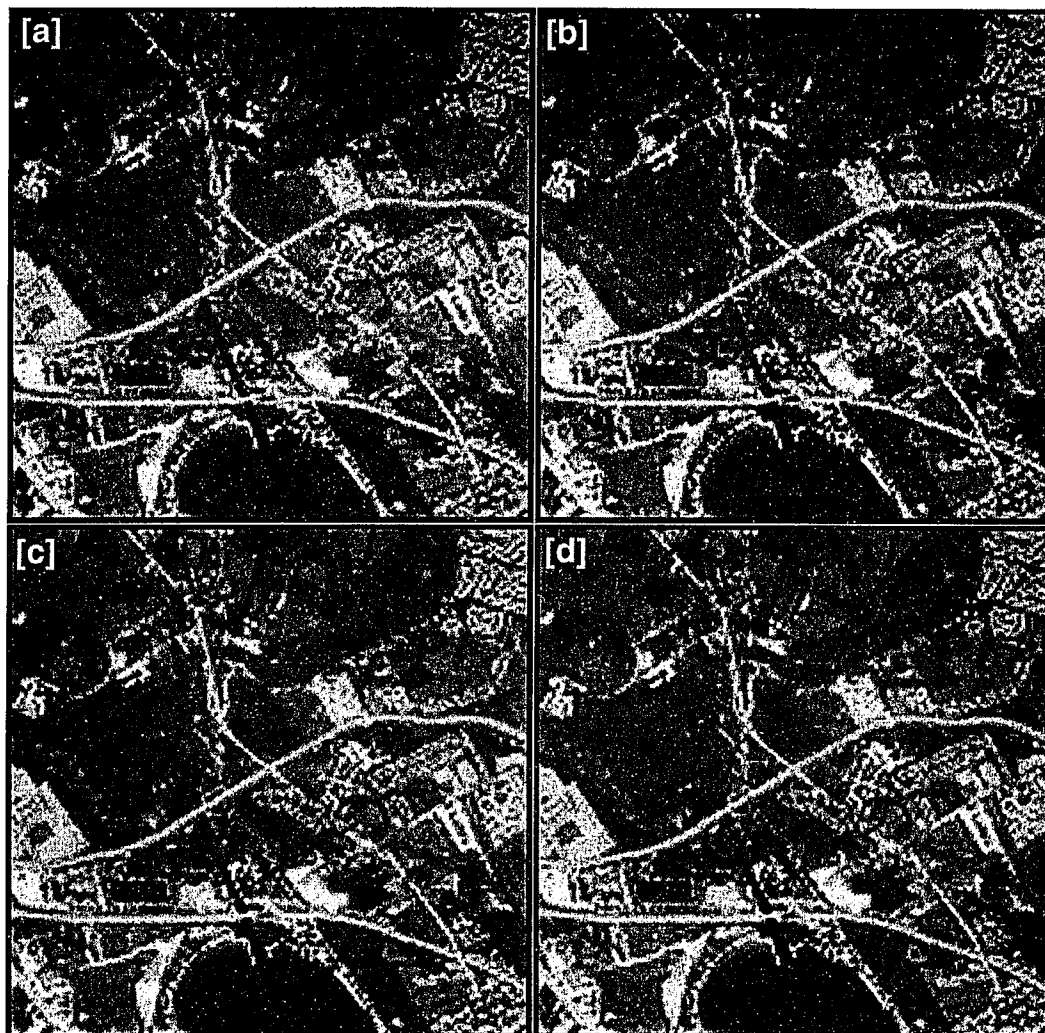


Figure 6.1: Spatially unconstrained and three small-kernel CLS restorations.

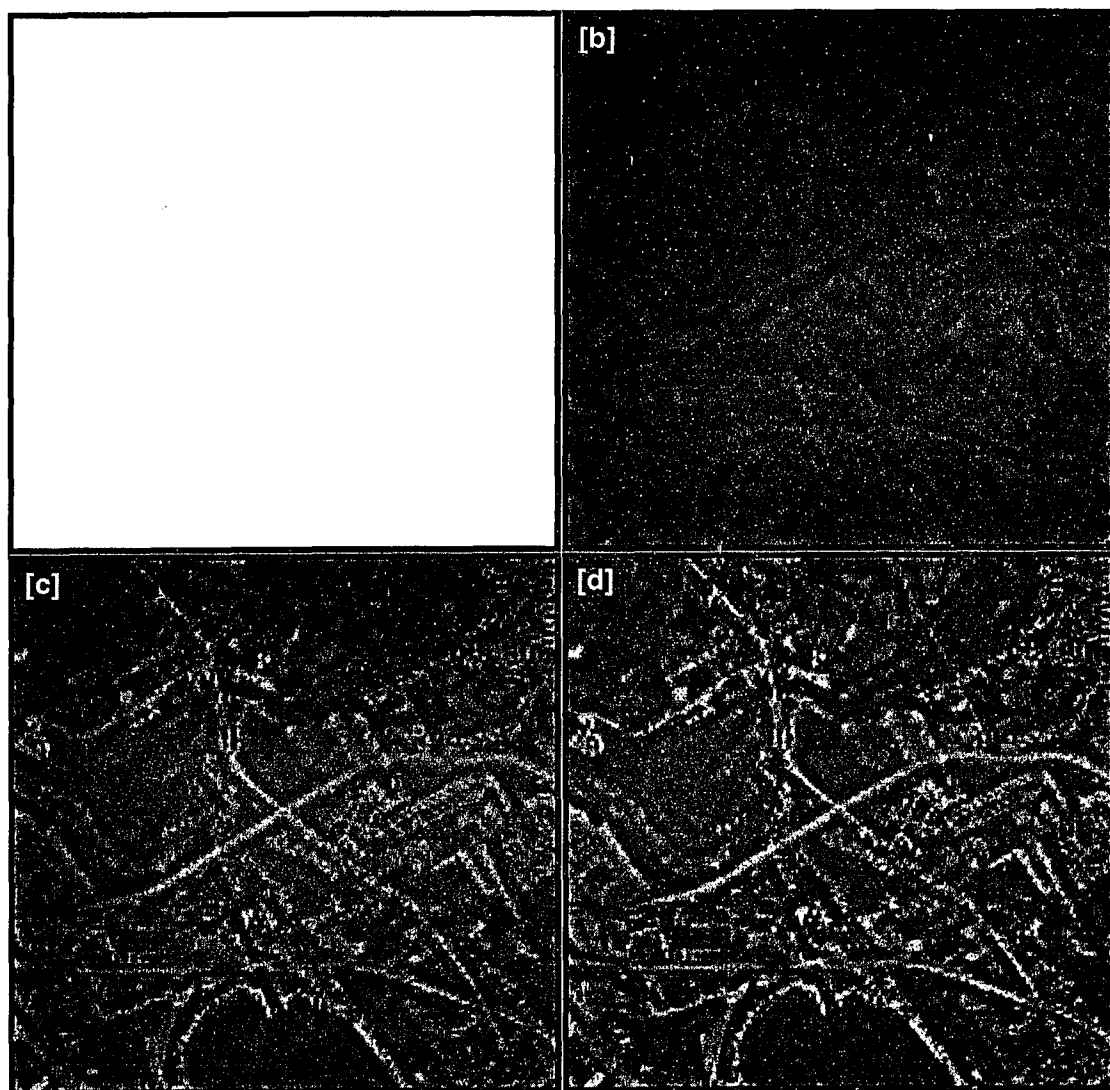


Figure 6.2: Difference images for spatially unconstrained and small-kernel CLS restorations.

tically contrast-stretched. These images demonstrate that the differences between the unconstrained CLS restoration and the small-kernel CLS restorations are *not* random. The differences in these images are mainly near the edges and other areas of fine spatial detail because constraining the size of the restoration filter affects the filter's ability to boost high frequencies. As demonstrated by the images in figure (6.1), however, the differences are small and for a  $7 \times 7$  CLS restoration filter kernel, figure (6.2[b]), essentially negligible.

This simulation demonstrates that implementation efficiency gained from using a small-kernel CLS restoration filter does not necessarily come at the expense of restoration quality. This observation is consistent with that made by Reichenbach et al. [47] who concluded that using a small restoration Wiener restoration kernel as opposed to the unconstrained optimal filter does not adversely affect the accuracy of the Wiener restoration technique.

The ability to apply the c/d/c model-based CLS restoration filter as a small convolution kernel allows it to be used in image restoration applications that are subject to stringent timing constraints but cannot use expensive hardware to apply the restoration filter in the frequency domain. Additionally, as demonstrated in chapter 8, the small CLS restoration kernel can also be applied adaptively because convolution with a small kernel is a local operation.

## CHAPTER VII

### CLS RESTORATION OF FORWARD-LOOKING INFRARED IMAGERY

This chapter presents an application of the  $c/d/c$  model-based CLS restoration filter described in chapter 5 for improving the performance of FLIR-based imaging systems. In FLIR (forward-looking infrared) systems, performance usually refers to target acquisition, including detection, classification, recognition, and identification either by a human observer or an automatic target recognizer (ATR). Although performance measures for ATRs are not very well-defined, the distance (range) at which a human observer or ATR can reliably identify a target is generally accepted as a reliable measure of ATR performance. Digital image restoration has the potential to significantly improve the effective range (and hence performance) in FLIR-based imaging systems by improving the quality of the digital image presented to the observer or the ATR. In this chapter, it is demonstrated that a small-kernel  $c/d/c$  model-based CLS restoration filter can be used to improve the effective range in FLIR imagery.

## 7.1 CLS Restoration of FLIR Imagery

Because of timing constraints, most present day ATRs do not actually produce a reconstructed image from the digital image. Without reconstruction, however, MSD-based metrics cannot be used to quantify the end-to-end performance of the imaging system. Due to the lack of appropriate ATR performance metrics, reconstruction is used in this chapter to generate an output image; doing so allows input-output comparison in a MSD sense that in turn allows effective range reduction to be quantified. In this way this chapter demonstrates that a c/d/c model-based CLS restoration can be used to achieve *effective range reduction*. That is, the study uses digital images of a target acquired at different ranges and attempts to produce an estimate of the original closest range image.

The imaging system is a staring-array based FLIR system; the focal plane array (FPA) consists of  $256 \times 320$  photo-detectors spaced  $\Delta = 31\mu m$  apart in both the horizontal and vertical directions. The OTF  $\hat{H}$  is modeled as the the cascaded frequency response of the optics  $\hat{H}_o$  and the detector  $\hat{H}_d$  responses as<sup>1</sup>

$$\hat{H}(\omega_1, \omega_2) = \hat{H}_o(\omega) \hat{H}_d(\omega_1, \omega_2). \quad (7.1)$$

The optical system OTF is

$$\hat{H}_o(\omega) = \begin{cases} \left[ \cos^{-1}\left(\frac{\omega}{\omega_0}\right) - \frac{\omega}{\omega_0} \sqrt{1 - \left(\frac{\omega}{\omega_0}\right)^2} \right] \exp\left(-0.5\left(\frac{\omega}{\omega_0}\right)^2\right) & \omega \leq \omega_0 \\ 0 & \omega > \omega_0 \end{cases} \quad (7.2)$$

---

<sup>1</sup>Although it is potentially significant, the atmospheric OTF component is ignored.

where  $\omega^2 = \omega_1^2 + \omega_2^2$  is the radial frequency variable. The normalized cut-off frequency  $\omega_0$  is given by

$$\omega_0 = \frac{A\Delta}{\lambda F} \quad (7.3)$$

where  $F$  is the focal length,  $A$  is the aperture diameter and  $\lambda$  is the mean wavelength. For this system,  $F = 100mm$ ,  $A = 43mm$  and  $\lambda = 5.5\mu m$ . From these values,  $\omega_0 = 2.45$  cycles/pixel. The Gaussian OTF component, with a scale parameter  $\omega_b$ , accounts for optical defocus. For this system  $\omega_b = 0.281$  cycles/pixel. This  $\omega_b$  value was estimated by using the PSF estimation method described in [73].

The detector response in the spatial domain is modeled as a simple square pulse to account for (ideal) spatial integration. That is,

$$\hat{H}_d(\omega_1, \omega_2) = P^2 \text{sinc}(P\omega_1) \text{sinc}(P\omega_2) \quad (7.4)$$

where  $\text{sinc}(x) = \sin(\pi x)/(\pi x)$  and  $P$  is the size of the detector relative to the inter-sample distance (samples-per-dwell parameter). For the system described  $P = 1$ . The SNR for this system is estimated to be 22.5.

Figure (7.1) illustrates an actual image sequence acquired by this FLIR-based imaging system.<sup>2</sup> The target, an automobile, was imaged at 100m interval ranges

---

<sup>2</sup>The images were acquired at the U.S. Army's Electro-Optics and Night-Vision Laboratories in Fort Belvoir, Virginia for the purpose of testing the actual performance of the c/d/c model-based Wiener filter as a function of range. During image acquisition, every effort was made to keep all variables other than range, fixed. The results of the Wiener filter-based study are available in [92]. This simulation duplicates the processing described in that report except for the use of a small-kernel CLS restoration filter in place of a small-kernel Wiener filter.



from 100m to 800m. As expected, with increasing range the target becomes more difficult to detect because spatial resolution decreases with range. The 100m image is the reference image; the longer range images are processed and then compared to this image.

For the purpose of digital processing, the entire image at each range was not selected; instead, a sub-image containing the target (automobile) was used. To facilitate the use of a FFT routine, the dimensions of all the sub-images are powers to 2; the 200m and 300m sub-images are  $128 \times 128$ , the 400m through 700m sub-images are  $64 \times 64$  and the 800m sub-images is  $32 \times 32$ . Figure (7.2) illustrates the sub-images. Except for the 100m (reference) image, the others have been enlarged by using PCC reconstruction. No restoration filtering has been performed. Because of inevitable changes in the horizontal and vertical positions of the camera relative to the initial (100m) image, the translation and scale are adjusted after reconstruction to achieve the highest correlation between the result image and the reference image. Due to slight changes in the camera's alignment, there is a bright (sun glint) spot in the 400m, 500m and 600m images; this spot is not present in the reference (100m) image. The presence of this spot is unfortunate; its effect on the range-reduction ability of the CLS restoration filter is discussed later.

Figure (7.3) is analogous to figure (7.2) except for the use of a  $5 \times 5$  CLS restoration filter prior to reconstruction.<sup>3</sup> All other processing, including the final trans-

---

<sup>3</sup>The reference (100m) image is not filtered.

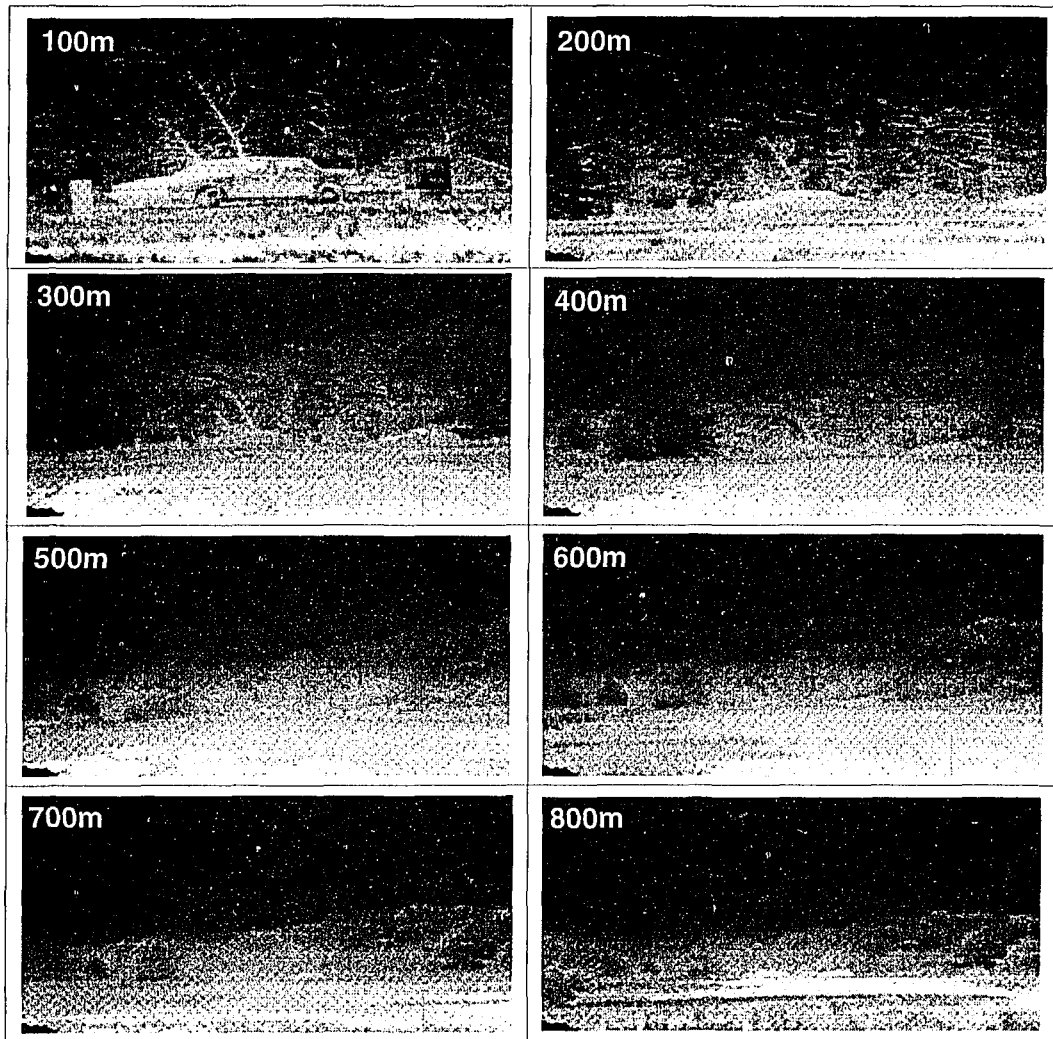


Figure 7.1: Unprocessed actual images at distances of 100m to 800m at 100m intervals.

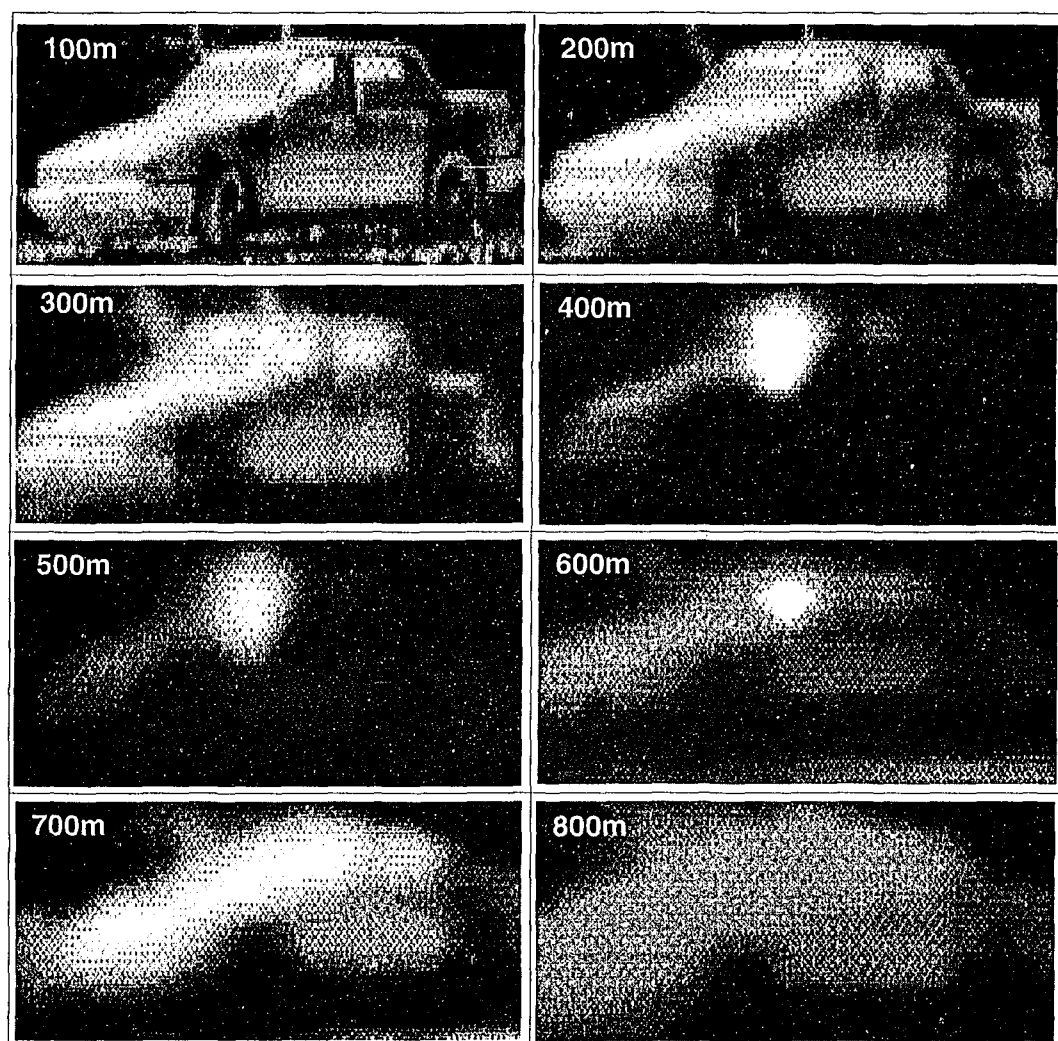


Figure 7.2: 100m reference image and PCC reconstructions of 200m to 800m images.

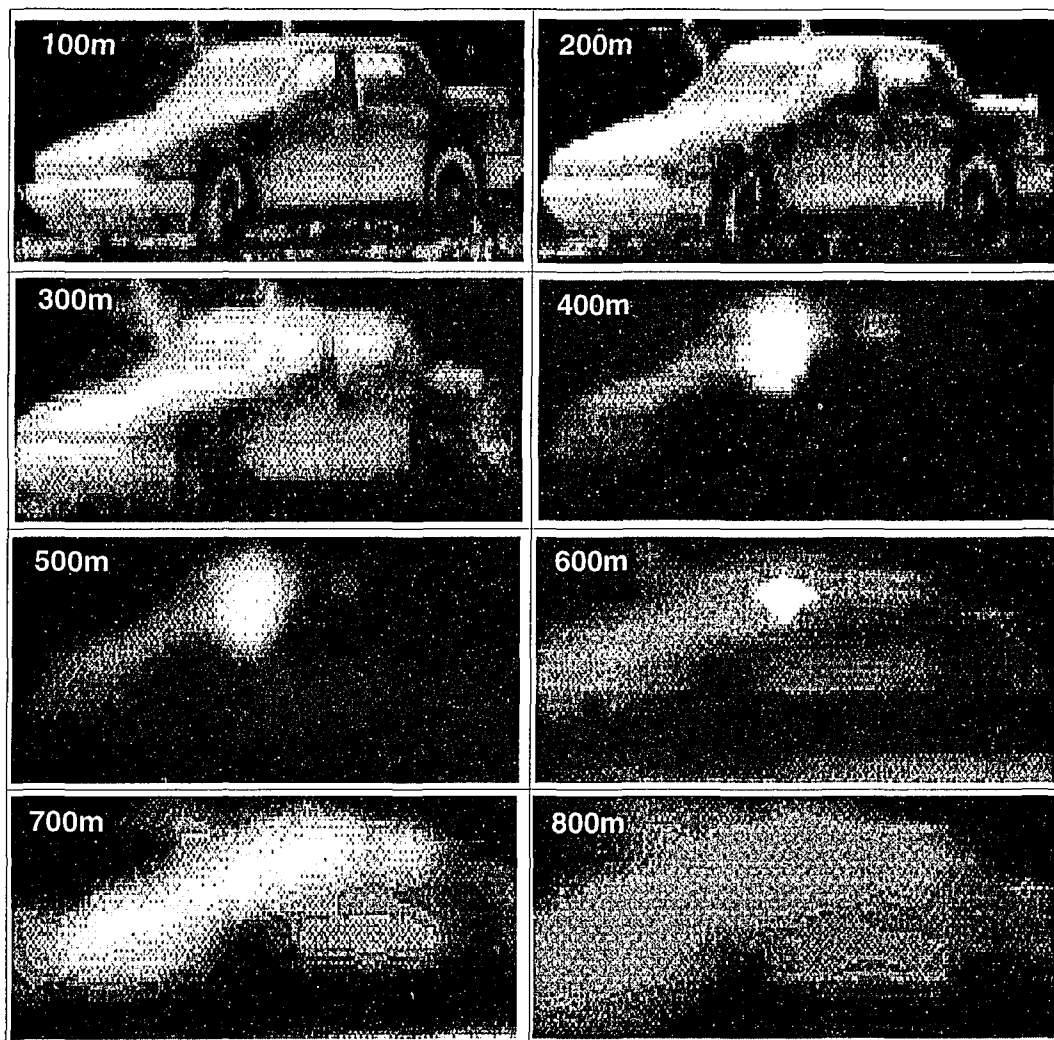


Figure 7.3: 100m reference image and CLS restorations of 200m to 800m images.

lation and scaling, is identical to that used to generate the images in figure (7.2). To generate the small-kernel CLS filter for each image, the high-pass filter defined in equation (5.17) is used with  $k = 2$ . The parameter  $\alpha$  is computed by using the Chi-Square Choice method.

By comparing figures (7.3) and (7.2), it is clear the filtered images are sharper than the corresponding unfiltered ones. The restored images are similar in quality to the ones obtained by a small-kernel ( $5 \times 5$ ) Wiener restoration filter [92]. The sharpening is more effective for the smaller ranges and degrades with increasing range; at the larger ranges aliasing noise is significant and the c/d/c model-based CLS restoration filter does not sharpen much to avoid aliased noise enhancement. Relative to the 100m image the bright glare spot in the 400m, 500m and 600m images is an unwanted scene feature that influences the restoration filter via the computation of  $\alpha$ . Because of this, the quality of the 400m, 500m and 600m restored images is degraded.

The results presented in this chapter demonstrate that a small-kernel CLS restoration filter can be used to restore FLIR images efficiently and effectively. The restorations produced by the CLS filter are similar in quality to those produced by the Wiener filter [92]. Unlike the Wiener filter, however, the CLS filter coefficients can be computed much more easily and efficiently; this makes the CLS filter a better choice for FLIR range-reduction applications.

## CHAPTER VIII

### CLS RESTORATION OF RADIATION MEASUREMENTS FROM A SATELLITE-BORNE SCANNING RADIOMETER

This chapter presents a remote-sensing application of the  $c/d/c$  model-based CLS restoration technique presented in chapter 5.<sup>1</sup> The imaging instrument in this application is the satellite-borne scanning radiometer used by NASA for the Earth Radiation Budget Experiment (ERBE). The ERBE instrument measures outgoing radiation from the Earth and its atmosphere; therefore the radiometer does not produce visual images in a traditional sense of the term. The scanning action of the radiometer combined with the forward motion of the satellite does, however, produce a 2-D array of radiance measurements that can be conceptualized as a digital image of the earth's radiation field. This conceptualization facilitates the application of digital image processing techniques, including restoration.

When ERBE measurements are reconstructed by interpolation, the reconstructed field is not an accurate estimate of the original radiation field; small-scale features present in the original field are degraded by blurring, random noise and sampling artifacts. This chapter demonstrates the use of a CLS restoration technique for filtering the discrete measurements to undo, to the extent possible, these degrada-

---

<sup>1</sup>The material presented in this chapter will appear as a journal article in [93].

tions. CLS restoration is more difficult in this application, however, because the ERBE geometry makes the image acquisition process shift-variant. Therefore, the c/d/c model presented in chapter 3 and the associated CLS filter have to be used in a special way to account for shift-variance.

## 8.1 ERBE System Model

The end-to-end process of making measurements of the earth's radiation field and interpolating (reconstructing) the measurements to obtain an estimate of this field can be described by a c/d/c model that is similar, in most respects, to the one presented in chapter 3. The one significant difference between that model and the ERBE system model is in the image acquisition module — in the ERBE model the imaging geometry makes the image acquisition process *shift-variant*. That is, as explained in the following discussion, it is impossible to find an underlying coordinate system for the ERBE system model in which the instrument's PSF does not change with viewing location.

### 8.1.1 ERBE Coordinate System

Two choices for the ERBE coordinate system are illustrated in figure (8.1). In the *scene-based* geocentric coordinate system the point  $A$  on the earth's surface is described by a pair of angles  $(\gamma_a, \gamma_c)$  that describe the point's position relative to the center of the earth. As an alternative, the point  $A$  can also be unambiguously

specified in an *instrument-based* coordinate system by a pair of angles  $(\delta_a, \delta_c)$  that describe the point's position relative to the current satellite position.

In a traditional c/d/c model-based application such as the one described in chapter 7, the scene-based coordinate system and the instrument-based coordinate system are assumed to be linearly related; this makes choosing one of them as the underlying coordinate system for the c/d/c model largely a matter of convenience and convention. Unlike traditional c/d/c model-based imaging applications, however, the scene-based  $(\gamma_a, \gamma_c)$  coordinate system and the instrument-based  $(\delta_a, \delta_c)$  coordinate system are *not* linearly related [96]. Consequently, uniform sampling in one coordinate system does not imply uniform sampling in the other. In particular, in the cross-track (scan) direction samples are uniformly spaced in the instrument-based coordinate system; in the along-track (flight) direction the samples are uniformly spaced in the geocentric coordinate system. Therefore, uniform sampling can be achieved in the ERBE c/d/c model if the underlying coordinate system is one in which along-track distances are measured in geocentric angular dimensions  $\gamma_c$  and cross-track distances are measured in instrument-based angular dimensions  $\delta_c$ .

### 8.1.2 ERBE Image Acquisition

To express ERBE image acquisition in the  $(\gamma_a, \delta_c)$  coordinate system it is necessary to express both the instrument PSF and the scene radiation field in this coordinate system. The  $(\delta_a, \delta_c)$  coordinate system is generally the natural choice for expressing



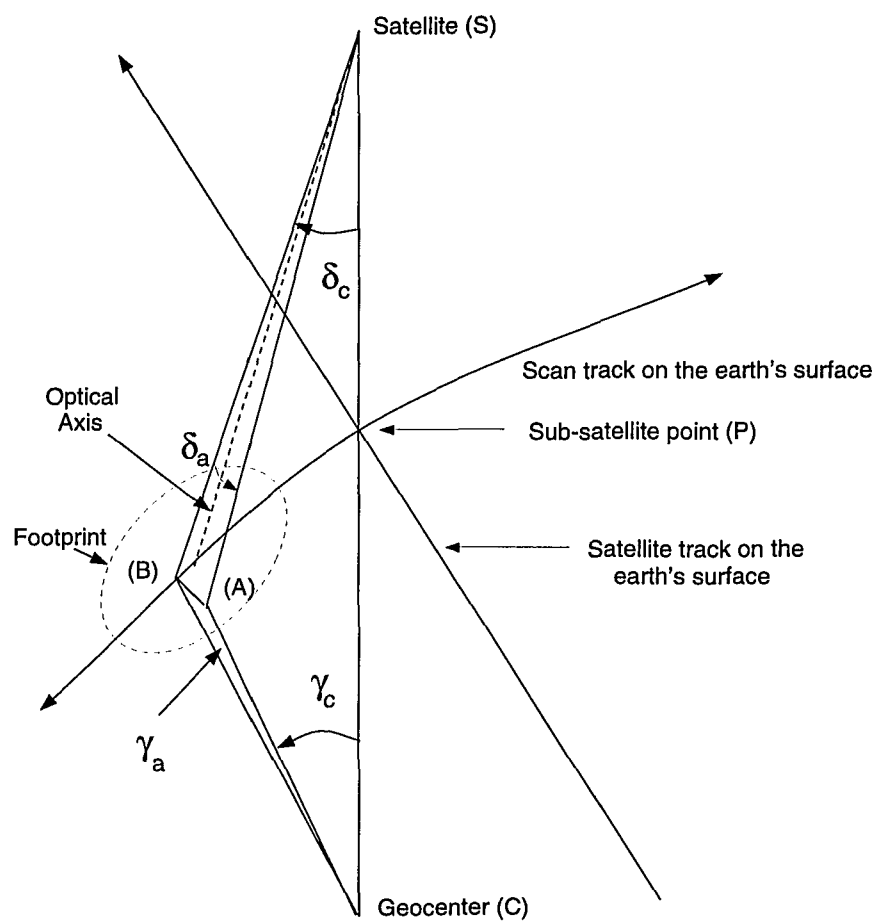


Figure 8.1: Imaging geometry and coordinate systems.

the instrument's PSF; therefore, the PSF must be converted to the  $(\gamma_a, \delta_c)$  coordinate system using the transformation<sup>2</sup>

$$\gamma_a \approx \frac{\mathbf{S}(\delta_c) \tan \delta_a}{R} \quad (8.1)$$

where  $\mathbf{S}(\delta_c)$  is the *slant-range* ( $\overline{SB}$  in figure (8.1)). Since the transformed coordinate  $\gamma_a$  is a function of *both* the cross-track coordinate  $\delta_c$  and the along-track coordinate  $\delta_a$ , equation (8.1) illustrates the shift-variant nature of ERBE image acquisition. In particular, it can be shown that the same  $\delta_a$  transforms into larger  $\gamma_a$ 's if  $\delta_c$  is increased; the instruments footprint grows in the along-track direction as the optical axis moves away from nadir. Therefore, although the  $(\gamma_a, \delta_c)$  coordinate system results in uniform sampling, image acquisition is shift-variant.

### 8.1.3 Shift-variant Image Restoration

Due to the shift-variant image acquisition process, the pre-sampled field  $g$  must be expressed as an integral equation with a position-dependent PSF as

$$g(\gamma_a, \delta_c) = \int \int h(\gamma'_a, \delta'_c; \gamma_a, \delta_c) s(\gamma_a - \gamma'_a, \delta_c - \delta'_c) d\gamma'_a d\delta'_c \quad (8.2)$$

over the entire field of view (swath). Because equation (8.2) is not a convolution, the c/d/c model for the ERBE instrument cannot be developed in the frequency domain in the manner presented in chapter 3. Consequently, the CLS restoration

---

<sup>2</sup>Equation (8.1) is an approximation in the sense that  $P$  and  $B$  are assumed to be joined by a line instead of an arc. This approximation is particularly accurate for a small field of view and greatly simplifies the relationship between  $\gamma_a$ ,  $\delta_a$  and  $\delta_c$ .

technique that uses this frequency domain description as the basis of its derivation, is not directly applicable.

In this chapter, a “sectioning” approach is adopted to overcome the shift-variant PSF problem; the radiation field is partitioned into vertical strips (sub-sections) and the PSF is assumed to be shift-variant within each section [94][95]. In this way shift-invariant restoration methods such as the CLS restoration technique can be used in the individual sections. Artifacts caused by artificially sectioning the radiation field are controlled by using overlapping sections. A necessary consequence of the partitioning approach, however, is the need to generate a CLS restoration filter for each section. Sectioning details are provided in section 8.2.

## 8.2 Simulation Results

This section uses simulated ERBE data to demonstrate the effectiveness of the CLS restoration-based reconstruction approach. Measurements are produced by simulating the measurement process on synthetic (artificial) input radiance fields. The use of simulated data provides a controlled environment for testing the CLS restoration filter. Artificial radiance fields provide a mechanism for explicitly designing the frequency content of the input, thereby making it possible to test the ability of the CLS restoration filter to restore frequencies of particular interest. The use of a known input scene also allows improved determination (and quantification) of restoration accuracy; this is a particularly important fact for ERBE and other

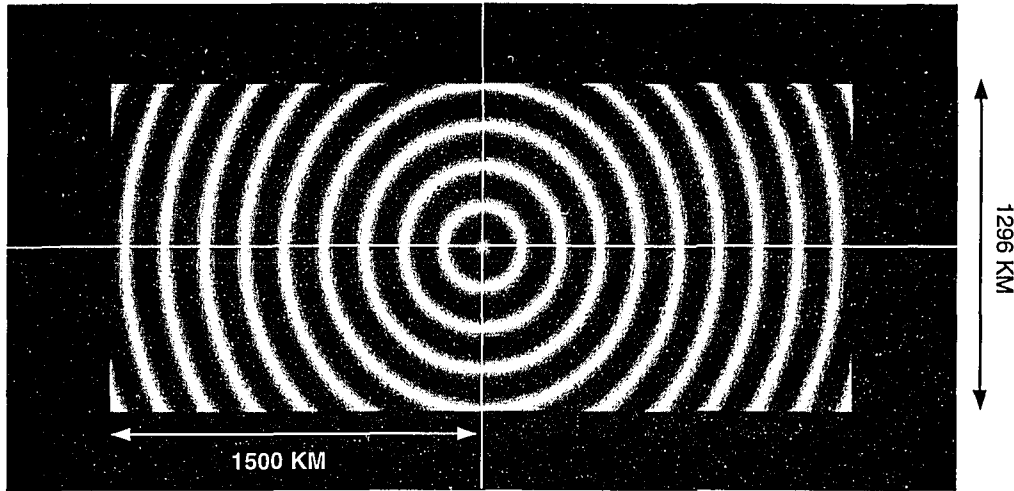


Figure 8.2: Simulated cosine radiance field.

radiometric instruments since there is no “ground-truth” that can be relied upon to judge the restoration accuracy.

The simulated input field,  $l$ , used in the CLS restoration study described in this section is presented in figure (8.2). The field represents a circularly symmetric cosine in the geocentric coordinate system defined as

$$l(\rho) = A_0 + A_1 \cos(\omega \rho) \quad (8.3)$$

where  $\omega$  denotes the cosine frequency and  $\rho = \sqrt{\gamma_a^2 + \gamma_c^2}$  is the radial distance from the origin. The simulated field in figure 8.2 uses  $\omega = 0.01$  cycles/km. The constants  $A_0 = 127.5$  and  $A_1 = 127.5$  are chosen to make  $l$  positive and have a dynamic range of 256, for ease of display on a 256-level display device.

The input radiance field to the c/d/c model  $s$  is obtained by mapping  $l$  from the  $(\gamma_a, \gamma_c)$  coordinate system to the required  $(\gamma_a, \delta_c)$  coordinate system using the

transformation

$$\delta_c = \tan^{-1} \left[ \frac{\sin \gamma_c}{(1 - \cos \gamma_c) + H/R} \right]. \quad (8.4)$$

In equation (8.4)  $H$  is the satellite altitude (measured from sea-level) and  $R$  is the radius of the earth; for ERBE  $H/R = 0.0926$ . The effect of the coordinate transformation in equation (8.4) is to distort  $l$  in the cross-track direction. The distortion has the effect of changing the pure cosine into a cosine function with a position-dependent frequency argument in the cross-track direction; the greater the distance from the origin, the higher the frequency.

Equation (8.4) also demonstrates why a c/d/c model-based Wiener filter would not be very practical in the ERBE context. Even if the energy spectrum of the field could be accurately characterized in the  $\{\gamma_a, \gamma_c\}$  coordinate system, perhaps from physical information about the field itself, there is no easy way to express that in the  $(\gamma_a, \delta_c)$  coordinate system because of the non-linear transformation. The CLS restoration filter does not have this problem because it does not require such an estimate.

The ERBE scanning radiometer's PSF is illustrated in figure (8.3) [97]. The coordinate system used to describe the PSF is the  $(\delta_a, \delta_c)$  system depicted in figure (8.1). To project the PSF in figure (8.3) onto the  $(\gamma_a, \delta_c)$  coordinate system, the coordinate transformation defined in equation (8.1) is used.

The simulated flight path of the satellite falls along the  $\gamma_a$  axis and takes the satellite directly over the center of the cosine. Scanning proceeds from left to right;

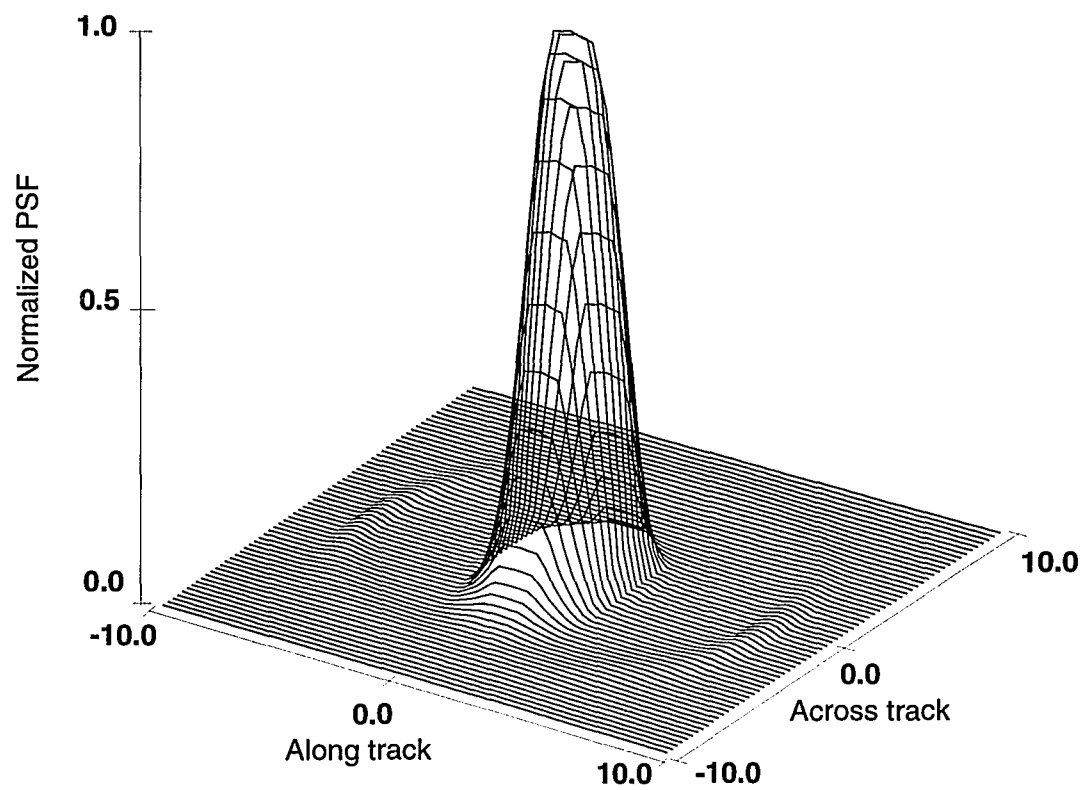


Figure 8.3: ERBE scanning radiometer PSF.

no measurements are made on the right-to-left (flyback) scan. Each sample of the resultant digital image is obtained using a numerical quadrature routine to integrate the PSF-weighted radiance within the IFOV. The scanning angle is to 60 deg on either side of nadir. The digital image is corrupted by additive, uniformly distributed (“white”) noise quantified by an SNR of 20.

The noisy, sampled field in figure (8.5a) is then reconstructed to a continuous field at the top-of-atmosphere (TOA) using the PCC reconstruction filter.<sup>3</sup> The reconstructed field is shown in figure (8.6a). The loss of resolution can be seen clearly in figure (8.6a). Consistent with the growth of the footprint in the along-track direction with scan angle (figure (8.4)), the resolution loss increases with increasing scan angle.

The measured field in figure (8.5a) is sectioned into 20.4 degree “vertical” sections spaced 6.06 degrees apart in the cross-track direction. This corresponds to sections 10 pixels wide with an overlap of 3 pixels and yields 19 sections over the entire swath. The extreme left and right sections have fewer than 10 pixels since the limiting scan-angle for measurements is 60 deg. The amount of overlap is dictated by the effective support of the PSF [94].<sup>4</sup> The section size represents a compromise between the number of pixels required to minimize the border-effects of circular

---

<sup>3</sup>The TOA is an meteorological reference surface, 30 km above sea-level, which is used for locating the measurements.

<sup>4</sup>In this application the effective support (width) of the PSF is the minimum pixel distance from the origin at which the PSF drops to 0.1 of its value at the origin.

convolution (during restoration) and the rate of increase in the size of the PSF along the  $\delta_a$  coordinate axis. The lower limit on the size of a section is bounded by the effective support of the PSF — the section size must be equal (and preferably larger) than the PSF. The upper bound on section size is determined primarily by how much the PSF's effective support changes over a given section.

The increase in the effective support of the PSF in the along-track direction with increasing scan-angle ( $\delta_c$ ) is illustrated in figure (8.4). As can be seen in this figure, the effective width of the PSF in the along-track direction increases from approximately 2 pixels at nadir to about 4 pixels at the limb. Each section is restored using an “average” PSF determined by computing the average of the PSFs at either extreme of the section. An alternative approach involves interpolating the restoration filter kernel between the extreme points to account for (small) variations in the PSF within each section. This approach is computationally more expensive and the increase in restoration accuracy is not large enough to warrant the additional computational burden. In the simulations, to generate the CLS restoration kernel for each section, the circularly symmetric high-pass filter kernel

$$\hat{C}(\omega) = 2.0 - 2.0 \cos(\omega) \quad (8.5)$$

is used;  $\omega$  represents the radial frequency in the  $(\gamma_a, \delta_c)$  coordinate system. The value of  $\alpha$  is determined by using the Chi-Square Choice method described in chapter 5.

The restored field in the  $(\gamma_a, \delta_c)$  coordinate system and the corresponding TOA reconstruction are shown in figure (8.5b) and (8.6b) respectively. The mapping from



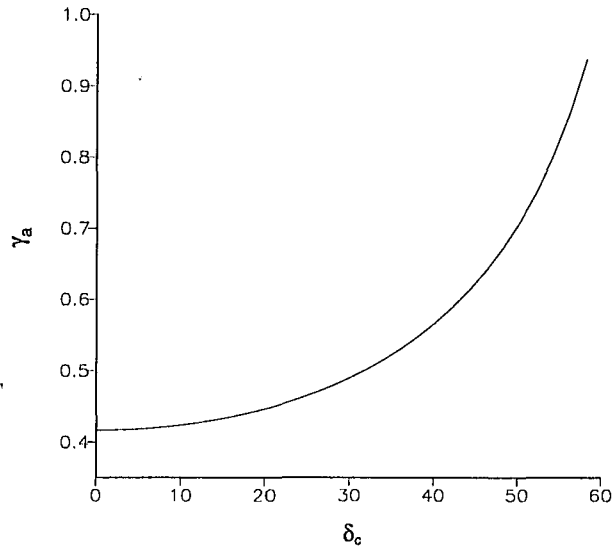
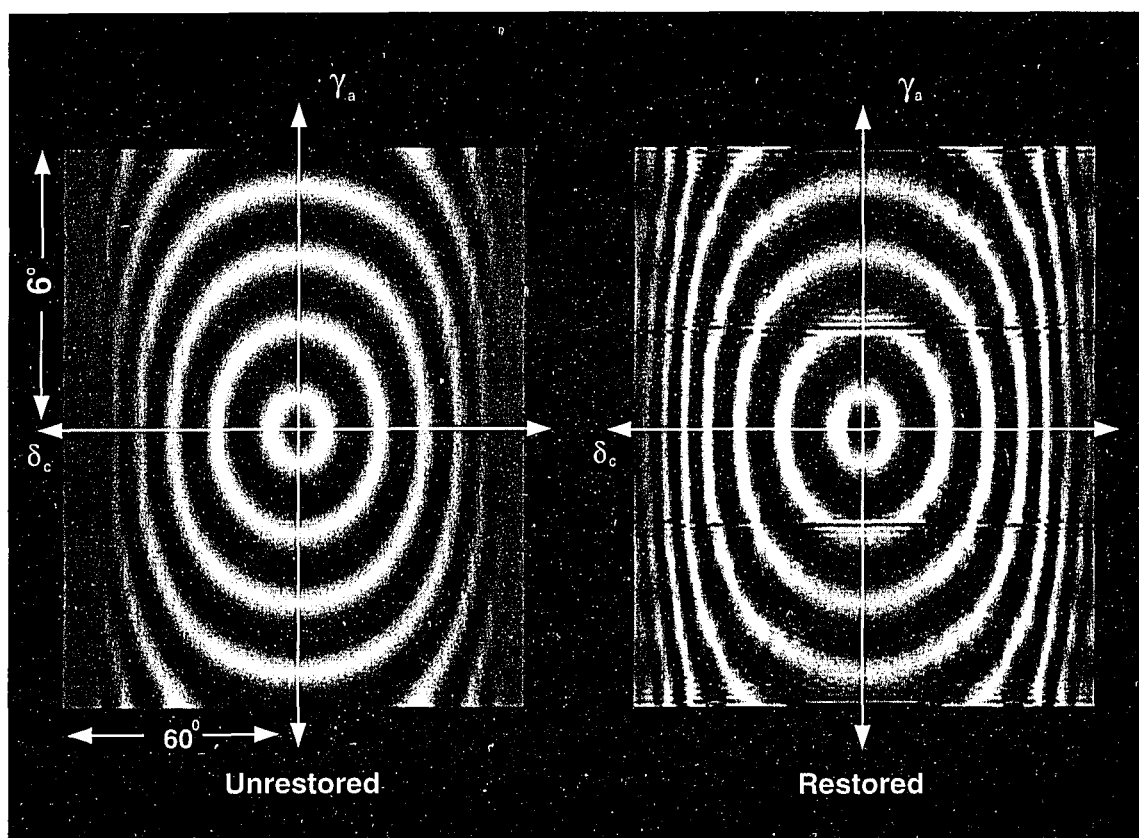


Figure 8.4: Footprint growth in the along-track direction with scan angle.

the  $(\gamma_a, \delta_c)$  coordinate system to the TOA coordinate system is obtained by inverting equation (8.4). The restoration shown were obtained by using  $7 \times 7$  restoration kernels over each of the 19 sections. Consistent with the high-pass filtering effects of the CLS restoration filter, the restored image is sharper than the unrestored image. The figures clearly show that the “rings” of the cosine that were blurred beyond recognition in the un-restored image (and its TOA reconstruction) have been partially recovered. This restoration comes at the expense of some noise amplification which is evident in the restorations.

The two horizontal artifacts (situated symmetrically about the center of the image) are a result of simulated line “drop-outs”, missing data due to instrument and/or transmission equipment malfunction, an important practical consideration. In the simulations, these missing scans are set to 0; the discontinuity introduced by



(a)

(b)

Figure 8.5: Restored versus unrestored digital image.

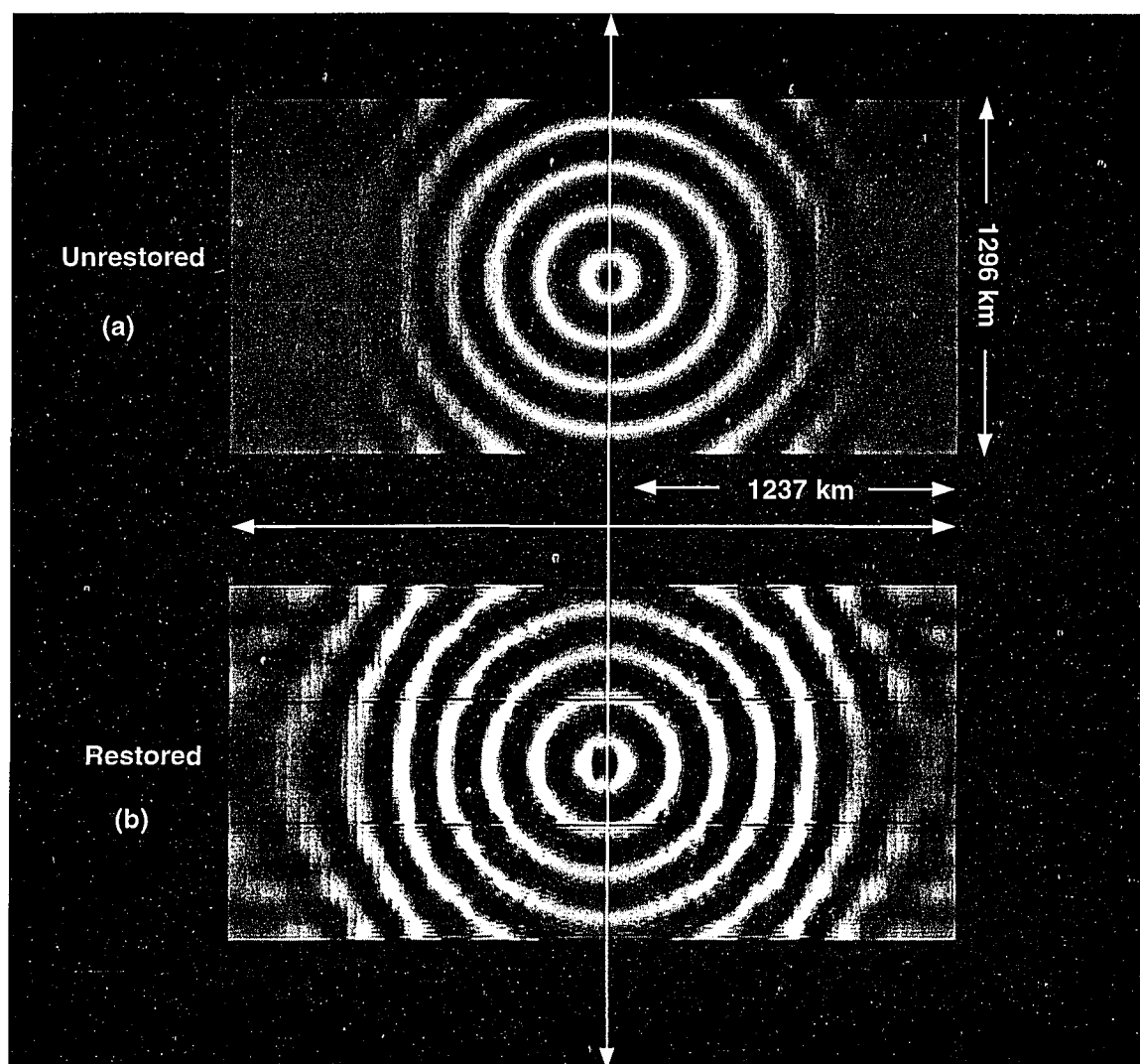


Figure 8.6: Restored versus unrestored TOA reconstructions.

this artifact is enhanced by the restoration filter that mistakes it for a high-frequency feature in the measured image. In practice, the exact locations of the missing data are known from ancilliary data and interpolation can be used to minimize the discontinuity effect.

This chapter demonstrates that a small-kernel c/d/c model-based CLS restoration filter can be used effectively and efficiently to improve the spatial resolution of remotely-sensed radiometric data. Improving data quality by using restoration processing has the potential to improve scientific analysis based on such data.

# CHAPTER IX

## CONCLUSIONS

### 9.1 Conclusions

The design of a digital image restoration filter must address the following restoration concerns: an accurate underlying imaging system model, a practical restoration metric, a computationally efficient filter synthesis algorithm, and an efficient filter implementation in the spatial domain as a small-kernel convolution. This dissertation presents convincing evidence as to why these four issues are important.

Simulation can be used to demonstrate that the widely-used  $d/d$  model is not the correct system model for digital imaging systems because the  $d/d$  model ignores sampling and reconstruction. If image acquisition blurring is the only source of image degradation,  $d/d$  model-based restoration filters can restore perfectly. These filters are also relatively effective in balancing restoration sharpening against random noise enhancement. When sampling and reconstruction are present, however, the same  $d/d$  model-based restoration filters fail to restore satisfactorily; the restored images exhibit sampling and reconstruction artifacts that are enhanced by the restoration filters.

A  $c/d/c$  system model is a superior alternative to the  $d/d$  system model. In

addition to image acquisition and additive random noise, this model explicitly accounts for sampling and reconstruction. By doing so, a c/d/c model provides an additive, scene-dependent *noise*-like characterization of sampling artifacts. For the purpose of digital restoration filter design this scene-dependent (aliased) noise has to be treated in the same manner as additive random noise.

Although optimal in a MSD sense, the c/d/c model-based Wiener filter has several practical problems. The use of the end-to-end MSD metric in the Wiener filter derivation results in an expression for the Wiener filter's response that cannot be evaluated without making statistical assumptions about the unknown stochastic scene and the random noise. Acceptable Wiener restorations may be computationally demanding, making the c/d/c model-based Wiener filter unsuitable in many time-constrained applications. Moreover, the c/d/c model-based Wiener filter cannot be implemented rigorously because the energy spectra of the stochastic scene and the additive random noise are never known *a priori*.

The c/d/c model-based CLS restoration filter is a viable alternative to the c/d/c model-based Wiener filter with several practical advantages. The derivation of the CLS filter does not require any statistical assumptions about the unknown scene and the random noise. Therefore, the CLS filter is applicable to a broader class of image restoration applications than is the Wiener filter. The CLS filter can also be applied rigorously; all the terms in the filter's response are known (or can be measured) and therefore, no ad-hoc estimation procedure is required. The c/d/c model-based CLS

restoration filter can also be implemented effectively and efficiently as a small-kernel convolution in the spatial domain, facilitating its use in real-time image restoration applications.

## 9.2 Future Research

### 9.2.1 Optimal regularization

The issue of a *scene-dependent* stabilizing functional  $\hat{C}$  needs to be investigated. There is some limited d/d model-based evidence that scene-dependent stabilizing functionals can improve restoration quality; this needs to be investigated in the context of a c/d/c model. In a recent article, Reeves et al. [58] proposed a technique that computes both  $\alpha$  and  $\hat{C}$  directly from the digital image; they claim that the resulting restorations are superior to those obtained by the traditional method described in chapter 2. The extension of their technique to a c/d/c model should be investigated.

### 9.2.2 Adaptive CLS Restoration

The Wiener and CLS restoration filters presented in this dissertation are *global* in the sense that a single restoration filter is used to restore the entire image. Since images are not spatially homogeneous, global restoration filters cannot be expected to perform as well as *adaptive* restoration filters that take local image characteristics into account. Adaptive image restoration is not a new area of research; all

known adaptive restoration techniques, however, are based on a d/d system model. The use of the c/d/c model-based CLS restoration filter as an adaptive restoration filter needs to be investigated. One possible approach would be to adapt  $\alpha$  by using a simple parametric model for  $\hat{p}$ , then estimating the model parameters directly from the digital image. Another approach would be to use different degrees of regularization by using different stabilizing functionals depending upon the local smoothness. These and other approaches should be evaluated for restoration accuracy and computational efficiency.

### 9.2.3 Color (Multi-spectral) CLS Restoration

The applicability of the c/d/c model-based CLS filter to color (multi-spectral) image restoration should be investigated.



## Appendix A

When a digital image is used as input to a c/d/c model-based simulation, the Fourier series coefficients of the band-limited scene have to be constructed from the DFT coefficients of the digital image. If this construction is done correctly then the band-limited scene interpolates the digital image exactly. That is, if this synthesized scene is sampled on the same pixel grid as the digital image then the resulting sampled image and the digital image are identical. This appendix describes the mathematics associated with such a construction technique. In practice, the number of rows and columns in the digital image are even numbers; that is the only case considered in this appendix.

**Theorem: A** *Given a digital image  $m$  periodic with period  $P_1 \times P_2$  and a band-limited, periodic scene*

$$s(x_1, x_2) = \sum_{|\nu_1| \leq \tau_1} \sum_{|\nu_2| \leq \tau_2} \hat{S}[\nu_1, \nu_2] \exp(i2\pi\nu_1 x_1 / P_1) \exp(i2\pi\nu_2 x_2 / P_2)$$

*with period  $P_1 \times P_2$ , if  $P_1$  and  $P_2$  are both even integers and*

$$\tau_1 = P_1/2 \quad \tau_2 = P_2/2$$

*then  $s$  interpolates  $m$  exactly provided*

$$\hat{S}[\nu_1, \nu_2] = \begin{cases} \hat{m}[\nu_1, \nu_2] & \text{if } |\nu_1| < \tau_1 \text{ and } |\nu_2| < \tau_2 \\ \frac{\hat{m}[\tau_1, \nu_2]}{2} & \text{if } |\nu_1| = \tau_1 \text{ and } |\nu_2| < \tau_2 \\ \frac{\hat{m}[\nu_1, \tau_2]}{2} & \text{if } |\nu_1| < \tau_1 \text{ and } |\nu_2| = \tau_2 \\ \frac{\hat{m}[\tau_1, \tau_2]}{4} & \text{if } |\nu_1| = \tau_1 \text{ and } |\nu_2| = \tau_2 \end{cases}$$

where

$$\hat{m}[\nu_1, \nu_2] = \sum_{n_1=0}^{P_1-1} \sum_{n_2=0}^{P_2-1} m[n_1, n_2] \exp(-i2\pi n_1 \nu_1 / P_1) \exp(-i2\pi n_2 \nu_2 / P_2)$$

is the DFT array associated with  $m$ .

**Proof:**

The MSD between  $m$  and the digital image obtained by sampling  $s$  on the  $P_1 \times P_2$  pixel-grid is

$$\text{MSD} = \frac{1}{P_1 P_2} \sum_{n_1=0}^{P_1-1} \sum_{n_2=0}^{P_2-1} |s(n_1, n_2) - m[n_1, n_2]|^2.$$

Using Parseval's equation and the sampling theorem the MSD can be expressed in the frequency domain as

$$\text{MSD} = \sum_{\nu_1=0}^{P_1-1} \sum_{\nu_2=0}^{P_2-1} |\langle \hat{S}[\nu_1, \nu_2] \rangle - \hat{m}[\nu_1, \nu_2]|^2.$$

Both  $\langle \hat{S}[\nu_1, \nu_2] \rangle$  and  $\hat{m}[\nu_1, \nu_2]$  are periodic with period  $P_1 \times P_2$ ; the MSD can be written over a different range of  $P_1 \times P_2$  frequencies as

$$\text{MSD} = \sum_{\nu_1=-P_1/2}^{P_1/2-1} \sum_{\nu_2=-P_2/2}^{P_2/2-1} |\langle \hat{S}[\nu_1, \nu_2] \rangle - \hat{m}[\nu_1, \nu_2]|^2.$$

The MSD can be simplified to

$$\begin{aligned} & \sum_{|\nu_1| < \tau_1} \sum_{|\nu_2| < \tau_2} |\langle \hat{S}[\nu_1, \nu_2] \rangle - \hat{m}[\nu_1, \nu_2]|^2 + \sum_{|\nu_2| < \tau_2} |\langle \hat{S}[-\tau_1, \nu_2] \rangle - \hat{m}[-\tau_1, \nu_2]|^2 \\ & + \sum_{|\nu_1| < \tau_1} |\langle \hat{S}[\nu_1, -\tau_2] \rangle - \hat{m}[\nu_1, -\tau_2]|^2 + |\langle \hat{S}[-\tau_1, -\tau_2] \rangle - \hat{m}[-\tau_1, -\tau_2]|^2. \end{aligned}$$

Because  $\hat{S}[\nu_1, \nu_2] = 0$  for  $|\nu_1| > \tau_1$  and  $|\nu_2| > \tau_2$ ,  $\langle \hat{S}[\nu_1, \nu_2] \rangle = \hat{S}[\nu_1, \nu_2]$  for  $|\nu_1| < \tau_1$  and  $|\nu_2| < \tau_2$ . Therefore, by choosing  $\hat{S}[\nu_1, \nu_2] = \hat{m}[\nu_1, \nu_2]$  for  $|\nu_1| < \tau_1$  and  $|\nu_2| < \tau_2$

the MSD reduces to

$$\begin{aligned} & \sum_{|\nu_2| < \tau_2} |\hat{m}[-\tau_1, \nu_2] - \hat{S}[-\tau_1, \nu_2] - \hat{S}[\tau_1, \nu_2]|^2 + \\ & \sum_{|\nu_1| < \tau_1} |\hat{m}[\nu_1, -\tau_2] + \hat{S}[\nu_1, -\tau_2] - \hat{S}[\nu_1, \tau_2]|^2 - \\ & |\hat{m}[-\tau_1, -\tau_2] - \hat{S}[-\tau_1, -\tau_2] + \hat{S}[-\tau_1, \tau_2] - \hat{S}[\tau_1, -\tau_2] - \hat{S}[\tau_1, \tau_2]|^2. \end{aligned}$$

For  $s$  to interpolate  $m$  exactly the remaining Fourier series coefficients in this MSD expression must be chosen to make the MSD equal 0. By inspection, this is accomplished by choosing the coefficients as

$$\hat{S}[\nu_1, \nu_2] = \begin{cases} \frac{\hat{m}[\tau_1, \nu_2]}{2} & \text{if } |\nu_1| = \tau_1 \text{ and } |\nu_2| < \tau_2 \\ \frac{\hat{m}[\nu_1, \tau_2]}{2} & \text{if } |\nu_1| < \tau_1 \text{ and } |\nu_2| = \tau_2 \\ \frac{\hat{m}[\tau_1, \tau_2]}{4} & \text{if } |\nu_1| = \tau_1 \text{ and } |\nu_2| = \tau_2 \end{cases}$$

This completes the proof of this theorem.

Note that if  $m$  is real-valued then

$$\begin{aligned} \hat{m}[-\nu_1, -\nu_2] &= \hat{m}^*[\nu_1, \nu_2] \\ \hat{m}[-\nu_1, \nu_2] &= \hat{m}^*[\nu_1, -\nu_2] \end{aligned}$$

Moreover,  $\hat{m}[\tau_1, \tau_2]$  is real-valued. By choosing  $\hat{S}$  in the manner just described,

$$\begin{aligned} \hat{S}[-\nu_1, -\nu_2] &= \hat{S}^*[\nu_1, \nu_2] \\ \hat{S}[-\nu_1, \nu_2] &= \hat{S}^*[\nu_1, -\nu_2] \end{aligned}$$

That is,  $s$  is also real-valued.

Most DFT implementations, including virtually all FFT implementations, compute the  $\hat{m}[\nu_1, \nu_2]$  array for  $0 \leq \nu_1 \leq P_1 - 1, 0 \leq \nu_2 \leq P_2 - 1$ . The theorem presented in this appendix requires DFT coefficients with negative frequency indices. Because the DFT array is periodic, these negative-index coefficients can be computed from the positive-index DFT coefficients by using the  $P_1 \times P_2$  periodicity equation

$$\hat{m}[\nu_1, \nu_2] = \hat{m}[\nu_1 \bmod P_1, \nu_2 \bmod P_2].$$

## Bibliography

- [1] Andrews H.C., and Hunt B.R., *Digital Image Restoration*, Prentice-Hall, Englewood Cliffs, NJ., 1977.
- [2] Katsagellos A.K., *Digital Image Restoration*, Springer-Verlag Series in Information Sciences, 1991.
- [3] Lim J.S., *Two-Dimensional Signal and Image Processing*, Prentice-Hall, Englewood Cliffs, NJ., 1990.
- [4] Jain A.K., *Fundamentals of Digital Image Processing*, Prentice-Hall, Englewood Cliffs, NJ., 1989.
- [5] Sezan I., *Selected papers on digital image restoration*, SPIE Milestone Series, MS 47, SPIE Bellingham, Washington, 1992.
- [6] Mertz P., and Gray F., "A theory of scanning and its relation to the characteristics of the transmitted signal in telephotography and television", *Bell Systems Technical Journal*, Vol. 13, pp. 464-515, 1934.
- [7] Elias P., Grey D.S., and Robinson D.F., "Fourier treatment of optical processes", *Journal of the Optical Society of America*, Vol. 42, pp. 127-134, 1952.
- [8] Linfoot E.H., "Transmission factors and optical design", *Journal of the Optical Society of America*, Vol. 46, No. 9, pp. 740-756, 1956.
- [9] Nathan R., *Digital Video Handling*, Tech. Rep. 32-887, NASA, 1966.

- [10] Schreiber W.F., *Fundamentals of Electronic Imaging Systems*, Springer-Verlag lecture series, 1986.
- [11] Schade O.H. Sr., "Image reproduction by a line raster process", *Perception of Displayed Information*, Chapter 6, pp. 233–278, Plenum Press, New York, NY, 1973.
- [12] Park S.K., "Image gathering, interpolation and restoration: a fidelity analysis", *SPIE 1992 Technical Symposium on Visual Information Processing*, Vol. 1705, pp. 134–144, 1992.
- [13] Park S.K., and Reichenbach S.E., "Digital image gathering and minimum mean-square error restoration", *Proceedings of the SPIE*, Vol. 1360, Visual Communications and Image Processing, pp. 1578–1589, 1990.
- [14] Fales C.L., Huck F.O., Park S.K., and McCormick J.A., "Wiener restoration of sampled image data", *Journal of the Optical Society of America*, Vol. A5, pp. 300–314, 1988.
- [15] Linfoot E.H., "Quality evaluations of optical systems", *Optica Acta*, Vol. 5, pp. 1–14, 1958.
- [16] Mertz P., Fowler A.D., and Christopher H.N., "Quality rating of television images", *Proceedings of the IRE*, Vol. 138, pp. 1269–1283, 1950.

- [17] Budrikis Z.L., "Visual fidelity criterion and modeling", *Proceedings of the IEEE*, Vol. 60, No. 7, pp. 771-779, 1972.
- [18] Hall C.F., and Hall E.L., "A nonlinear model for the spatial characteristics of the human visual system", *IEEE Transactions on Systems, Man and Cybernetics*, Vol. SMC-7, pp. 274-283, 1977.
- [19] Campbell F.W., "The physics of visual perception", *Philosophical Transactions of the Royal Society of London*, Series B, Vol. 290, pp. 5-9, 1980.
- [20] Hazra R., Park S.K., and Miller K.W., "Model based quantification of image quality", *Proceedings of the Second International Conference on Visual Information Processing for T.V. and Telerobotics*, NASA Conf. Pub. 3053, pp. 11-22, 1989.
- [21] Marmolin H., "Subjective MSE measures", *IEEE Transactions on Systems, Man and Cybernetics*, Vol. SMC-16, No. 3, 1986.
- [22] Hall E., and Dwyer S., "Evaluating image quality: a new formulation computer", *Biology and Medicine*, Vol. 2, pp. 15-25, 1982.
- [23] Nillson U., Marmolin H., and Nyberg S., "Computer simulation of visual models", FOA report C 53010-H2, National Defence Research Institute, Stockholm, Sweden, 1982.

- [24] Granath D.J., "The role of human visual models in image processing", *Proceedings of the IEEE*, Vol. 69, No. 5, pp. 552-561, 1981.
- [25] Anderson G.L., and Netravali A.N., "Image restoration based on a subjective criterion", *IEEE Transactions on Systems, Man and Cybernetics*, Vol. SMC-6, No. 12, 1976.
- [26] Frieden B.R., "Restoring with maximum likelihood and maximum entropy", *Journal of the Optical Society of America*, Vol. 62, No. 4, pp. 511-518, 1972.
- [27] Gonsalves R.A., and Kao H.M., "Entropy based algorithm for reducing artifacts in image restoration", *Optical Engineering*, Vol. 26, No. 7, pp. 617-622, 1987.
- [28] Trussel H.J., "The relationship between image restoration by a maximum a posteriori method and a maximum entropy method", *IEEE Transactions on Acoustics, Speech and Signal Processing*, Vol. ASSP-28, No. 1, pp. 114-117, 1980.
- [29] Burch S.F., Bull S.F., and Skilling J., "Image restoration by a powerful maximum entropy method", *Computer Vision, Graphics and Image Processing*, Vol. 23, pp. 113-128, 1983.
- [30] Hunt B.R., "Bayesian methods in nonlinear digital image restoration", *IEEE Transactions on Computers*, Vol. C-26, No. 3, pp. 219-229, 1977.



- [31] Trussel H.J., and Hunt B.R., "Sectioned methods for image restoration", *IEEE Transactions on Acoustics, Speech and Signal Processing*, Vol. ASSP-26, No. 2, pp. 157-164, 1978.
- [32] Trussel H.J., and Hunt B.R., "Improved methods of maximum a posteriori restoration", *IEEE Transactions on Computers*, Vol. C-27, No. 1, pp. 57-62, 1979.
- [33] Woods J.W. and Radewan C.W., "Kalman filtering in 2 dimensions", *IEEE Transactions on Information Theory*, Vol. 23, pp. 473-482, 1977.
- [34] Biemond J., Rieske J., and Gerbands J.J., "A fast Kalman filter for images degraded by both blur and noise", *IEEE Transactions on Acoustics, Speech and Signal Processing*, Vol. 31, No. 5, pp. 1248-1256, 1983.
- [35] Quereschi A.G., "Constrained Kalman filtering for image restoration", *IEEE Transactions on Acoustics, Speech and Signal Processing*, Vol. 37, pp. 1405-1408, 1989.
- [36] Suresh B.R., and Shenoi B.A., "New results in 2D Kalman filtering with applications to image restoration", *IEEE Transactions on Circuits and Systems*, Vol. 28, No. 4, pp. 307-319, 1981.
- [37] Cetin A.E., and Tekalp A.M., "Robust reduced update Kalman filtering", *IEEE Transactions on Circuits and Systems*, Vol. 36, No. 13, pp. 155-157, 1989.

- [38] Sanz J.L.C., and Huang T.S., "Unified Hilbert space approach to iterative least squares linear signal restoration", *Journal of the Optical Society of America*, Vol. 73, No. 11, pp. 1455-1465, 1983.
- [39] Trussel H.J., and Civanlar M.R., "The Landweber iteration and projection onto convex sets", *IEEE Transactions on Acoustics, Speech and Signal Processing*, Vol. ASSP- 33, No. 6, pp. 1632-1634, 1985.
- [40] Wiener N., *Extrapolation, Interpolation and Smoothing of Stationary Time Series*, MIT Press, Cambridge, MA, 1942.
- [41] Helstrom C.W., "Image restoration by the method of least squares", *Journal of the Optical Society of America*, Vol. 57, No. 3, pp. 297-303, 1967.
- [42] Slepian D., "Linear least-squares filtering of distorted images", *Journal of the Optical Society of America*, Vol. 57, No. 7, pp. 918-922, 1967.
- [43] Hunt B.R., "Application of constrained least-squares estimation to image restoration", *IEEE Transactions on Computers*, Vol. C-22, No. 9, pp. 805-812, 1973.
- [44] Park S.K., "Linear digital imaging system fidelity analysis", *Proceedings of the Second International Conference on Visual Information Processing for T.V. and Telerobotics*, NASA Conf. Pub. 3053, pp. 3-10, 1989.

- [45] Huck F.O., Altenburg R.A., and Zia-ur Rahman, "Image gathering and digital restoration for fidelity and visual quality", *Computer Graphics, Vision and Image Processing*, Vol. 53, No. 1, 1991.
- [46] Sezan M.I., and Takalp M.A., "Survey of recent developments in digital image restoration", *Optical Engineering*, Vol. 29, No. 5, pp. 393-404, 1990.
- [47] Reichenbach S.E., and Park S.K., "Small convolution kernels for high-fidelity image restoration", *IEEE Transactions on Signal Processing*, Vol. 39, pp. 2263-2274, 1991.
- [48] Arguello R.J., Sellner H.R., and Stuller J.A., "Transfer function compensation of sampled imagery", *IEEE Transactions of Computers*, Vol. 21, No. 7, pp. 812-818, 1972.
- [49] Riemer T.E., and McGillem C.D., "Optimum constrained image restoration filters", *Applied Optics*, Vol. 12, No. 9, pp. 2027-2029, 1977.
- [50] Scutten R.W., and Vermeij G.F., "The approximation of image blur restoration filters by finite impulse responses", *IEEE Transactions of Pattern Analysis and Machine Intelligence*, Vol. 2, No. 2, pp. 176-180, 1980.
- [51] Frieden B.R., "Image restoration by discrete convolution of minimal length", *Journal of the Optical Society of America*, Vol. 64, No. 5, pp. 682-686, 1974.

- [52] Lahart M.J., "Local image restoration by a least-squares method.", *Journal of the Optical Society of America*, Vol. 69, No. 10, pp. 1333-1339, 1979.
- [53] Chu N-Y., McGillem C.D., "Image restoration filters based on a 1-0 weighting over the domain of support of the PSF", *IEEE Transactions of Acoustics Speech and Signal Processing*, Vol. 27, No. 5, pp. 457-464, 1979.
- [54] Walkup J.F., and Choens R.C., "Image processing in signal dependent noise", *Optical Engineering*, Vol. 13, pp. 258-266, 1974.
- [55] Park S.K., "Lecture notes in digital image processing", Department of Computer Science, College of William & Mary, 1994.
- [56] Tikhonov A.N., and Arsenin V.Y., *Solutions of Ill-posed problems*, Winston, Washington D.C., 1977.
- [57] Karayannis N.B., and Venetsanopoulos A.N., "Image restoration: a regularization approach", *Proceedings of the Second International Conference on Image Processing and its Applications*, Conference Publication No. 256, pp. 1-5, 1989.
- [58] Reeves S.J., and Merserau R.M., "Optimal estimation of the regularization parameter and stabilizing functional for regularized image restoration", *Optical Engineering*, Vol. 29, No. 5, pp. 446-454, 1990.
- [59] Bruneau J-M, and Mathieu P., "Image restoration using biorthogonal wavelet transforms", *Optical Engineering*, Vol. 33, No. 7, pp. 2378-2384, 1994.

- [60] Castleman K.R., *Digital Image Processing*, Prentice-Hall, Engelwood Cliffs, NJ., 1979.
- [61] Brown D.E., "Digital image restoration: a comparative analysis", *Masters Thesis*, Department of Electrical & Computer Engineering, George Washington University, 1987.
- [62] Park S.K., and Hazra R., "Aliasing as noise: a quantitative and qualitative assessment", *Proceedings of the SPIE 1993 Technical Symposium on Visual Information Proceedings II*, Vol. 1961, pp. 2-13, 1993.
- [63] Modestino J.W., and Fries R.W., "Construction and properties of useful two-dimensional random fields", *IEEE Transactions on Information Theory*, Vol. 26, pp. 44-50, 1980.
- [64] Reichenbach S.E., Park S.K., Alter-Gartenburg R., and Rahman Zia-ur, "Artificial scenes and simulated imaging", *Proceedings of the SPIE Symposium on Stochastic and Neural Methods in Signal Processing, Image Proceedings and Computer Vis.*, Vol. 1569, pp. 422-433, 1991.
- [65] Lee J.S., "Digital image enhancement and noise filtering by use of local statistics", *IEEE Transactions on Pattern Analysis and Machine Intelligence*, Vol. 2, No. 2, pp. 165-168, 1980.
- [66] Jain A.K., "Advances in mathematical models for image processing", *Proceedings of the IEEE*, Vol. 69, No. 5, 1981.

- [67] Jain A.K., "Noncausal representations of finite discrete signals", *Proceedings of the IEEE Conference on Decision and Control*, Arizona, 1974.
- [68] Woods J.M., "Two dimensional discrete Markov fields", *IEEE Transactions on Information Theory*, Vol. 18, pp. 232-240, 1972.
- [69] Woods J.M., "Markov image modeling", *IEEE Transactions on Automatic Control*, Vol. 23, No. 5, 1978.
- [70] Mizutani Q., and Sugimoto L., "Semicausal models and smoothing for 2D random image fields", *Proceedings of the 11<sup>th</sup> JAACE Symposium on Stochastic Systems*, pp. 161-164, 1979.
- [71] Powell S.R., and Silverman L.M., "Modeling of 2D covariance functions with application to image restoration", *IEEE Transactions on Automatic Control*, Vol. 19, pp. 8-13, 1974.
- [72] Boudaoud M., and Chaparro L.F., "Nonstationary composite modeling of images", *IEEE Transactions on Systems, Man and Cybernetics*, Vol. 19, No. 1, pp. 112-117, 1989.
- [73] Reichenbach S.E., Park S.K., and Narayanswami R., "Characterizing digital image acquisition devices", *Optical Engineering*, Vol. 30, No. 2, pp. 170-177, 1991.

- [74] Mitchell D.P., and Netravelli A.N., "Reconstruction filters in computer graphics", *Computer Graphics*, Vol. 24, No. 4, pp. 221–228, 1988.
  - [75] Johnson C.B., "A method for characterizing electro-optical device modulation transfer functions", *Photographic Science & Engineering*, Vol. 14, No. 6, pp. 413–415, 1970.
  - [76] Lansing D., and Park S.K., "Quantitative analysis of the reconstruction performance of interpolants", *NASA Technical Publication 2688*, NASA Langley Research Center, 1987.
  - [77] Park S.K., and Schowengerdt R.A., "Image reconstruction by parametric cubic convolution", *Computer Vision Graphics & Image Processing*, Vol. 23, pp. 258–272, 1983.
  - [78] Park S.K., and Hazra R., "Image restoration versus aliased noise enhancement", *Proceedings of the SPIE 1993 Technical Symposium on Visual Information Processing III*, Orlando, 1993.
  - [79] Vincent J.D., *Fundamentals of infra-red detector operation and testing*, John Wiley & Sons, New York, NY 1990.
  - [80] Park S.K., "Lecture notes in discrete linear systems theory", Department of Computer Science, College of William & Mary, 1994.
-

- [81] Welch P.D., "The use of Fast Fourier Transform for the estimation of power spectra: a method based on time averaging over short, modified periodograms", *IEEE Transactions on Audiophonics and Electroacoustics*, Vol. 15, pp. 70-73, 1967.
- [82] Rino C.L., "Factorization of spectra by discrete Fourier transforms", *IEEE Transactions on Information Theory*, Vol. 16, pp. 484-485, 1970.
- [83] Sage A.P., and Melsa J.L., *Estimation theory with applications to communications and control*, McGraw-Hill, 1971.
- [84] Woods J.M., "Two dimensional Markov spectral estimation", *IEEE Transactions on Information Theory*, Vol. 22, pp. 552-559, 1976.
- [85] Jain A.K., "Spectral estimation and signal extrapolation in one and two dimensions", *Proceedings of the RADC Spectral Estimation Workshop*, Rome NY, pp. 195-214, 1979.
- [86] Dickinson B.W., "2D Markov spectral estimates need not exist", *IEEE Transactions on Information Theory*, Vol. 26, pp. 120-121, 1980.
- [87] Jain A.K., and Ranganath S., "Application of two dimensional spectral estimation in image restoration", *Proceedings of the IEEE International Conference on Acoustics, Speech and Signal Processing*, pp. 1113-1116, 1981.



- [88] Ekstrom M.P., "Realizable Wiener filtering in two dimensions", *IEEE Transactions on Acoustics, Speech and Signal Processing*, Vol. 30, No. 1, pp. 31-41, 1982.
- [89] Hazra R., Park S.K., Smith G.L., and Reichenbach S.E., "Constrained least-squares image restoration filters for sampled image data", *Applications of Digital Image Proceedings XVI*, SPIE Vol. 2028, pp. 177-192, 1993.
- [90] Hall P, and Titterton D.M., "On some smoothing techniques used in image restoration", *Journal of the Royal Statistical Society (B)*, Vol. 48, pp. 330-343, 1986.
- [91] Reichenbach S.E., "Small-kernel image restoration", *Ph.D dissertation*, College of William & Mary, July 1989.
- [92] Reichenbach S.E., "Restoration and range performance in FLIR imaging systems", Final Report for TCN 92471, July 1994.
- [93] Hazra R., Smith G.L., and Park S.K., "Estimation of earth's radiation field from Earth Radiation Budget Experiment (ERBE) measurements", *to appear in the IEEE Transactions on Geoscience and Remote Sensing*, 1995.
- [94] Trussel H.J., and Hunt B.R., "Image restoration of space-variant blurs by sectioned methods", *IEEE Transactions on Acoustics, Speech and Signal Processing*, Vol. 26, pp. 608-609, 1978.

- [95] Trussel H.J., and Hunt B.R., "Sectioned methods in image processing", *IEEE Transactions on Acoustics, Speech and Signal Processing*, Vol. 26, pp. 157-164, 1978.
- [96] Smith G.L., and Hazra R., "Satellite-based image formation: a quantitative analysis of shift-variance effects", submitted to the *Journal of the Optical Society of America (A)*, December 1994.
- [97] Kopia L.P., "Earth Radiation Budget Scanner Instrument", *Reviews of Geophysics*, Vol. 24, pp. 400-406, 1986.

## VITA

### Rajeeb Hazra

The author was born in Calcutta, India on the 25th day of January, 1965. He received his Bachelor's Degree in Computer Science and Engineering from Jadavpur University, Calcutta, in 1987. He then entered the graduate program in the Department of Computer Science at the College of William & Mary in the Fall of 1987 and was awarded a Master of Science in Computer Science in December of 1989. In August 1990, he was admitted into the Ph.D program in Computer Science at the College of William & Mary. He has been on the staff at Lockheed Engineering and Sciences Company and is currently a Research Associate in the Department of Atmospheric Sciences at Oregon State University. His research interests include the modeling and performance analysis of sampled imaging systems and the design of computationally efficient digital restoration filters for images produced by such systems.